

THE GLACIAL HISTORY OF THE WEDDELL SEA EMBAYMENT,  
ANTARCTICA

AN ABSTRACT

SUBMITTED ON THE TWENTY-FIRST DAY OF OCTOBER 2020  
TO THE DEPARTMENT OF EARTH AND ENVIRONMENTAL SCIENCES  
IN PARTIAL FULFILLMENT OF THE REQUIREMENTS  
OF THE SCHOOL OF SCIENCE AND ENGINEERING

OF TULANE UNIVERSITY

FOR THE DEGREE

OF


DOCTOR OF PHILOSOPHY

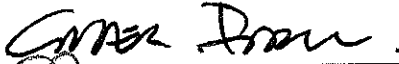
BY

---


Keir Alexander Nichols

Approved: \_\_\_\_\_

  
Brent M. Goehring, Ph.D.  
Director

  
Greg Balco, Ph.D.

  
Torbjörn E. Törnqvist, Ph.D.

  
George C. Flowers, Ph.D.

# **The Glacial History of the Weddell Sea Embayment, Antarctica**

Keir Alexander Nichols

## **Abstract**

I present research that improves our understanding of the glacial history of the Antarctic Ice Sheet and advances the method of in situ  $^{14}\text{C}$  exposure dating. Firstly, I present research investigating deglaciation in the Weddell Sea Embayment (WSE) sector of the Antarctic Ice Sheet. Large spatial gaps exist in our knowledge of the former configuration of the ice sheet in the WSE because previous studies observe cosmogenic nuclide exposure ages indicative of either significantly thicker ice than present at the Last Glacial Maximum (LGM) or limited (<100 m) thickening. The resulting pattern of past ice thickness is glaciologically unlikely. By measuring the short-lived cosmogenic nuclide in situ  $^{14}\text{C}$  in many of the same samples as previous studies, I show that ice at locations thought to have experienced limited thickening was at least 300 to 800 m thicker than present. These new constraints will help future modelling studies in their efforts to simulate the ice sheet and narrow down the contribution to deglacial sea level rise.

Next, I present an investigation into the source of elevated in situ  $^{14}\text{C}$  measurements observed from samples that were processed using a mineral separation technique called froth flotation. Multiple organic compounds are required for the use of froth flotation. With modern carbon sources, these organic compounds could introduce carbon contamination to samples. I find that froth flotation introduces modern carbon to samples and contaminant  $^{14}\text{C}$  is released with the in situ component. I then outline a procedure that demonstrably removes carbon contamination that can be followed by those isolating quartz for in situ  $^{14}\text{C}$  analysis.

Finally, I present an evaluation of the results of numerical ice sheet models using a compilation of exposure ages from the WSE. I use all published post-LGM  $^{10}\text{Be}$  and in situ  $^{14}\text{C}$  exposure ages from the WSE to assess how well models predict ice thinning histories evidenced by the cosmogenic nuclide measurements. Whilst most models are consistent with minimum geologic constraints for the thickness of the ice sheet, the timing and rate of the majority of post-LGM ice thinning predicted by ice sheet models is often both premature and more rapid than indicated by exposure ages.

THE GLACIAL HISTORY OF THE WEDDELL SEA EMBAYMENT,  
ANTARCTICA

A DISSERTATION

SUBMITTED ON THE TWENTY-FIRST DAY OF OCTOBER 2020

TO THE DEPARTMENT OF EARTH AND ENVIRONMENTAL SCIENCES

IN PARTIAL FULFILLMENT OF THE REQUIREMENTS

OF THE SCHOOL OF SCIENCE AND ENGINEERING

OF TULANE UNIVERSITY

FOR THE DEGREE

OF


DOCTOR OF PHILOSOPHY

BY

---

Keir Alexander Nichols

Approved:

  
Brent M. Goehring, Ph.D.  
Director

  
Greg Balco, Ph.D.

  
Torbjörn E. Tornqvist, Ph.D.

  
George C. Flowers, Ph.D.





## **Acknowledgements**

I would first like to thank my advisor Brent Goehring for his wonderful supervision over the last five years. Thank you for taking a chance on this geographer as one of your first graduate students, for encouraging me to embrace the field of geology, for your efforts sifting through my awful manuscript first (and sometimes second, and third...) drafts, and for trusting me with the radiocarbon line. I have learnt so much in and out of the laboratory, I hope I can pay that forward and be a great mentor one day. I would also like to thank my dissertation committee, Greg Balco, Torbjörn Törnqvist, and George Flowers, for your encouragement over the last two years.

I felt uncomfortable using the word "I" in this thesis, as this work would not have been possible without the help and work of many others. A huge thank you to my co-authors for my main chapter, Jo Johnson, Greg Balco, Andy Hein, and Claire Todd, for your support, knowledge, and sample material. It is an honour to be published alongside such wonderful people and scientists.

I must thank my fellow Tulane University Cosmogenic Nuclide Laboratory graduate students, Rachel, Cari, and Tori. Thank you for your unending support in and out of the laboratory, I wouldn't have come close to finishing my PhD without your help and friendship. I have to give a special thanks to Rachel for letting me drive on the wrong side of the road for three weeks as her field assistant in Alaska.

I would also like to thank the many Tulane EENS graduate students I have had the privilege of sharing a department with over the last five years. Graduate school is such a transient experience, but I have made some true lifelong friends here. I have to give special mentions to Jon, Dan, Travis, and Uditia. For the former three, I had the privilege of living with for one year, providing some of my most cherished memories of the last five years. For the latter, thank you for being a rock for this fellow international student.

Thank you to all of the support staff in the department, in particular Tonya Durden and Tanya Goehring. You keep the department ticking and always help graduate students with any concerns with lightning speed. Our graduate school experience would not be the same without you, maybe not even possible at all.

My greatest thanks must go to my mum, Janet, my dad, Ross, and my brother, Lewis. Thank you for all of our wonderful childhood holidays to mountainous areas that instilled within me a love of the natural world. Thank you for supporting me through my entire university journey, and especially for

helping me to fly home each Christmas. Without those trips I wouldn't have survived so far away from home for so long. Lewis, along with two of my best friends Chris and Matt, have kept me sane during my time in the US. Thank you for staying up late playing on Xbox with me to distract me from my qualifying exam and other graduate school worries.

Finally, thank you to my loving girlfriend, Faye. Thank you for sticking with me over the last three years and listening to me talk about cosmogenic nuclides and glaciers for what must have felt like a time longer than those I talk about in this thesis. I wouldn't have survived the last three years without you. Thank you for making New Orleans feel like home.

## **Table of Contents**

List of Tables .....	vi
List of Figures .....	vii
Chapter 1: Introduction .....	1
1. Cosmogenic nuclide geochronology .....	1
1.1 Exposure dating challenges.....	2
1.2 Pervasive nuclide inheritance in the Weddell sector of Antarctica .....	3
1.3 Why use in situ $^{14}\text{C}$ ? .....	4
1.4 In situ $^{14}\text{C}$ and preferred sampling material .....	5
1.5 Chapter 2 – In situ $^{14}\text{C}$ exposure dating in the Weddell Sea Embayment .....	6
1.6 In situ $^{14}\text{C}$ extraction .....	6
1.7 In situ $^{14}\text{C}$ extraction lines.....	7
1.8 Chapter 3 – Carbon contamination from quartz isolation.....	9
1.7 Chapter 4 – Evaluating ice sheet model outputs with cosmogenic nuclide measurements.....	10
1.8 Summary of chapters .....	11
1.8 References.....	11
Chapter 2. New Last Glacial Maximum Ice Thickness constraints for the Weddell Sea Embayment, Antarctica.....	21
Abstract.....	22
1. Introduction.....	22
1.1 The Last Glacial Maximum in the Weddell Sea Embayment.....	25
1.2 In situ $^{14}\text{C}$ exposure dating.....	28
1.3 Sample Sites .....	30
1.3.1 Shackleton Range.....	30
1.3.2 Lassiter Coast.....	31
1.3.3 Pensacola Mountains .....	32
2. Methods.....	32
3. Results.....	34
4. Discussion .....	38
4.1. Assessment of $^{14}\text{C}$ elevation transects .....	38
4.2 LGM ice thicknesses in the Weddell Sea Embayment .....	41
4.3 Grounding line position and flowline modelling comparison .....	44

4.4 Sea level contribution .....	45
5. Conclusions.....	48
Acknowledgements.....	48
References.....	49
Supplement .....	56
Chapter 3. Isolation of quartz for cosmogenic in situ <sup>14</sup> C analysis.....	74
Abstract.....	75
1. Introduction.....	75
1.1 Froth flotation and the isolation of quartz from whole rock material.....	77
1.1.1 Pre-Froth Flotation.....	77
1.1.2 Frothing Solution .....	77
1.1.3 Froth Flotation .....	78
1.1.4 Post-Froth Flotation Acid Etching.....	78
1.2 Initial Anomalous C-14 Measurements .....	79
2. Systematic Investigation .....	82
3. Results.....	84
4. Discussion.....	85
5. Conclusion .....	91
Acknowledgements.....	92
References.....	93
Tables.....	95
Chapter 4: An evaluation of ice sheet model-derived ice histories using cosmogenic nuclide measurements from the Weddell Sea Embayment sector of Antarctica.....	98
Abstract.....	99
1. Introduction.....	99
1.1 Deglaciation in the Weddell Sea Embayment .....	100
2. Methods.....	103
2.1 Ice sheet model outputs.....	104
2.2 Interpreting cosmogenic nuclide data for ice sheet models.....	104
3. Discussion .....	110
3.1 LGM misfit .....	110
3.2 Temporal misfit.....	113
3.3 Evaluating models with <sup>14</sup> C .....	117
3.4 Future work in the WSE .....	122
4. Conclusions.....	124
References.....	125
Chapter 5: Conclusion.....	134

References.....	135
-----------------	-----

**List of Tables****Chapter 2 Supplement:**

Table S2.1: Sample information .....	57
Table S2.2: In situ <sup>14</sup> C analytical data and exposure ages .....	64

**Chapter 3:**

Table 3.1: Aliquot information and quartz isolation procedures .....	95
Table 3.2: In situ <sup>14</sup> C analytical data.....	97

**Chapter 4:**

Table 4.1: Numerical ice sheet model and ice loading history information .....	133
--	-----

## **List of Figures**

### **Chapter 1:**

Figure 1.1: Map of the Weddell Sea Embayment.....	3
Figure 1.2: Exposure ages from the Lassiter Coast .....	4
Figure 1.3: Elevation versus in situ $^{14}\text{C}$ concentration of samples that initially yielded anomalously high $^{14}\text{C}$ concentrations .....	10

### **Chapter 2:**

Figure 2.1: The Weddell Sea Embayment, including all locations referred to within the text.....	24
Figure 2.2: Current terrestrial ice thickness constraints inferred from measurements of long-lived nuclides around the WSE .....	27
Figure 2.3: Hypothetical ice surface elevation change at a nunatak partially covered by ice at the LGM and resulting in situ $^{14}\text{C}$ concentration .....	29
Figure 2.4: Landsat imagery of study sites .....	31
Figure 2.5: Elevation versus in situ $^{14}\text{C}$ concentration of samples from the Shackleton Range .....	35
Figure 2.6: Elevation versus in situ $^{14}\text{C}$ concentration of samples collected from the Lassiter Coast.....	36
Figure 2.7: Elevation versus in situ $^{14}\text{C}$ concentration of samples collected from the Schmidt Hills .....	37
Figure 2.8: Elevation versus in situ $^{14}\text{C}$ concentration of samples collected from the Thomas Hills.....	37
Figure 2.9: Terrestrial ice thickness constraints inferred from measurements of cosmogenic nuclides around the WSE.....	41
Figure 2.10: Exposure-age results projected onto an elevation profile along flowline of the Slessor Glacier .....	42
Figure 2.11: Exposure-age results projected onto an elevation profile along flowline of the Foundation Ice Stream .....	43
Figure 2.12: Predicted LGM ice thickness change from three ice sheet model outputs at each of our study sites and their associated sea level equivalent.....	47

### **Supplement:**

Figure S2.1: Sample locations at Mount Skidmore .....	65
Figure S2.2: Sample locations at Mount Provender .....	66
Figure S2.3: Sample locations on Mount Lampert and an unnamed nunatak, Lassiter Coast .....	67

Figure S2.4: Sample locations in the Schmidt Hills, Pensacola Mountains .....	68
Figure S2.5: Sample locations in the Thomas Hills, Pensacola Mountains.....	69
Figure S2.6: Elevation versus in situ $^{14}\text{C}$ age of samples from the Shackleton Range	70
Figure S2.7: Elevation versus in situ $^{14}\text{C}$ age of samples from the Lassiter Coast.....	71
Figure S2.8: Elevation versus in situ $^{14}\text{C}$ age of samples from the Schmidt Hills. ....	72
Figure S2.9: Elevation versus in situ $^{14}\text{C}$ age of samples from the Thomas Hills.....	73

### **Chapter 3:**

Figure 3.1: Elevation versus in situ $^{14}\text{C}$ concentration of samples that initially yielded anomalously high $^{14}\text{C}$ concentrations .....	80
Figure 3.2: Initial and final unit yields associated with the same measurements presented in Fig. 3.1 .....	81
Figure 3.3: Unit yield and $^{14}\text{C}$ concentration for the five quartz separates.....	85
Figure 3.4: SEM images of quartz grains of aliquots 1 and 2.....	90
Figure 3.5: SEM images of quartz grains of aliquots 3 to 5. ....	91

### **Chapter 4:**

Figure 4.1: Post 26.5 ka $^{10}\text{Be}$ and $^{14}\text{C}$ exposure ages from the WSE .....	103
Figure 4.2: Two potential scenarios from measuring cosmogenic nuclide concentrations of samples collected from the surface of a nunatak and their relation to former ice extent constraints. ....	105
Figure 4.3: Misfit between total LGM ice thickness change from ice sheet model outputs and geologic constraints (part 1).....	111
Figure 4.4: Misfit between total LGM ice thickness change from ice sheet model outputs and geologic constraints (part 2).....	113
Figure 4.5: Mean temporal misfit at each site.....	114
Figure 4.6: Temporal misfit between exposure ages and the time the elevation associated with each age is deglaciated by model outputs .....	116
Figure 4.7: Evaluation of modelled ice surface histories with individual measurements of in situ $^{14}\text{C}$ .....	120

### **Supplement:**

Figure S4.1: Modelled ice surface histories and exposure ages for sites on the southern Antarctic Peninsula .....	106
Figure S4.2: Modelled ice surface histories and exposure ages for sites in the Ellsworth Mountains. ....	107
Figure S4.3: Modelled ice surface histories and exposure ages for the Whitmore Mountains at the WAIS Divide.....	108
Figure S4.4: Modelled ice surface histories and exposure ages for sites in the Pensacola Mountains. ....	109
Figure S4.5: Modelled ice surface histories and exposure ages for sites in the Shackleton Range.....	110



## **Chapter 1: Introduction**

### **1. Cosmogenic nuclide geochronology**

This thesis presents research on the development and application of the in situ produced cosmogenic nuclide carbon-14 ( $^{14}\text{C}$ ). Cosmogenic nuclides are rare isotopes produced at an approximately constant rate in the upper few metres of Earth surface materials by the interaction of cosmic radiation with target nuclei. By measuring the concentration of cosmogenic nuclides in a geologic sample, the rates of geomorphic and other geologic processes can be determined. Many cosmogenic nuclides, such as  $^{10}\text{Be}$  and  $^{26}\text{Al}$ , are routinely measured, permitting their application in a range of geomorphic scenarios and transforming the field of geomorphology. Measurements of cosmogenic nuclides have allowed the quantification of, for example, fault slip rates (e.g. Blisniuk et al., 2010; 2012), uplift rates (e.g. Ruzkiczay-Rüdiger et al., 2005; 2020), earthquake recurrence intervals (e.g. Schlagenhauf et al., 2011; Akçar et al., 2012), glacial (e.g. Jansen et al., 2019; Rand and Goehring, 2019), coastal (e.g. Hurst et al., 2016), and basin-wide (e.g. Brown et al., 1995; Granger et al., 1996; von Blanckenburg, 2005) erosion rates, and sediment storage (e.g. Hippe et al., 2012; Fülöp et al., 2020).

The most pertinent application of cosmogenic nuclide geochemistry to this dissertation is known as surface exposure dating. Ages are determined for fluctuations in ice masses based on the simple relationship between concentrations of nuclides and the time that has elapsed since a sample was exposed by a retreating ice mass, accounting for loss of nuclides by radioactive decay and erosion. In the first large-scale glacier chronology study using cosmogenic nuclides, Phillips et al. (1990) determined the ages of moraine sequences in the Sierra Nevada. Prior to the use of cosmogenic nuclide exposure dating, we were generally limited to determining the age of a moraine by determining min- and max-limiting bracketing ages using potentially sparse radiocarbon datable organic material (Balco, 2011). For cosmogenic nuclide exposure dating, one simply requires a fresh geomorphic surface, erratics, or depositional features such as moraines to generate a glacier chronology. The lithology and the materials available, and the presumed age of the geomorphic surface, determine the cosmogenic nuclides available for measurement. Quartz-bearing rock types are most commonly targeted because, not only are many established cosmogenic nuclides (with the exception of  $^{36}\text{Cl}$ ) produced within the quartz mineral lattice, but, owing to its simple, silicon dioxide composition,  $^{10}\text{Be}$ ,  $^{26}\text{Al}$ , and  $^{14}\text{C}$  are only produced in meaningful amounts on oxygen and silicon. Thus, other production pathways do not need to be accounted for.

Following on from glacier chronology studies that determined the ages of moraines, Brook et al. (1996) pioneered an approach in which a series of cosmogenic nuclide measurements are made from samples (bedrock or erratics) collected from the surface of a nunatak to constrain the former thickness of an adjacent ice mass or former ice mass (e.g. Ackert et al. 1999; Stone et al., 2003; Mackintosh et al., 2007; Corbett et al., 2019).

The use of cosmogenic nuclide exposure dating has rapidly grown in the decades following Phillips et al. (1990), with glacier chronology studies on all seven continents and encapsulating not only the most recent glaciation (e.g. Bentley et al., 2010, Goehring et al., 2011), but as far into the past as 14.5 million years (e.g. Sugden et al., 2017; Balter et al., 2020). By constraining the timing and extent of previous glaciations, cosmogenic nuclide measurements provide vital constraints for numerical ice sheet models (e.g. Whitehouse et al., 2012; Pollard et al., 2016). Thus, cosmogenic nuclide measurements indirectly form an integral part of helping to provide estimates of future sea-level rise, which, in turn, inform policy makers planning action to counter said sea-level rise scenarios .

### **1.1 Exposure dating challenges**

However, the use of surface exposure dating has not come without challenges. When undertaking a surface exposure dating study, we assume that measurements of cosmogenic nuclides are representative of the most recent period of exposure, i.e. when a sampling location most recently deglaciated. When a study site is covered by warm-based ice, an ice mass may erode to a sufficient depth over the duration of glaciation to remove material containing cosmogenic nuclides produced during prior periods of exposure. However, cold-based ice, which is not at the pressure melting point and is thus frozen to its bed, can preserve surfaces rather than erode them (e.g. Stroeven et al., 2002; Fabel et al., 2012). In the instance of non-erosive, cold-based ice cover, the only means to reduce cosmogenic nuclide concentrations is through radioactive decay. The most commonly measured cosmogenic nuclides are  $^{10}\text{Be}$  (half-life  $1.387 \pm 0.012$  Ma; Chmeleff et al., 2010; Korschinek et al., 2010) and  $^{26}\text{Al}$  (half-life  $705 \pm 17$  ka; Norris et al., 1983). With half-lives greater than the length of multiple glacial-interglacial cycles,  $^{10}\text{Be}$  and  $^{26}\text{Al}$  concentrations from previous periods of exposure will persist to the present when surfaces are buried by non-erosive ice during the LGM. Because they contain what is known as an inherited cosmogenic nuclide inventory, resulting exposure ages are older than the true age of the most recent deglaciation. For example, apparent exposure ages may predate the LGM, when in reality the samples were covered by cold-based ice and were uncovered following the LGM. Cosmogenic nuclide

inheritance may therefore produce ambiguous cosmogenic nuclide datasets, making it difficult, if not impossible, for researchers to make inferences using the resulting exposure ages.

## **1.2 Pervasive nuclide inheritance in the Weddell sector of Antarctica**

The potential inheritance of cosmogenic nuclides is a motivating factor for Chapter 2 of this thesis. The study site for Chapter 2 is the Weddell Sea Embayment (WSE) of Antarctica (Figure 1.1), a location where nuclide inheritance hindered glacier chronology studies. Multiple studies have made  $^{10}\text{Be}$  measurements from bedrock and/or erratics collected from nunataks around the embayment to study deglaciation in the region. Resulting  $^{10}\text{Be}$  exposure ages from the Shackleton Range (Hein et al., 2011), the Schmidt Hills in the Pensacola Mountains (Balco et al., 2016; Bentley et al., 2017), and the Lassiter Coast on the southern Antarctic Peninsula (Johnson et al., 2019; below) are primarily, or solely, pre-LGM aged (Figure 1.2).

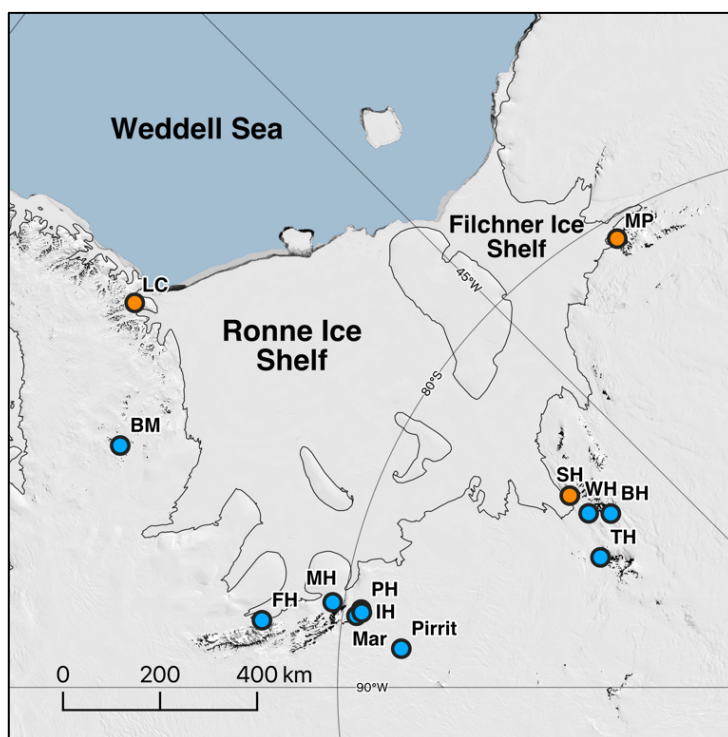


**Figure 1.1:** Map of the Weddell Sea Embayment. Orange dots are sites at which predominantly pre-LGM  $^{10}\text{Be}$  exposure ages are observed, indicative of no LGM thickening. Mount Provender (MP) in the Shackleton Range, the Schmidt Hills (SH), and the Lassiter Coast (LC). Blue dots are sites at which exposure age data indicate that ice was at least 380 to at least 1100 m thicker than present at the LGM. Behrendt Mountains (BM), Flower (FH), Meyer (MH), Patriot (PH), Independence (IH), Marble (Mar), Pirrit, Thomas (TH), and Williams (WH) Hills, and Mounts Harper and Bragg (HB). Base map is from the Quantarctica GIS package (Matsuoka et al., 2018).

At face value, one might interpret the ages in Fig. 1.2 as indicative of limited expansion of ice at the Lassiter Coast during the LGM. However, other exposure dating studies in the WSE have found evidence for a significantly vertically expanded ice sheet at the LGM. Post-LGM exposure ages show that ice was at least 1100 m thicker than present in the Ellsworth Mountains (Fogwill et al., 2014), and at least 380 to 500 m thicker than present in the Behrendt and Pensacola Mountains (Bentley et al., 2006; Balco et al., 2016; Bentley et al., 2017; Figure 1.1). Such a spatially variable pattern of ice thickness in the WSE at the LGM is glaciologically unlikely as it produces glacier surface slopes steeper than those of modern Antarctic glaciers (Balco et al., 2016) and is incompatible with flowline modelling (Whitehouse et al., 2017). If ice was indeed thicker than present at the sites lacking post-LGM exposure ages, they may have been covered by cold-based ice, preserving nuclide concentrations from previous periods of exposure with no LGM-aged drift deposited. To test if cold-based ice did cover study sites in the WSE at the LGM, we measured another cosmogenic nuclide that, owing to a short half-life, is less sensitive to inheritance; in situ produced  $^{14}\text{C}$ .

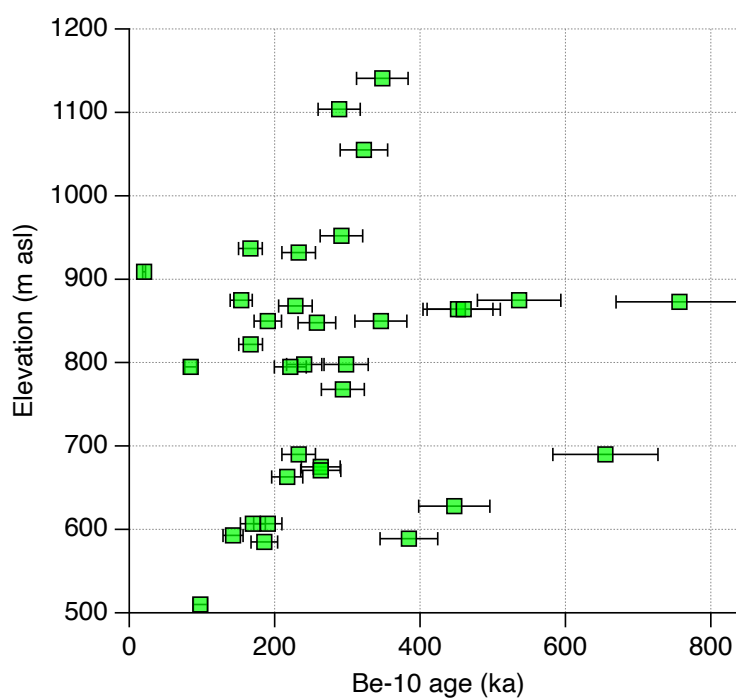


**Figure 1.2** Exposure ages from the Lassiter Coast (Johnson et al., 2019).

### **1.3 Why use in situ $^{14}\text{C}$ ?**

The short half-life of in situ  $^{14}\text{C}$  (5,730 yr) leads to two key advantages over long-lived nuclides. First, in situ  $^{14}\text{C}$  is less sensitive to inheritance when compared to longer lived nuclides. Because in situ

$^{14}\text{C}$  decays comparatively rapidly, concentrations are quickly reduced whilst buried by ice within a single glacial cycle. Thus, one does not need to rely on erosive ice cover to produce fresh surfaces following deglaciation.

A second advantage of using in situ  $^{14}\text{C}$  is that measurements can unambiguously show that a sample has been exposed through the LGM. A balance between production, decay, and removal by erosion, known as secular equilibrium, is achieved by radioactive cosmogenic nuclides after exposure for approximately 5.5 times that of their half-life. For  $^{14}\text{C}$ , secular equilibrium is attained after ca. 30 kyr of continuous exposure and a relatively low erosion rate, at which point a surface is described as being saturated with respect to  $^{14}\text{C}$ . Therefore, if a surface was uncovered during the LGM it will yield a  $^{14}\text{C}$  concentration equivalent to saturation. If a surface is covered by ice at the LGM, production ceases whilst the surface is buried, and the in situ  $^{14}\text{C}$  concentration decreases by ongoing radioactive decay.

One can apply the cosmogenic nuclide dipstick approach using a series of measurements of in situ  $^{14}\text{C}$ . If a nunatak was partially buried by ice during the LGM, a discontinuity will exist in the in situ  $^{14}\text{C}$  concentrations, at which point post-LGM exposure ages transition to saturated measurements, providing both an upper and lower constraint on the LGM thickness of the glacier. Ice must have been thicker than the highest-elevation sample yielding a post-LGM exposure age, but thinner than the lowest-elevation saturated sample. The ability to provide unambiguous evidence for the LGM thickness of an ice mass is a unique advantage of in situ  $^{14}\text{C}$ .

#### **1.4 In situ $^{14}\text{C}$ and preferred sampling material**

An interesting consequence of the increasing application of in situ  $^{14}\text{C}$  exposure dating is how the method may change the favoured sampling material of glacial geologists measuring cosmogenic nuclides. Cosmogenic nuclide studies investigating ice histories use erratics and/or bedrock for their sample material. Erratics are often the preferred choice, as they are arguably less likely to contain nuclide inheritance when compared to bedrock owing to their assumed subglacial source, where higher erosion rates are more likely to produce fresh geologic material. At the periphery of an ice sheet, ice is less likely to be at the pressure melting point, hindering erosion. Thus, glaciated surfaces at the periphery of an ice sheet, such as the surface of a nunatak, are less likely to be subject to high rates of erosion during glacial occupation. Owing to potentially lower erosion rates, bedrock samples collected from the surface of nunataks are therefore more likely to contain inheritance when compared to erratic cobbles. However, when measuring in situ  $^{14}\text{C}$ , bedrock and erratics can be considered equals with respect to their potential

for nuclide inheritance. In fact, bedrock is considered a more reliable target for in situ  $^{14}\text{C}$  dating compared to erratics, as erratics can be subject to unusual geomorphic circumstances that result in elevated in situ  $^{14}\text{C}$  concentrations. Although unlikely, sample material sourced from a mass movement event onto a glacier surface could be transported supraglacially to its sampling location (Balco et al., 2019). If the sample remains as supraglacial debris until it is deposited, and is transported rapidly, then the sample would have an elevated in situ  $^{14}\text{C}$  concentration relative to subglacially-derived cobbles deposited at the same location. The sample would have been subject to a higher cosmogenic nuclide production rate whilst residing at a higher elevation before being deposited at a lower elevation. Such geomorphic circumstances cannot influence bedrock, thus making bedrock a more favourable target for in situ  $^{14}\text{C}$  analysis.

### **1.5 Chapter 2 – In situ $^{14}\text{C}$ exposure dating in the Weddell Sea Embayment**

To summarise, Chapter 2 of this dissertation takes the form of an in situ  $^{14}\text{C}$  exposure dating study in the WSE, motivated by observations indicative of limited LGM thickening at numerous locations spanning the embayment (Sect. 1.0 and Figs. 1.1 and 1.2). The spatially variable pattern of LGM ice thickness is glaciologically unlikely (Balco et al., 2016; Whitehouse et al., 2017). The aim of Chapter 2 is to test for the burial of sites yielding solely or mostly pre-LGM  $^{10}\text{Be}$  exposure ages by cold based ice using measurements of in situ  $^{14}\text{C}$  along elevation transects. In situ  $^{14}\text{C}$  is used because of the insensitivity to nuclide inheritance owing to the short half-life of the nuclide.

I measured the in situ  $^{14}\text{C}$  content of bedrock and/or erratic cobbles collected from the Pensacola Mountains, Shackleton Range, and the Lassiter Coast (Fig. 1.1). The in situ  $^{14}\text{C}$  measurements I present are made from many of the same samples that were previously measured for primarily long-lived cosmogenic nuclides by Hein et al. (2011), Balco et al. (2016), and Johnson et al. (2019). Until recently, a large scale in situ  $^{14}\text{C}$  exposure dating study like that in Chapter 2 could not be undertaken due to difficulties in the extraction of the nuclide from quartz. The following section describes how  $^{14}\text{C}$  is extracted from quartz and the methodological advances that have allowed the undertaking of Chapter 2.

### **1.6 In situ $^{14}\text{C}$ extraction**

The potential for terrestrial in situ  $^{14}\text{C}$  to revolutionise the field of geomorphology was recognized in the late 1980s (Lal, 1988; Jull et al., 1992; Brook et al., 1995; Gosse et al., 1996), though

at the time there was no reliable method for extracting it from sample material. The method we use today to extract in situ  $^{14}\text{C}$  is the culmination of over three decades of methodological advances. The first measurements of in situ  $^{14}\text{C}$  from whole rock material were made from meteorites using pyrolysis (e.g. Goel and Kohman, 1962; Suess and Wänke, 1962). The production rate of in situ  $^{14}\text{C}$  in space is typically at least two orders of magnitude (ca. 200 to 1600 times) greater than that on Earth (Jull et al., 2013; Meszaros et al., 2018). Thus, as Lifton (1997) explains, sources of analytical variability in in situ  $^{14}\text{C}$  measurements are more important for terrestrial samples, but relatively insignificant for extraterrestrial ones. The first studies to isolate carbon from Earth materials extracted carbon from mid-oceanic basalts (e.g. Des Marais, 1978; Des Marais and Moore, 1984). By studying the isotopic content of carbon evolved at different temperature steps, Des Marais and Moore (1984) found that carbon contamination is released at temperatures up to 500 °C, with  $\text{CO}_2$  in vesicles and mantle-derived carbon ( $^{13}\text{C}$ ) released at higher temperatures. Building on this previous work, the first studies to measure the in situ  $^{14}\text{C}$  content of surficial terrestrial rocks were undertaken by Jull et al. (1989; 1992; 1994). However, procedural blanks were variable and on the scale of  $10^6$  atoms, too high to allow the routine measurement of in situ  $^{14}\text{C}$ . The PhD work of Lifton (1997) and a follow up study by Lifton et al. (2001) then developed the method that is the basis for all in situ  $^{14}\text{C}$  extraction lines in use today. Lifton (1997) found that, similarly to the findings of Des Marais and Moore (1984),  $^{14}\text{C}$  contamination is released at temperatures at or below 500 °C, and in situ  $^{14}\text{C}$  is released at temperatures between 500 and 1500 °C. Extraction techniques have been improved over the following two decades (e.g. Hippe et al., 2009; Pigati et al., 2010a; Lifton et al., 2015; Goehring et al., 2019; Lamp et al., 2019). Lowering of system blanks, the adoption of the quartz interlaboratory comparison material CRONUS-A (Jull et al., 2015), and the automation of extraction (Lifton et al., 2015; Goehring et al., 2019) have contributed toward making in situ  $^{14}\text{C}$  a now routinely measured cosmogenic nuclide.

### **1.7 In situ $^{14}\text{C}$ extraction lines**

In situ  $^{14}\text{C}$  extraction lines contain three to four key components: (1) a system that liberates in situ  $^{14}\text{C}$  from quartz and converts it to  $\text{CO}_2$ ; (2) a  $\text{CO}_2$  purification system that removes contaminant gasses; (3) a component that measures the pressure of  $\text{CO}_2$  released and consequently the amount of native carbon; and (4) a dilution and graphitisation system, the latter following the method of Slota et al. (1987) or Southon (2007). To liberate carbon from quartz, samples are step heated, first at 500 °C to

remove atmospheric contamination, then at 1100 to 1670 °C to liberate the in situ component (Lifton et al., 2001). With the exception of large samples (ca. >100 µg of carbon and depending on the AMS system), the CO<sub>2</sub> released from a sample is diluted with <sup>14</sup>C-dead CO<sub>2</sub> to help permit graphitisation and lower the background from modern <sup>14</sup>C. A gaseous sample split is also collected for stable carbon isotope analysis. Some laboratories use gaseous samples for AMS analysis and thus do not require a graphitisation system (e.g. Lupker et al., 2019; Fülöp et al., 2019).

There are four types of extraction lines in use at present. The first follows the method of Lifton et al. (2001) and Pigati et al. (2010a) using the fusion of quartz in a LiBO<sub>2</sub> flux with a high heat step of 1100 °C (Lifton et al., 2015; Kim et al., 2016; Tikhomirov et al., 2016; Goehring et al., 2019; Lamp et al., 2019). An O<sub>2</sub> carrier gas carries evolved gases for secondary oxidation of carbon species to CO<sub>2</sub>, which is then purified and graphitised. The second type of extraction line uses a furnace that can reach temperatures of 1600 °C, relying on high temperature diffusion to liberate in situ <sup>14</sup>C from quartz and removing the need for a flux (Hippe et al., 2009; 2013; Lupker et al., 2019). There is no sample dilution or graphitisation, as carbon isotope ratios are measured using gaseous samples. Another type of extraction line combusts quartz in sealed tubes in the presence of a CaCO<sub>3</sub> carrier with a high temperature heat step at 1650 °C, again with no flux and no graphitisation (Fülöp et al., 2015, 2019; Ermini et al., 2019; Schiffer et al., 2020). The final type of extraction line combines aspects of types one and two, employing a LiBO<sub>2</sub> flux but sending gaseous samples for AMS analysis (Paige et al., 2017; 2018a,b).

The methodological advances outlined above have facilitated a rapid increase in the number of studies using in situ <sup>14</sup>C over the last few years, in addition to making possible an in situ <sup>14</sup>C study on the relatively large scale of that presented in Chapter 2. There are now at least ten laboratories with the capability of extracting in situ <sup>14</sup>C from quartz, with seven reporting routine measurements. Only ten studies published from 1989 to 2010 applied in situ <sup>14</sup>C measurements. When I started my PhD studies in 2015, there were 20 published studies applying in situ <sup>14</sup>C measurements. By 2020, the number of studies using in situ <sup>14</sup>C has increased to 43, with 12 alone published in 2019. Including extraction line performance updates, methodological advances, theses, and technical reports, the number of in situ <sup>14</sup>C studies by mid-2020 stands at 63. The number of studies applying measurements of in situ <sup>14</sup>C is likely to continue to rise at a rapid rate, perhaps even more so if more extraction lines are built and enter routine use, more lines incorporate automation, and if methods to reliably extract it from other minerals such as



olivine and feldspars are developed (Handwerker et al., 1999; Pigati et al., 2010b). The latter would greatly increase the geographic area with rock types suitable for making in situ  $^{14}\text{C}$  measurements.

### **1.8 Chapter 3 – Carbon contamination from quartz isolation**

In addition to decades of in situ  $^{14}\text{C}$  extraction method development, I had to overcome methodological challenges before completing measurements of in situ  $^{14}\text{C}$  for Chapter 2. As stated above, barring unlikely geomorphic circumstances, the in situ  $^{14}\text{C}$  saturation concentration for a study site cannot be exceeded. However, whilst measuring in situ  $^{14}\text{C}$  from samples presented in Chapter 2, as well as measurements for external projects, I observed concentrations exceeding saturation concentrations (Figure 1.3). The quartz for these samples was isolated at external institutions. Additional etching, following typical procedures using HF and  $\text{HNO}_3$ , of samples yielded lower, though still in excess of saturation, in situ  $^{14}\text{C}$  concentrations. Suspecting that  $^{14}\text{C}$  contamination was sourced from the varying quartz isolation procedures used at different laboratories, we isolated quartz from the same samples from whole rock at Tulane, after which we observed lower and geologically-plausible in situ  $^{14}\text{C}$  concentrations. We ruled out systematic measurement issues through repeat measurements of interlaboratory and other samples, after which we suspected that the source of elevated in situ  $^{14}\text{C}$  concentrations was part of the quartz isolation procedure known as froth flotation. A commonly-used technique, froth flotation is used to separate quartz from feldspars and involves the use of multiple organic compounds (laurylamine and eucalyptus oil) which, with modern carbon sources, are potential sources of contamination. We thus set out to investigate the source of  $^{14}\text{C}$  contamination through a systematic study. We isolated quartz from the same whole rock material using different methods to find the potential source of contamination. We also measured the carbon isotope ratio of laurylamine to find out if our laurylamine has a modern carbon source. Finally, we present a standard procedure for the isolation of quartz for in situ  $^{14}\text{C}$  analysis that can be followed to avoid contamination from froth flotation.

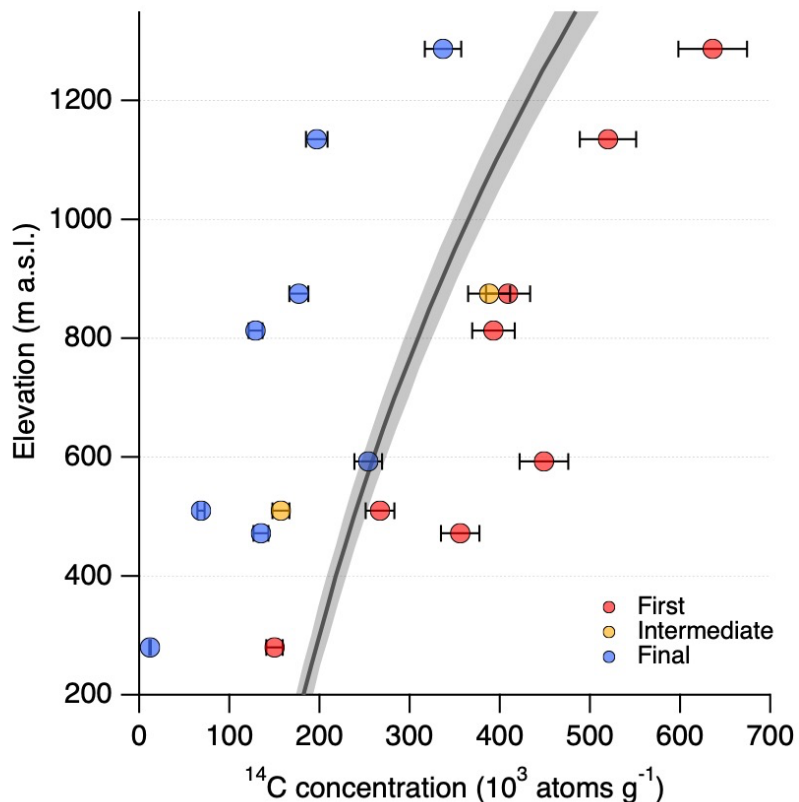


**Figure 1.3:** Elevation versus in situ  $^{14}\text{C}$  concentration of samples that initially yielded anomalously high  $^{14}\text{C}$  concentrations. Measurements at the same elevation are from the same sample. For each sample, the highest in situ  $^{14}\text{C}$  concentration is sourced from the first measurement (red). For the two samples measured three times at 510 and 875 m a.s.l., the intermediate measurement was made following additional etching and yields the intermediate in situ  $^{14}\text{C}$  concentration (yellow). The final measurement (blue) for each sample was made from quartz isolated from whole rock at Tulane. Thick grey line and grey shading are the saturation concentration and associated error envelope. Sourced from Chapter 3 (Figure 3.1).

#### **1.7 Chapter 4 – Evaluating ice sheet model outputs with cosmogenic nuclide measurements**

After identifying the likely source of contamination causing elevated in situ  $^{14}\text{C}$  concentrations and outlining a method to avoid it, we were confident in our ability to measure the in situ  $^{14}\text{C}$  concentration of samples for Chapter 2. The exposure ages presented in Chapter 2 constrain the LGM thickness and pattern of deglaciation at three sites around the WSE. Additionally, Spector et al. (2019) published LGM constraints for two sites in the WSE; the Pirrit Hills and the Whitmore Mountains (Figure 1.1). There is now a large dataset of exposure ages constraining the LGM-to-present configuration and behaviour of the AIS in the WSE. Many numerical ice sheet models or ice loading histories use measurements of cosmogenic nuclides to constrain their models, through, for example, their use in the scoring of ensemble members (e.g. Pollard et al., 2016; 2017) for the former, or iterative adjustment to

satisfy constraints for the latter (Argus et al., 2014). In Chapter 3, we review all post-LGM  $^{10}\text{Be}$  and in situ  $^{14}\text{C}$  exposure ages from the WSE to evaluate the outputs of numerical ice sheet models published over the last decade, but prior to the majority of exposure dating studies in the WSE. We use the exposure age dataset to locate where ice sheet model outputs are inconsistent, or not inconsistent, with geologic constraints. We look at both the LGM configuration of the ice sheet predicted by different ice sheet models, as well as the timing and rate of deglaciation predicted around the embayment. Through our evaluation, we hope to aid future modelling studies by identifying locations with large misfits, as well as places where thinning may occur too early or late, as well as too rapidly or slowly, than indicated by exposure ages. We also discuss future avenues of research in the WSE with respect to modelling efforts and exposure dating studies.

### **1.8 Summary of chapters**

To summarise, this dissertation is focussed primarily on advancing in situ  $^{14}\text{C}$  as a tool for understanding past ice sheet change and using it to study deglaciation in the WSE. In Chapter 2 I present an in situ  $^{14}\text{C}$  exposure dating study in which we measure the in situ  $^{14}\text{C}$  content of samples collected from around the WSE that yield  $^{10}\text{Be}$  ages exceeding the last glacial period. Chapter 3 describes an investigation into anomalously-high measurements of in situ  $^{14}\text{C}$  made whilst undertaking Chapter 2, including efforts to identify the source of the elevated  $^{14}\text{C}$  concentrations, as well as a standard procedure for the isolation of quartz from whole rock material for in situ  $^{14}\text{C}$  analysis. Chapter 4 describes how cosmogenic nuclide measurements can be used to constrain numerical ice sheet models and, using all post-LGM exposure ages from the WSE, I evaluate numerical ice sheet model outputs to help inform those modelling the WSE in the future.

### **1.8 References**

- Ackert, R. P., Barclay, D. J., Jr, H. W. B., Calkin, P. E., Kurz, M. D., Fastook, J. L., Steig, E. J., Jr, R. P. A., Barclay, D. J. and Jr, H. W. B.: Measurements of Past Ice Sheet Elevations in Interior West Antarctica Published by: American Association for the Advancement of Science Stable URL: <http://www.jstor.org/stable/2899686>, Science (80-. ), 286(5438), 276–280, 1999.
- Akçar, N., Tikhomirov, D., Özkaymak, Ç., Ivy-Ochs, S., Alfimov, V., Sözbilir, H., Uzel, B. and

- Schlüchter, C.:  $^{36}\text{Cl}$  exposure dating of paleoearthquakes in the Eastern Mediterranean: First results from the western Anatolian Extensional Province, Manisa fault zone, Turkey, *Bull. Geol. Soc. Am.*, 124(11–12), 1724–1735, doi:10.1130/B30614.1, 2012.
- Argus, D. F., Peltier, W. R., Drummond, R. and Moore, A. W.: The Antarctica component of postglacial rebound model ICE-6G\_C (VM5a) based on GPS positioning, exposure age dating of ice thicknesses, and relative sea level histories, *Geophys. J. Int.*, 198(1), 537–563, doi:10.1093/gji/ggu140, 2014.
- Balco, G., Todd, C., Goehring, B.M., Moening-Swanson, I., Nichols, K.: Glacial geology and cosmogenic-nuclide exposure ages from the Tucker Glacier - Whitehall Glacier confluence, northern Victoria Land, Antarctica, *Am. J. Sci.*, 319(April), 255–286, doi:10.2475/04.2019.01, 2019.
- Balco, G.: Contributions and unrealized potential contributions of cosmogenic-nuclide exposure dating to glacier chronology, 1990-2010, *Quat. Sci. Rev.*, 30(1–2), 3–27, doi:10.1016/j.quascirev.2010.11.003, 2011.
- Balco, G., Todd, C., Huybers, K., Campbell, S., Vermeulen, M., Hegland, M., Goehring, B. M. and Hillebrand, T. R.: Cosmogenic-nuclide exposure ages from the Pensacola Mountains adjacent to the foundation ice stream, Antarctica, *Am. J. Sci.*, 316(6), 542–577, doi:10.2475/06.2016.02, 2016.
- Balter, A., Bromley, G., Balco, G., Thomas, H. and Jackson, M. S.: A 14.5 million-year record of East Antarctic Ice Sheet fluctuations from the central Transantarctic Mountains, constrained with cosmogenic  $^3\text{He}$ ,  $^{10}\text{Be}$ ,  $^{21}\text{Ne}$ , and  $^{26}\text{Al}$ , *Cryosph. Discuss.*, in review(March), doi:10.5194/tc-2020-57, 2020.
- Bentley, M. J., Fogwill, C. J., Kubik, P. W. and Sugden, D. E.: Geomorphological evidence and cosmogenic  $^{10}\text{Be}/^{26}\text{Al}$  exposure ages for the Last Glacial Maximum and deglaciation of the Antarctic Peninsula Ice Sheet, *Bull. Geol. Soc. Am.*, 118(9–10), 1149–1159, doi:10.1130/B25735.1, 2006.
- Bentley, M. J., Fogwill, C. J., Brocq, A. M. Le, Hubbard, A. L., Sugden, D. E., Dunai, T. J. and Freeman, S. P. H. T.: Deglacial history of the West Antarctic Ice Sheet in the Weddell Sea embayment: Constraints on past ice volume change, *Geol. Soc. Am.*, 38(5), 411–

414, doi:10.1130/G30754.1, 2010.

- Bentley, M. J., Hein, A. S., Sugden, D. E., Whitehouse, P. L., Shanks, R., Xu, S. and Freeman, S. P. H. T.: Deglacial history of the Pensacola Mountains, Antarctica from glacial geomorphology and cosmogenic nuclide surface exposure dating, *Quat. Sci. Rev.*, 158, 58–76, doi:10.1016/j.quascirev.2016.09.028, 2017.
- von Blanckenburg, F.: The control mechanisms of erosion and weathering at basin scale from cosmogenic nuclides in river sediment, *Earth Planet. Sci. Lett.*, 237(3–4), 462–479, doi:10.1016/j.epsl.2005.06.030, 2005.
- Blisniuk, K., Rockwell, T., Owen, L. A., Oskin, M., Lippincott, C., Caffee, M. W. and Dortch, J.: Late Quaternary slip rate gradient defined using high-resolution topography and  $^{10}\text{Be}$  dating of offset landforms on the southern San Jacinto Fault zone, California, *J. Geophys. Res. Solid Earth*, 115(8), doi:10.1029/2009JB006346, 2010.
- Blisniuk, K., Oskin, M., Fletcher, K., Rockwell, T. and Sharp, W.: Assessing the reliability of U-series and  $^{10}\text{Be}$  dating techniques on alluvial fans in the Anza Borrego Desert, California, *Quat. Geochronol.*, 13, 26–41, doi:10.1016/j.quageo.2012.08.004, 2012.
- Brook, E. J., Brown, E. T., Kurz, M. D., Ackert, R. P., Raisbeck, G. M. and Yiou, F.: Constraints on age, erosion, and uplift of Neogene glacial deposits in the Transantarctic Mountains determined from in situ cosmogenic  $^{10}\text{Be}$  and  $^{26}\text{Al}$ , *Geology*, 23(12), 1063–1066, 1995.
- Brown, E. T., Stallard, R. F., Larsen, M. C., Raisbeck, G. M. and Yiou, F.: Denudation rates determined from the accumulation of in situ-produced  $^{10}\text{Be}$  in the Luquillo experimental forest, Puerto Rico, *Earth Planet. Sci. Lett.*, 129(1–4), 193–202, doi:10.1016/0012-821X(94)00249-X, 1995.
- Chmeleff, J., Blanckenburg, F. Von, Kossert, K. and Jakob, D.: Determination of the  $^{10}\text{Be}$  half-life by multicollector ICP-MS and liquid scintillation counting, *Nucl. Inst. Methods Phys. Res. B*, 268(2), 192–199, doi:10.1016/j.nimb.2009.09.012, 2010.
- Corbett, L. B., Bierman, P. R., Wright, S. F., Shakun, J. D., Davis, P. T., Goehring, B. M., Halsted, C. T., Koester, A. J., Caffee, M. W. and Zimmerman, S. R.: Analysis of multiple cosmogenic nuclides constrains Laurentide Ice Sheet history and process on Mt. Mansfield, Vermont's highest peak, *Quat. Sci. Rev.*, 205, 234–246,

doi:10.1016/j.quascirev.2018.12.014, 2019.

Ermini, M., Schimmelpfennig, I., Keddadouche, K., Tuna, T., Bard, E., Lupker, M., Hippe, K. and Benedetti, L.: Status of the in situ <sup>14</sup>C extraction system at CEREGE (Aix-en-Provence, France), in Goldschmidt., 2019.

Fabel, D., Ballantyne, C. K. and Xu, S.: Trimlines, blockfields, mountain-top erratics and the vertical dimensions of the last British-Irish Ice Sheet in NW Scotland, *Quat. Sci. Rev.*, 55, 91–102, doi:10.1016/j.quascirev.2012.09.002, 2012.

Fogwill, C. J., Turney, C. S. M., Golledge, N. R., Rood, D. H., Hippe, K., Wacker, L., Wieler, R., Rainsley, E. B. and Jones, R. S.: Drivers of abrupt Holocene shifts in West Antarctic ice stream direction determined from combined ice sheet modelling and geologic signatures, *Antarct. Sci.*, 26(6), 674–686, doi:10.1017/S0954102014000613, 2014.

Fülöp, R. H., Wacker, L. and Dunai, T. J.: Progress report on a novel in situ <sup>14</sup>C extraction scheme at the University of Cologne, *Nucl. Instruments Methods Phys. Res. Sect. B Beam Interact. with Mater. Atoms*, 361, 20–24, doi:10.1016/j.nimb.2015.02.023, 2015.

Fülöp, R. H., Fink, D., Yang, B., Codilean, A. T., Smith, A., Wacker, L., Levchenko, V. and Dunai, T. J.: The ANSTO – University of Wollongong in-situ<sup>14</sup>C extraction laboratory, *Nucl. Instruments Methods Phys. Res. Sect. B Beam Interact. with Mater. Atoms*, (January), 0–1, doi:10.1016/j.nimb.2018.04.018, 2019.

Fülöp, R. H., Codilean, A. T., Wilcken, K. M., Cohen, T. J., Fink, D., Smith, A. M., Yang, B., Levchenko, V. A., Wacker, L., Marx, S. K., Stromsoe, N., Fujioka, T. and Dunai, T. J.: Million-year lag times in a post-orogenic sediment conveyor, *Sci. Adv.*, 6(25), doi:10.1126/sciadv.aaz8845, 2020.

Goehring, B. M., Schaefer, J. M., Schluechter, C., Lifton, N. A., Finkel, R. C., Jull, A. J. T., Akçar, N. and Alley, R. B.: The Rhone Glacier was smaller than today for most of the Holocene, *Geology*, 39(7), 679–682, doi:10.1130/G32145.1, 2011.

Goehring, B. M., Wilson, J. and Nichols, K.: A fully automated system for the extraction of in situ cosmogenic carbon-14 in the Tulane University cosmogenic nuclide laboratory, *Nucl. Instruments Methods Phys. Res. Sect. B Beam Interact. with Mater. Atoms*, doi:10.1016/j.nimb.2019.02.006, 2019a.

- Goehring, B. M., Balco, G., Todd, C., Moening-Swanson, I. and Nichols, K.: Late-glacial grounding line retreat in the northern Ross Sea, Antarctica, *Geology*, 47(4), 1–4, doi:10.1130/G45413.1, 2019b.
- Goel, P.S., Kohman, P. K.: Cosmogenic Carbon-14 in Meteorites and Terrestrial Ages of “Finds” and Craters, *Science* (80-. ), 136(3519), 875–876, 1962.
- Gosse, John C., Reedy, R.C., Harrington, C.D., Poths, J.: Overview of the workshop on secular variations in production rates of cosmogenic nuclides on Earth, *Radiocarbon*, 38(1), 135–147, 1996.
- Granger, D. E., Kirchner, J. W. and Finkel, R.: Spatially averaged long-term erosion rates measured from in situ-produced cosmogenic nuclides in alluvial sediment, *J. Geol.*, 104(3), 249–257, doi:10.1086/629823, 1996.
- Handwerger, D. A., Cerling, T. E. and Bruhn, R. L.: Cosmogenic  $^{14}\text{C}$  in carbonate rocks, *Geomorphology*, 27(1–2), 13–24, doi:10.1016/S0169-555X(98)00087-7, 1999.
- Hein, A. S., Fogwill, C. J., Sugden, D. E. and Xu, S.: Glacial/interglacial ice-stream stability in the Weddell Sea embayment, Antarctica, *Earth Planet. Sci. Lett.*, 307(1–2), 211–221, doi:10.1016/j.epsl.2011.04.037, 2011.
- Hippe, K., Kober, F., Baur, H., Ruff, M., Wacker, L. and Wieler, R.: The current performance of the in situ  $^{14}\text{C}$  extraction line at ETH, *Quat. Geochronol.*, 4(6), 493–500, doi:10.1016/j.quageo.2009.06.001, 2009.
- Hippe, K., Kober, F., Zeilinger, G., Ivy-Ochs, S., Maden, C., Wacker, L., Kubik, P. W. and Wieler, R.: Quantifying denudation rates and sediment storage on the eastern Altiplano, Bolivia, using cosmogenic  $^{10}\text{Be}$ ,  $^{26}\text{Al}$ , and in situ  $^{14}\text{C}$ , *Geomorphology*, 179, 58–70, doi:10.1016/j.geomorph.2012.07.031, 2012.
- Hippe, K., Kober, F., Wacker, L., Fahrni, S. M., Ivy-Ochs, S., Akçar, N., Schlüchter, C. and Wieler, R.: An update on in situ cosmogenic  $^{14}\text{C}$  analysis at ETH Zürich, *Nucl. Instruments Methods Phys. Res. Sect. B Beam Interact. with Mater. Atoms*, 294, 81–86, doi:10.1016/j.nimb.2012.06.020, 2013.
- Hippe, K., Ivy-Ochs, S., Kober, F., Zasadni, J., Wieler, R., Wacker, L., Kubik, P. W. and Schlüchter, C.: Chronology of Lateglacial ice flow reorganization and deglaciation in the Gotthard Pass area, Central Swiss Alps, based on cosmogenic  $^{10}\text{Be}$  and in situ  $^{14}\text{C}$ , *Quat.*

- Geochronol., 19, 14–26, doi:10.1016/j.quageo.2013.03.003, 2014.
- Hurst, M. D., Rood, D. H., Ellis, M. A., Anderson, R. S. and Dornbusch, U.: Recent acceleration in coastal cliff retreat rates on the south coast of Great Britain, *Proc. Natl. Acad. Sci.*, 113(47), 13336–13341, doi:10.1073/pnas.1613044113, 2016.
- Jansen, J. D., Knudsen, M. F., Andersen, J. L., Heyman, J. and Egholm, D. L.: Erosion rates in Fennoscandia during the past million years, *Quat. Sci. Rev.*, 207, 37–48, doi:10.1016/j.quascirev.2019.01.010, 2019.
- Johnson, J. S., Nichols, K. A., Goehring, B. M., Balco, G. and Schaefer, J. M.: Abrupt mid-Holocene ice loss in the western Weddell Sea Embayment of Antarctica, *Earth Planet. Sci. Lett.*, 518, 127–135, doi:10.1016/j.epsl.2019.05.002, 2019.
- Jull, A.J.T, Wilson, A.E., Burr, G.S., Toolin, L.J., Donahue, D. J.: Measurements of Cosmogenic Produced By Spallation in High-Altitude Rocks, *Radiocarbon*, 34(3), 737–744, 1992.
- Jull, A.J.T., Lifton, N., Phillips, W.M., Quade, J. Studies of the production rate of cosmic-ray produced  $^{14}\text{C}$  in rock surfaces, *Nucl. Instruments Methods Phys. Res. Sect. B Beam Interact. with Mater. Atoms*, 92(1-4), 308–310, [https://doi.org/10.1016/0168-583X\(94\)96024-0](https://doi.org/10.1016/0168-583X(94)96024-0), 1994.
- Jull, A. J. T., Donahue, D. J., Linick, T. W. and Wilson, G. C.: Spallogenic  $^{14}\text{C}$  in high-altitude rocks and in Antarctic meteorites, *Radiocarbon*, 31(3), 719–724, 1989.
- Jull, A. J. T., Giscard, M. D., Hutzler, A., Schnitzer, C. J., Zahn, D., Burr, G. S., McHargue, L. R. and Hill, D.: Radionuclide Studies of Stony Meteorites from Hot Deserts, *Radiocarbon*, 55(3), 1779–1789, doi:10.1017/s0033822200048682, 2013.
- Jull, A. J. T., Scott, E. M. and Bierman, P.: The CRONUS-Earth inter-comparison for cosmogenic isotope analysis, *Quat. Geochronol.*, 26(1), 3–10, doi:10.1016/j.quageo.2013.09.003, 2015.
- Kim, D. E., Seong, Y. B., Byun, J., Weber, J. and Min, K.: Geomorphic disequilibrium in the Eastern Korean Peninsula: Possible evidence for reactivation of a rift-flank margin, *Geomorphology*, 254, 130–145, doi:10.1016/j.geomorph.2015.11.022, 2016.
- Korschinek, G., Bergmaier, A., Faestermann, T., Gerstmann, U. C., Knie, K., Rugel, G., Wallner, A., Dillmann, I., Dollinger, G., Lierse von Gostomski, C., Kossert, K., Maiti, M., Poutivtsev, M. and Remmert, A.: A new value for the half-life of  $^{10}\text{Be}$  by Heavy-Ion



- Elastic Recoil Detection and liquid scintillation counting, *Nucl. Instr. Methods Phys. Res. B*, 268(2), 187–191, doi:10.1016/j.nimb.2009.09.020, 2010.
- Lal, D.: In situ produced cosmogenic isotopes in terrestrial rocks, *Annu. Rev. Earth Planet. Sci.*, 16, 355–388, 1988.
- Lamp, J. L., Young, N. E., Koffman, T., Schimmelpfennig, I., Tuna, T., Bard, E. and Schaefer, J. M.: Update on the cosmogenic in situ <sup>14</sup>C laboratory at the Lamont-Doherty Earth Observatory, *Nucl. Instruments Methods Phys. Res. Sect. B Beam Interact. with Mater. Atoms*, (April), 1–6, doi:10.1016/j.nimb.2019.05.064, 2019.
- Lifton, N., Goehring, B., Wilson, J., Kubley, T. and Caffee, M.: Progress in automated extraction and purification of in situ <sup>14</sup>C from quartz: Results from the Purdue in situ <sup>14</sup>C laboratory, *Nucl. Instruments Methods Phys. Res. Sect. B Beam Interact. with Mater. Atoms*, 361, 381–386, doi:10.1016/j.nimb.2015.03.028, 2015.
- Lifton, N. A.: A new extraction technique and production rate estimate for in situ cosmogenic <sup>14</sup>C in quartz, PhD Dissertation, University of Arizona., 1997.
- Lifton, N. A., Jull, A. J. T. and Quade, J.: A new extraction technique and production rate estimate for in situ cosmogenic <sup>14</sup>C in quartz, *Geochim. Cosmochim. Acta*, 65(12), 1953–1969, doi:10.1016/S0016-7037(01)00566-X, 2001.
- Lupker, M., Hippe, K., Wacker, L., Steinemann, O., Tikhomirov, D., Maden, C., Haghpor, N. and Synal, H. A.: In-situ cosmogenic <sup>14</sup>C analysis at ETH Zürich: Characterization and performance of a new extraction system, *Nucl. Instruments Methods Phys. Res. Sect. B Beam Interact. with Mater. Atoms*, 457(July), 30–36, doi:10.1016/j.nimb.2019.07.028, 2019.
- Mackintosh, A., White, D., Fink, D., Gore, D. B., Pickard, J. and Fanning, P. C.: Exposure ages from mountain dipsticks in Mac. Robertson Land, East Antarctica, indicate little change in ice-sheet thickness since the Last Glacial Maximum, *Geology*, 35(6), 551–554, doi:10.1130/G23503A.1, 2007.
- Des Marais, D. J.: Variable-Temperature Cryogenic Trap for the Separation of Gas Mixtures, *Anal. Chem.*, 50(9), 1405–1406, doi:10.1021/ac50031a056, 1978.
- Des Marais, D. J. and Moore, J. G.: Carbon and its isotopes in mid-oceanic basaltic glasses, *Earth Planet. Sci. Lett.*, 69(1), 43–57, doi:10.1016/0012-821X(84)90073-6, 1984.

- Matsuoka, K., Skoglund, A., & Roth, G. (2018). Quantarctica [Data set]. Norwegian Polar Institute. <https://doi.org/10.21334/npolar.2018.8516e961>
- Mészáros, M., Leya, I., Hofmann, B. A. and Szidat, S.: Current performance and preliminary results of a new  $^{14}\text{C}$  extraction line for meteorites at the University of Bern, *Radiocarbon*, 60(2), 601–615, doi:10.1017/RDC.2017.114, 2018.
- Norris, T. L., Gancarz, A. J., Rokop, D. J. and Thomas, K. W.: Half-Life of  $^{26}\text{Al}$ , *J. Geophys. Res.*, 88, B331–B333, 1983.
- Paige, C., Gosse, J., Margreth, A. and Wacker, L.: Development of a cosmogenic  $^{14}\text{C}$  extraction line at Dalhousie University, in EGU General Assembly, vol. 20., 2018a.
- Paige, C. A., Gosse, J. C., Taylor, K. and Margreth, A.: Atlantic Geoscience Society Abstracts: 43rd Annual Colloquium & General Meeting 2017, in *Atlantic Geology*, vol. 53., 2017.
- Paige, C. A., Gosse, J. C., Taylor, K., Margreth, A., Wacker, L. and Lifton, N. A.: Canada's first in situ  $^{14}\text{C}$  extraction line is ready for action, in *Atlantic Geology*, vol. 54, pp. 081–132., 2018b.
- Phillips, F. M., Zreda, M. G., Smith, S. S., Elmore, D., Kubik, P. W. and Sharma, P.: Cosmogenic Chlorine-36 Chronology for Glacial Deposits at Bloody Canyon, Eastern Sierra Nevada, *Science*, 248(4962), 1529–1532, doi: 10.1126/science.248.4962.1529
- Pigati, J.S., Lifton, N.A., Jull, A.J.T., Quade, J.: Extraction of in situ cosmogenic  $^{14}\text{C}$  from olivine, *Radiocarbon*, 52(2–3), 1244–1260, doi:10.1063/1.1478845, 2010.
- Pigati, J. S., Lifton, N. A., Jull, A. J. T. and Quade, J.: A simplified in situ cosmogenic  $^{14}\text{C}$  extraction system, *Radiocarbon*, 52(2–3), 1236–1243, 2010.
- Pollard, D., Chang, W., Haran, M., Applegate, P. and DeConto, R.: Large ensemble modeling of the last deglacial retreat of the West Antarctic Ice Sheet: Comparison of simple and advanced statistical techniques, *Geosci. Model Dev.*, 9(5), 1697–1723, doi:10.5194/gmd-9-1697-2016, 2016.
- Pollard, D., Gomez, N. and DeConto, R. M.: Variations of the Antarctic Ice Sheet in a Coupled Ice Sheet-Earth-Sea Level Model: Sensitivity to Viscoelastic Earth Properties, *J. Geophys. Res. Earth Surf.*, 122(11), 2124–2138, doi:10.1002/2017JF004371, 2017.
- Rand, C. and Goehring, B. M.: The distribution and magnitude of subglacial erosion on millennial timescales at Engabreen, Norway, *Ann. Glaciol.*, 60(80), 73–81,

doi:10.1017/aog.2019.42, 2019.

- Ruszkiczay-Rüdiger, Z., Fodor, L., Bada, G., Leél-Össy, S., Horváth, E. and Dunai, T. J.: Quantification of Quaternary vertical movements in the central Pannonian Basin: A review of chronologic data along the Danube River, Hungary, *Tectonophysics*, 410(1–4), 157–172, doi:10.1016/j.tecto.2005.05.048, 2005.
- Ruszkiczay-Rüdiger, Z., Balázs, A., Csillag, G., Drijkoningen, G. and Fodor, L.: Uplift of the Transdanubian Range, Pannonian Basin: How fast and why?, *Glob. Planet. Change*, 192(March), 103263, doi:10.1016/j.gloplacha.2020.103263, 2020.
- Schiffer, M., Stolz, A., López, D. A., Spanier, R., Herb, S., Müller-Gatermann, C., Heinze, S., Binnie, S., Melchert, J., Kivel, N., Schumann, D., Rethemeyer, J., Dunai, T. and Dewald, A.: Method developments for accelerator mass spectrometry at CologneAMS,  $^{53}\text{Mn}/^{3}\text{He}$  burial dating and ultra-small  $^{14}\text{CO}_2$  samples, *Glob. Planet. Change*, 184(September 2019), doi:10.1016/j.gloplacha.2019.103053, 2020.
- Schlagenhauf, A., Manighetti, I., Benedetti, L., Gaudemer, Y., Finkel, R., Malavieille, J. and Pou, K.: Earthquake supercycles in Central Italy, inferred from  $^{36}\text{Cl}$  exposure dating, *Earth Planet. Sci. Lett.*, 307(3–4), 487–500, doi:10.1016/j.epsl.2011.05.022, 2011.
- Slota, P.J.Jr., Jull, A.J.T., Linick, T.W., Toolin, L. J.: Preparation of small samples for  $^{14}\text{C}$  accelerator targets by catalytic reduction of  $\text{CO}$ , *Radiocarbon*, 29(29), 303–306, doi:10.1017/S0033822200056988, 1987.
- Southon, J.: Graphite reactor memory - Where is it from and how to minimize it?, *Nucl. Instruments Methods Phys. Res. Sect. B Beam Interact. with Mater. Atoms*, 259(1), 288–292, doi:10.1016/j.nimb.2007.01.251, 2007.
- Spector, P., Stone, J. and Goehring, B.: Thickness of the divide and flank of the West Antarctic Ice Sheet through the last deglaciation, *Cryosphere*, 13(11), 3061–3075, doi:10.5194/tc-13-3061-2019, 2019.
- Stone, J. O., Balco, G. A., Sugden, D. E., Caffee, M. W., Sass, L. C., Cowderly, S. G. and Siddoway, C.: Holocene deglaciation of Marie Byrd Land, West Antarctica, *Science* (80-. ), 299(5603), 99–102, doi:10.1126/science.1077998, 2003.
- Stroeven, A. P., Fabel, D., Harbor, J., Hättestrand, C. and Kleman, J.: Quantifying the erosional impact of the Fennoscandian ice sheet in the Torneträsk-Narvik corridor, northern

- Sweden, based on cosmogenic radionuclide data, *Geogr. Ann. Ser. A Phys. Geogr.*, 84(3–4), 275–287, doi:10.1111/j.0435-3676.2002.00182.x, 2002.
- Suess, H.E., Wänke, H.: Radiocarbon content and terrestrial age of twelve stony meteorites and one iron meteorite, *Geochim. Cosmochim. Acta*, 26, 475–480, 1962.
- Sugden, D. E., Hein, A. S., Woodward, J., Marrero, S. M., Rodes, A., Dunning, S. A., Stuart, F. M., Freeman, S. P. H. T., Winter, K. and Westoby, M. J.: The million-year evolution of the glacial trimline in the southernmost Ellsworth Mountains, Antarctica, *Earth Planet. Sci. Lett.*, 469, 42–52, doi:10.1016/j.epsl.2017.04.006, 2017.
- Tikhomirov, D., Olsen, J., Grosen, C. and Egholm, D.: Announcement of in-situ <sup>14</sup>C extraction system of Aarhus University, in Third Nordic Workshop on cosmogenic nuclide techniques., 2016.
- Whitehouse, P. L., Bentley, M. J. and Le Brocq, A. M.: A deglacial model for Antarctica: Geological constraints and glaciological modelling as a basis for a new model of Antarctic glacial isostatic adjustment, *Quat. Sci. Rev.*, 32, 1–24, doi:10.1016/j.quascirev.2011.11.016, 2012.
- Whitehouse, P. L., Bentley, M. J., Vieli, A., Jamieson, S. S. R., Hein, A. S. and Sugden, D. E.: Controls on Last Glacial Maximum ice extent in the Weddell Sea embayment, Antarctica, *J. Geophys. Res. Earth Surf.*, 122(1), 371–397, doi:10.1002/2016JF004121, 2017.

## **Chapter 2. New Last Glacial Maximum Ice Thickness constraints for the Weddell Sea Embayment, Antarctica**

Keir A. Nichols<sup>1</sup>, Brent M. Goehring<sup>1</sup>, Greg Balco<sup>2</sup>, Joanne S. Johnson<sup>3</sup>, Andrew S. Hein<sup>4</sup>, Claire Todd<sup>5</sup>

<sup>1</sup>. Department of Earth and Environmental Sciences, Tulane University, New Orleans, 70118, LA, USA.

<sup>2</sup>. Berkeley Geochronology Center, 2455 Ridge Road, Berkeley, 94709, CA, USA.

<sup>3</sup>. British Antarctic Survey, Natural Environment Research Council, High Cross, Madingley Road, Cambridge, CB3 0ET, UK.

<sup>4</sup>. School of GeoSciences, University of Edinburgh, Drummund Street, Edinburgh, EH8 9XP, UK.

<sup>5</sup>. Department of Geosciences, Pacific Lutheran University, Tacoma, 98447, WA, USA.

Published in *The Cryosphere*

<https://doi.org/10.5194/tc-13-2935-2019>

## **Abstract.**

We describe new Last Glacial Maximum (LGM) ice thickness constraints for three locations spanning the Weddell Sea Embayment (WSE) of Antarctica. Samples collected from the Shackleton Range, Pensacola Mountains, and the Lassiter Coast constrain the LGM thickness of the Slessor Glacier, Foundation Ice Stream, and grounded ice proximal to the modern Ronne Ice Shelf edge on the Antarctic Peninsula, respectively. Previous attempts to reconstruct LGM-to-present ice thickness changes around the WSE used measurements of long-lived cosmogenic nuclides, primarily  $^{10}\text{Be}$ . An absence of post-LGM apparent exposure ages at many sites led to LGM thickness reconstructions that were spatially highly variable, and inconsistent with flowline modelling. Estimates for the contribution of the ice sheet occupying the WSE at the LGM to global sea level since deglaciation vary by an order of magnitude, from 1.4 to 14.1 m of sea level equivalent. Here we use a short-lived cosmogenic nuclide, in situ produced  $^{14}\text{C}$ , which is less susceptible to inheritance problems than  $^{10}\text{Be}$  and other long-lived nuclides. We use in situ  $^{14}\text{C}$  to evaluate the possibility that sites with no post-LGM exposure ages are biased by cosmogenic nuclide inheritance due to surface preservation by cold-based ice and nondeposition of LGM-aged drift. Our measurements show that the Slessor Glacier was between 310 and up to 655 m thicker than present at the LGM. The Foundation Ice Stream was at least 800 m thicker, and ice on the Lassiter Coast was at least 385 m thicker than present at the LGM. With evidence for LGM thickening at all of our study sites, our in situ  $^{14}\text{C}$  measurements indicate that the long-lived nuclide measurements of previous studies were influenced by cosmogenic nuclide inheritance. Our inferred LGM configuration, which is primarily based on minimum ice thickness constraints and thus does not constrain an upper limit, indicates a relatively modest contribution to sea level rise since the LGM of <4.6 m, and possibly as little as <1.5 m.

## **1. Introduction**

We describe new constraints on Last Glacial Maximum (LGM, ca. 26 to 15 ka; Peltier and Fairbanks, 2006) ice thickness changes from three locations within the Weddell Sea Embayment (WSE) of Antarctica (Fig. 1.1). The WSE drains approximately one fifth of the total area of the Antarctic ice sheets (AIS) (Joughin et al., 2006) and is thus an important contributor to LGM-to-present and,

potentially, future sea level change. Previous attempts to reconstruct LGM-to-present ice thickness changes around the WSE used measurements of long-lived cosmogenic nuclides, primarily  $^{10}\text{Be}$  (half-life  $1.387 \pm 0.012$  Ma; Chmeleff et al., 2010; Korschinek et al., 2010) and  $^{26}\text{Al}$  (half-life  $705 \pm 17$  ka; Norris et al., 1983), sourced from bedrock and erratic cobbles proximal to modern glacier surfaces. Through measuring the cosmogenic nuclide concentration of samples of glacial deposits and bedrock, one can constrain the magnitude and timing of past changes in the thickness of adjacent ice masses. However, an absence of post-LGM apparent exposure ages at many sites around the WSE led to LGM thickness reconstructions that were spatially highly variable, and inconsistent with flowline modelling (e.g. Whitehouse et al., 2017). Consequently, estimates based on ice models constrained by field evidence (Le Brocq et al., 2011) and by relative sea level records and earth viscosity models (Bassett et al., 2007) for the contribution of the sector to global sea level since deglaciation began vary by an order of magnitude, from 1.4 to 14.1 m, respectively. The lack of geological evidence for LGM thickening is also manifest in a misfit between present day geodetic uplift rate measurements in southern Palmer Land and predicted uplift rates from a glacial isostatic adjustment (GIA) model (Wolstencroft et al., 2015). Constraining the previous vertical extent of ice provides inputs to numerical models investigating both the response of the ice sheet to past and potential future changes in climate and sea level (e.g. Briggs et al., 2014; Pollard et al., 2016, 2017; Whitehouse et al., 2017), as well as the response of the solid earth to past ice load changes to quantify present day ice-mass loss (e.g. Wolstencroft et al., 2015). Furthermore, quantifying the LGM dimensions of the WSE sector of the AIS is required to further constrain the offset between estimates for post-LGM sea level rise and estimates of the total amount of ice melted since the LGM. The former is sourced from sea level index points, and the latter is sourced from our knowledge of the dimensions of ice masses at the LGM (Simms et al., 2019). Currently, the “missing ice” accounts for between  $15.6 \pm 9.6$  m and  $18.1 \pm 9.6$  m of global sea level rise since the LGM (Simms et al., 2019).

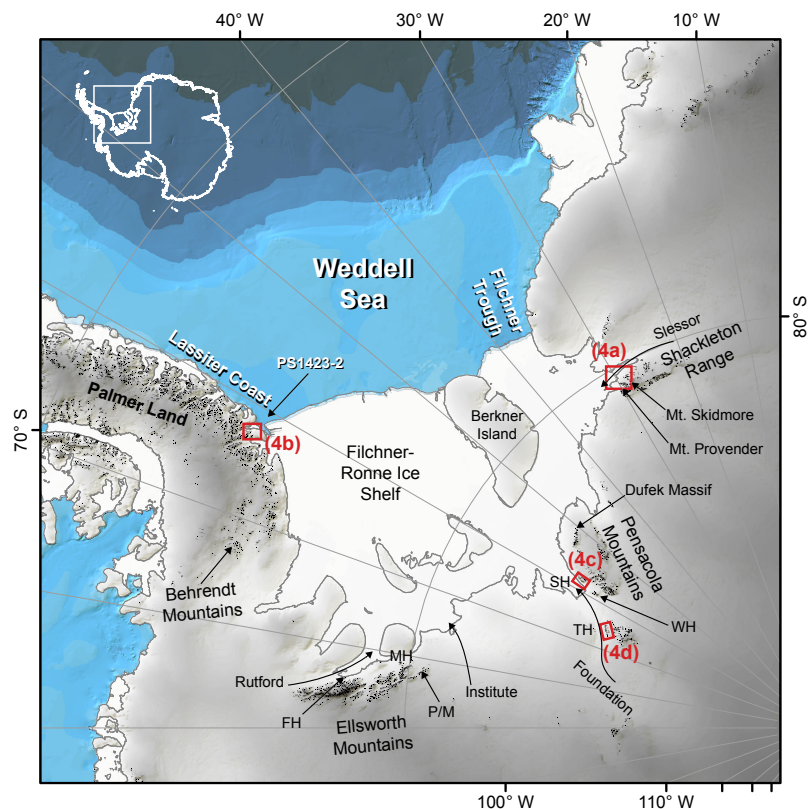


**Figure 2.1:** The Weddell Sea Embayment, including all locations referred to within the text. SH, WH and TH are the Schmidt, Williams and Thomas Hills, respectively. FH, P/M and MH are the Flower Hills, Patriot and Marble Hills, and the Meyer Hills, respectively. Black is exposed rock. Red boxes show extent of satellite images in Fig. 2.4. Exposed rock and coastline sourced from the SCAR Antarctic Digital Database. Bathymetry sourced from the International Bathymetric Chart of the Southern Ocean V1.0 (IBSCO; Arndt et al., 2013). Surface topography (shading) is sourced from the Reference Elevation Model of Antarctica (REMA; Howat et al., 2019). PS1423-2 is a marine sediment core from Crawford et al. (1996).

Although the use of cosmogenic nuclide geochronology to study the AIS is clearly proven (e.g. Stone et al., 2003; Ackert et al., 2007), applications in the WSE are challenging. Many studies, despite making multiple cosmogenic nuclide measurements from relatively large numbers of samples, observed no or few post-LGM exposure ages (Hein et al., 2011, 2014; Balco et al., 2016; Bentley et al., 2017). With no evidence for LGM ice cover, it was not clear whether sites were covered by ice at the LGM, or whether sites were covered but the ice left no fresh deposits on top of those yielding pre-LGM ages. It is therefore currently unknown whether ice was thicker than present during the LGM at the Schmidt Hills in the Pensacola Mountains, and in the Shackleton Range (Figs. 2.1 and 2.2). Results from the Schmidt Hills (Fig. 2.2) indicating no LGM thickening of the Foundation Ice Stream (FIS) are particularly problematic, as thickening of 500 m from the Williams Hills, 50 km upstream of the Schmidt Hills, produces a LGM surface slope that is steeper than glaciological models permit and is also steeper than



present-day ice surface slopes (Balco et al., 2016). Cold-based ice and an associated lack of subglacial erosion is the likely cause of the complex  $^{10}\text{Be}$  data sets, evidenced by numerous studies in the WSE that report  $^{10}\text{Be}$  and  $^{26}\text{Al}$  ratios significantly below those predicted for continuous exposure which is indicative of significant periods of non-erosive burial (e.g. Bentley et al., 2006; Sugden et al., 2017). Cold-based ice preserves surfaces (e.g. Stroeven et al., 2002; Sugden et al., 2005; Gjermundsen et al., 2015), allowing nuclide concentrations to persist within surfaces from previous periods of exposure to the present, a phenomenon known as inheritance. Long-lived nuclides are particularly susceptible to inheritance due to their long half-lives which, when protected from erosion beneath cold-based ice, require long periods of burial to reduce concentrations to below measurable levels. When covered by cold-based ice during glaciations, concentrations of long-lived nuclides record exposure during multiple separate ice free periods rather than just the most recent one. Inheritance thus hinders interpretations of cosmogenic nuclide measurements.

We resolve conflicting LGM thickening estimates based on  $^{10}\text{Be}$  measurements by using measurements of in situ produced  $^{14}\text{C}$ , a cosmogenic nuclide that is, owing to a short half-life of 5730 years, largely insensitive to inheritance. We present the in situ  $^{14}\text{C}$  analysis of transects of erratic and bedrock samples from the Shackleton Range, Lassiter Coast and Pensacola Mountains (Fig. 2.1). Our results constrain the LGM thickness of the Slessor Glacier to between 310 and up to 655 m. We show that ice was at least 385 m thicker than present during the LGM at the Lassiter Coast, proximal to the modern Ronne Ice Shelf edge. Our data also constrain the LGM thickness of the FIS to at least 800 m at the Schmidt Hills. Replicate measurements made from four samples revealed higher than expected variability of in situ  $^{14}\text{C}$  measurements, which is discussed in Sect. 4.1. Our thickness estimates are comparable to those of Hein et al. (2016) in the Ellsworth Mountains, as well as those of Balco et al. (2016) and Bentley et al. (2017) in the Williams and Thomas Hills. Although our results show that locations around the WSE were buried by hundreds of metres of ice, this is less than called for by some reconstructions. Our inferred LGM configuration, which is primarily based on minimum ice thickness constraints and thus does not constrain an upper limit, indicates a relatively modest contribution to sea level rise since the LGM of <4.6 m, and possibly as little as <1.5 m.

### **1.1 The Last Glacial Maximum in the Weddell Sea Embayment**

Although it is clear that grounded ice in the WSE has been thicker in the past (Bentley and Anderson, 1998), there is little evidence as to the thickness and grounding line position of the ice sheet

at the LGM, with contrasting evidence from marine sources, and those inferred from terrestrial studies (Hillenbrand et al., 2014). Terrestrial evidence for the extent of ice in the WSE during the LGM takes the form of numerous cosmogenic nuclide studies. Bentley et al. (2006) measured the  $^{10}\text{Be}$  and  $^{26}\text{Al}$  content of erratics on the southern Antarctic Peninsula. Studies report cosmogenic nuclide concentrations from the Meyer Hills, Patriot Hills, Marble Hills, and the Flower Hills, all in the Ellsworth Mountains (Bentley et al., 2010; Fogwill et al., 2014; Hein et al., 2016; Sugden et al., 2017), the Pensacola Mountains (Hodgson et al., 2012; Balco et al., 2016; Bentley et al., 2017), and the Shackleton Range (Fogwill et al., 2004; Hein et al., 2011, 2014). Figure 2.2 summarises the ice thickness estimates from these studies. The majority of estimates are sourced from  $^{10}\text{Be}$  measurements, with some accompanying  $^{26}\text{Al}$  measurements. Two exceptions are Fogwill et al. (2014) and Balco et al. (2016), whom combined some in situ  $^{14}\text{C}$  measurements with  $^{10}\text{Be}$  measurements to constrain the thickness of the Rutford and Institute ice streams and the Foundation Ice Stream, respectively. The highest elevation post-LGM exposure ages at each site delineate the minimum vertical extent of ice at the LGM. Ice thickness estimates vary spatially around the embayment, ranging from zero to hundreds of metres of LGM thickening.

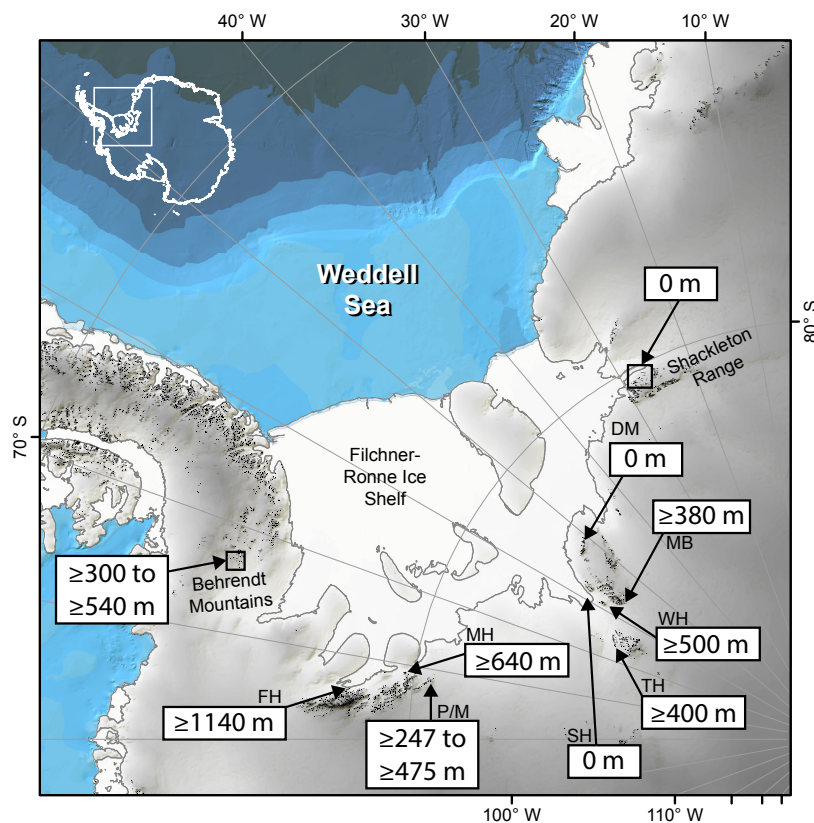


**Figure 2.2:** Current terrestrial ice thickness constraints inferred from measurements of long-lived nuclides around the WSE. Acronyms are as in Fig. 2.1. Constraints for the SH, WH, and TH are sourced from Balco et al. (2016) and Bentley et al. (2017). MB is Mount Bragg (Bentley et al., 2017). Thickness estimate for the Dufek Massif (DM) is sourced from Hodgson et al. (2012). Constraints for the P/M are sourced from Hein et al. (2016). For the MH and FH, the LGM thickness constraints are sourced from Fogwill et al. (2014). The thickness constraints sourced from Fogwill et al. (2014) were interpreted using modern ice surface elevations for the Rutford Ice Stream and Union Glacier measured using the Reference Elevation Model of Antarctica (REMA; Howat et al., 2019). Thickness constraints for the Shackleton Range are sourced from Hein et al. (2011, 2014). The range of LGM thicknesses for the Behrendt Mountains are sourced from multiple locations (Bentley et al., 2006).

Marine geological and geophysical evidence in the southern Weddell Sea indicates a significantly expanded WSE LGM configuration, with subglacial till, subglacial bedforms and a grounding zone wedge found towards the shelf edge (Hillenbrand et al., 2012, 2014; Larter et al., 2012; Arndt et al., 2017). As a result, there is currently a disconnect between marine evidence for a greatly expanded WSE sector and terrestrial evidence indicating little to no vertical change at the LGM in some areas. Hillenbrand et al. (2014) propose two potential LGM configurations of the WSE sector of the AIS. The first scenario, based on terrestrial evidence for vertical LGM ice thicknesses, involves a complex configuration with the grounding line of the ice sheet situated towards the shelf edge and a largely ice-free Filchner Trough and western margin of the WSE. The second scenario, based on marine evidence, places the grounding line of the ice sheet at the shelf edge across the width of the WSE. Flowline

modelling of the response of the FIS, which occupied the Filchner Trough at the LGM, to the onset of glacial conditions shows that there are two plausible LGM grounding line positions for the ice stream: one situated at the shelf edge, and another at the northern margin of Berkner Island (Whitehouse et al., 2017).

### **1.2 In situ $^{14}\text{C}$ exposure dating**

Cosmogenic nuclides  $^{10}\text{Be}$  and  $^{26}\text{Al}$  have half-lives that are much longer than glacial-interglacial cycles, so  $^{10}\text{Be}$  and  $^{26}\text{Al}$  concentrations produced in previous interglacials persist to the present if buried by non-erosive, cold-based ice. The short half-life of in situ  $^{14}\text{C}$  means that only short periods of burial are required to significantly reduce concentrations from previous periods of exposure, making in situ  $^{14}\text{C}$  less sensitive to inheritance than longer-lived nuclides. For example, a burial duration beneath non-erosive, cold-based ice of 11 kyr results in ca. 74% of the original in situ  $^{14}\text{C}$  decaying away. Furthermore, continuously exposed, slowly eroding surfaces reach an equilibrium between production and decay of in situ  $^{14}\text{C}$  (“saturation”) after approximately 30 to 35 kyr. A sample that has reached saturation thus requires low erosion and continuous exposure from before the LGM, whilst a sample that yields a concentration below saturation requires ice cover during the last ca. 35 kyr. Surfaces yielding saturation concentrations therefore provide an upper limit on LGM thickening. Figure for two locations within the WSE; 3 shows a hypothetical ice surface elevation change history at a nunatak partially buried by cold-based, non-erosive ice during the LGM, with associated in situ  $^{14}\text{C}$  measurements from samples collected along an elevation transect on the surface of the nunatak. There is a transition from undersaturated to saturated samples, a discontinuity in the  $^{14}\text{C}$  concentrations which constrains the LGM ice thickness. The “true exposure” data points represent in situ  $^{14}\text{C}$  concentrations with resulting exposure ages matching the post-LGM ice-surface lowering history. The “apparent exposure” data points were saturated at the onset of ice cover and include in situ  $^{14}\text{C}$  that persists to the present due to an insufficient amount of time passing for it to decay away. For the five undersaturated samples, which were buried by ice for differing durations, a range of ~2 to ~4 % of the  $^{14}\text{C}$  accumulated prior to burial will persist to the present. In terms of the effect on resulting exposure ages, the sample exposed at 10 ka yields an apparent exposure age of 11.41 ka (~13 % increase), and the sample exposed at 2 ka yields an apparent exposure age of 2.17 ka (~8 % increase). Without knowing the burial duration of the samples or whether or not the samples were indeed saturated upon burial by LGM ice, we do not know the exact quantity of in situ  $^{14}\text{C}$  inherited in the samples. The in situ  $^{14}\text{C}$  exposure ages are therefore maximum deglaciation ages. In the same

hypothetical scenario with the same samples, ca. 98 % and 97 % of the  $^{10}\text{Be}$  and  $^{26}\text{Al}$  accumulated prior to burial will persist to the present, respectively.

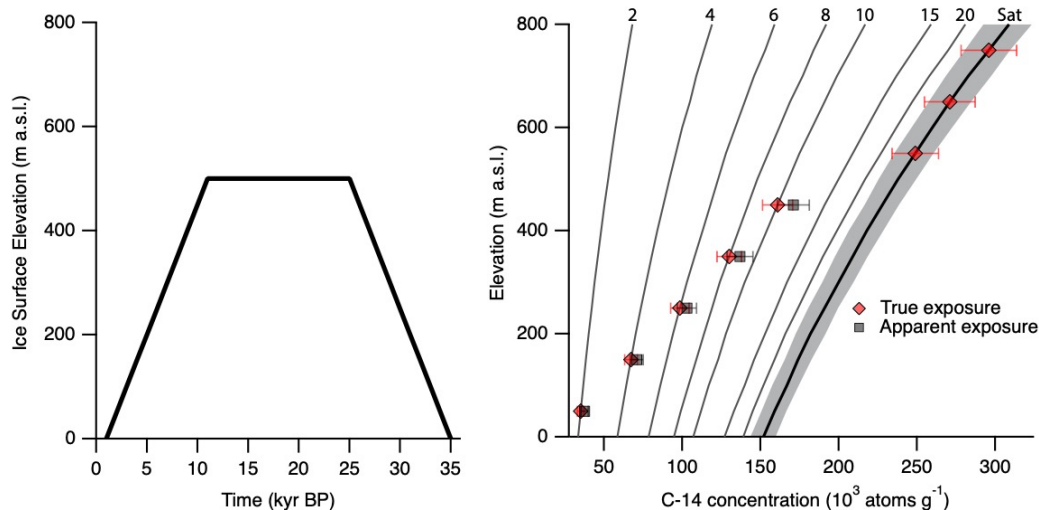


**Figure 2.3:** Left: Hypothetical ice surface elevation change at a nunatak partially covered by ice at the LGM. Right: Resulting in situ  $^{14}\text{C}$  concentration, assuming no surface erosion, in samples collected at 100 m intervals along an elevation transect on the surface of the nunatak. Thin black lines indicate isochrons of exposure duration. Thick black line with dashed lines either side represent the saturation concentration and associated error envelope. Error envelope represents typical analytical uncertainty. “True exposure” refers to the resulting  $^{14}\text{C}$  concentration associated with the ice surface change history on the left plot. “Apparent exposure” is the resulting concentration that includes an inherited component, which is a residual  $^{14}\text{C}$  inventory remaining from the hypothetical samples which were saturated prior to ice cover.

We report in situ  $^{14}\text{C}$  concentrations measured from both erratic and bedrock samples, with primarily erratic samples from the Shackleton Range and the Pensacola Mountains, and solely bedrock from the Lassiter Coast. We assume both materials provide the same information regarding the timing of ice retreat and constraining LGM ice thicknesses. For example, we assume that both erratics and bedrock samples saturated with in situ  $^{14}\text{C}$  indicate that their respective sampling locations were ice free for the last 30 to 35 kyr. With the exception of two samples, all of our erratic samples have previously been measured for their  $^{10}\text{Be}$  content (Hein et al., 2011, 2014, Balco et al., 2016), with the vast majority yielding ages far in excess of the LGM. It is highly likely that these erratic samples have been repeatedly covered and exposed by cold-based ice. Having been covered and uncovered in situ, the erratic samples can thus effectively be considered bedrock. There are, however, potential situations where our assumption that bedrock and erratic samples provide the same information with respect to the timing of changes in ice thickness is not met and resulting  $^{14}\text{C}$  concentrations misrepresent the age of deglaciation,

creating scatter in the measured in situ  $^{14}\text{C}$  data. Erratic samples may, for example, be sourced from mass movement onto glacier surfaces, producing spuriously high  $^{14}\text{C}$  concentrations (See Balco et al., 2019). Spuriously high, in excess of saturation, in situ  $^{14}\text{C}$  concentrations sourced from bedrock samples, however, can only result from analytical errors and thus provides an important test for the premise of the technique. Additionally, erratic cobbles may have undergone downslope movement post-deposition and may have flipped over, or may have been subjected to high erosion rates, which could produce in situ  $^{14}\text{C}$  concentrations with resulting exposure ages lower than the true age of deglaciation. Snow shielding of sample locations is another mechanism leading to exposure ages which underestimate the age of deglaciation and can influence both bedrock and erratic samples. Whilst not without challenges, our in situ  $^{14}\text{C}$  measurements provide an opportunity to unambiguously show whether sites around the WSE were covered by ice at the LGM.

### **1.3 Sample Sites**

#### **1.3.1 Shackleton Range**

The Shackleton Range is located in Coats Land in northeastern WSE, adjacent to Slessor Glacier (Figs. 2.1 and 2.4a). Slessor Glacier drains ice from the East Antarctic Ice Sheet (EAIS) into the Filchner Ice Shelf. Mt. Skidmore is located approximately 25 km upstream of the modern Slessor Glacier grounding line, with the Köppen and Stratton glaciers respectively joining the Slessor Glacier to the north and south of Mt. Skidmore (Fig. 2.4a). Proximal to sampling locations are Ice Tongue A and Ice Tongue B of the Stratton Glacier, and the Snow Drift Glacier (Fig. S2.1). We assume that samples collected from Mt. Skidmore record changes in the thickness of the Slessor Glacier. However, it is possible that samples collected proximal to the smaller ice masses may have been buried by them, rather than by the Slessor Glacier, potentially complicating the interpretation of results. The modern Slessor Glacier surface is situated at ~200 m a.s.l. proximal to Mt. Skidmore, with exposed surfaces of Mt. Skidmore located up to over ~820 m a.s.l. Mt. Provender is located adjacent to the Slessor Glacier grounding line and is bounded by the Stratton and Blaiklock glaciers to the north and south, respectively. Exposed rock of Mt. Provender rises from the modern ice surface up to over ~900 m a.s.l. We analysed 11 samples from the Shackleton Range (Table S2.1), with two from Mt. Provender and nine from Mt. Skidmore (Fig. 4a). At Mt. Provender we analysed one erratic cobble from near the modern ice surface and one bedrock sample from ~650 m above it (Fig. S2.2). Samples from Mt. Skidmore include one bedrock sample and eight

cobbles that form an elevation transect from near the modern ice surface to ~300 m above it (Fig. S2.1). The two highest elevation samples collected from Mt. Skidmore are proximal to the main trunk of the Stratton Glacier more so than the Slessor Glacier, and were collected from ca. 115 and 130 m above the modern Stratton Glacier surface. The two highest elevation samples on Mt. Skidmore therefore may represent a Stratton Glacier ice surface lowering more so than the Slessor Glacier, and thus are presented as a separate sample group to those collected proximal to the Slessor Glacier.

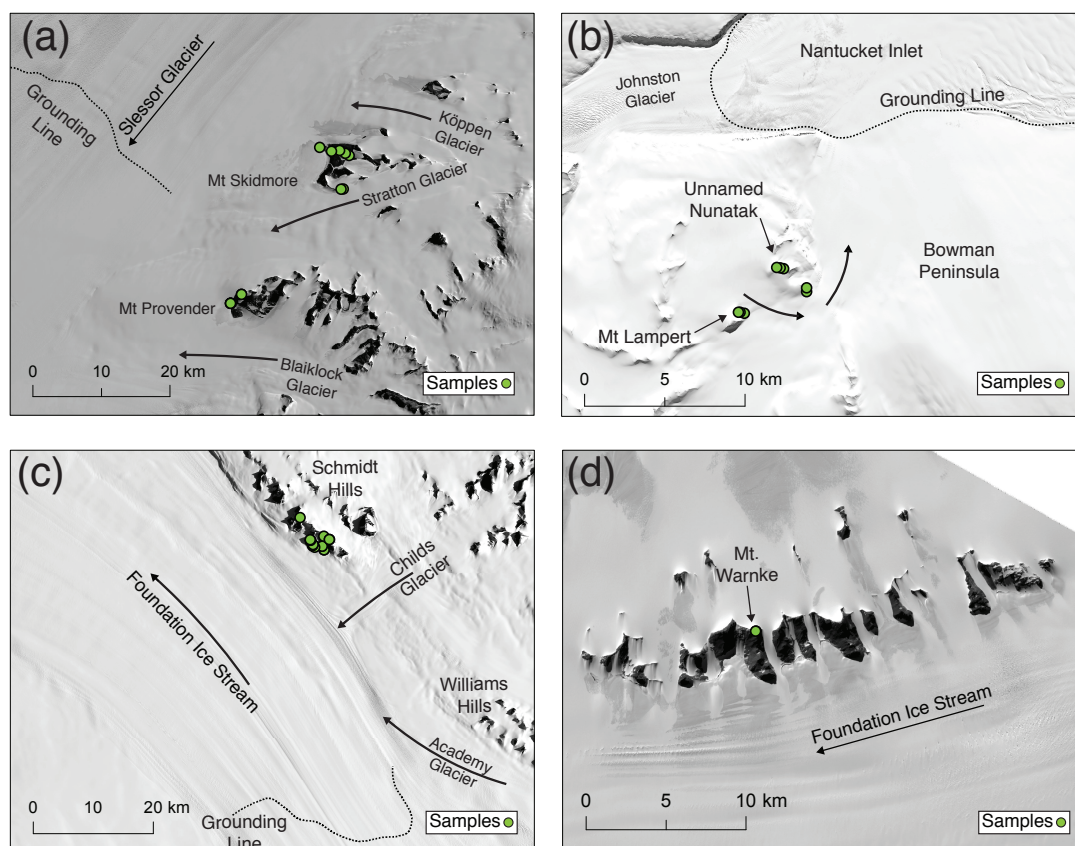


**Figure 2.4:** Landsat imagery of study sites. Location of each image is shown in Fig. 2.1. Green dots show sample locations. Arrows show ice flow directions. A: Mt. Skidmore and Mt. Provender, Shackleton Range. B: Lassiter Coast, southern Palmer Land. C: Schmidt Hills, Pensacola Mountains. D: Thomas Hills, Pensacola Mountains. Landsat 8 imagery courtesy of the U.S. Geological Survey. Grounding line positions sourced from the MEaSURES program V2 (Rignot et al., 2011, 2014, 2016).

### 1.3.2 Lassiter Coast

The Lassiter Coast is located on the east coast of southern Palmer Land, adjacent to the present position of the Ronne Ice Shelf edge (Fig. 2.1). The modern ice surface is situated at 490 m a.s.l. Johnson et al. (2019) collected samples from several sites in this area (Fig. 2.4b) and carried out  $^{10}\text{Be}$  measurements; we subsequently carried out  $^{14}\text{C}$  measurements on these samples as part of the present

study, and the  $^{14}\text{C}$  results are reported both here and in Johnson et al. (2019). Here we discuss results for a total of eight bedrock samples from Mt. Lampert and the Bowman Peninsula collected from 20 to 385 m above the modern ice surface (Figs. 2.4b and S2.3); see Table S2.1 for sample data and Johnson et al. (2019) for  $^{10}\text{Be}$  measurements. The adjacent Johnston Glacier drains ice from central Palmer Land into the WSE (Fig. 2.4b). We interpret the samples together as effectively a single elevation transect that records changes in the thickness of grounded ice in the WSE immediately east of these sites after the LGM.

### **1.3.3 Pensacola Mountains**

The Schmidt Hills are a series of nunataks adjacent to the FIS in the southeast WSE (Figs. 2.1 and 2.4c) proximal to the modern grounding line. The FIS is a major ice stream that drains ice from both the EAIS and West Antarctic Ice Sheet (WAIS) into the WSE. The surface of the FIS adjacent to the Schmidt Hills is situated ca. 200 m a.s.l., with exposed surfaces of the Schmidt Hills reaching up to 1100 m a.s.l. The Thomas Hills are another series of nunataks adjacent to the FIS, located ~130 km upstream of the Schmidt Hills (Figs. 2.1, 2.4d). The main trunk of the FIS adjacent to the Thomas Hills is near 550 m a.s.l., with the Thomas Hills rising up to 1050 m a.s.l. The local ice margin of the FIS at the Thomas Hills is situated ~75 m below the centre of the FIS. We analysed 17 samples from the Pensacola Mountains (Table S2.1); 15 from the Schmidt Hills and two from the Thomas Hills. We made a further seven repeat measurements from four samples collected from the Schmidt Hills. Samples from the Schmidt Hills were collected from Mount Coulter and No Name Spur (Figs. 2.4c and S2.4) from close to the modern ice surface to approximately 800 m above it. We also analysed two samples from the Thomas Hills which were collected from Mount Warnke ca. 320 m above the FIS ice margin (Figs. 2.4d and S2.5). The highest elevation sample from the Schmidt Hills, collected from ca. 1035 m a.s.l., is the only bedrock sample analysed from the Pensacola Mountains, with the rest being erratic cobbles.

## **2. Methods**

We used between 0.5 and 10 g of quartz from each sample for in situ  $^{14}\text{C}$  analysis. The methodology used for the isolation of quartz varies for samples from different sample sites because quartz was previously isolated for prior cosmogenic nuclide studies (see Hein et al., 2011; Balco et al., 2016). For samples processed at the Tulane University Cosmogenic Nuclide Laboratory (primarily those



from the Lassiter Coast), quartz was isolated through crushing, sieving, magnetic separation and froth flotation (modified from Herber, 1969) of sample material. Samples were then etched for at least two periods of 24 hours on both a shaker table in 5 % HF/HNO<sub>3</sub> and then in an ultrasonic bath in 1 % HF/HNO<sub>3</sub>. This leaching procedure removes the organic compound laurylamine used in the froth flotation procedure (Nichols and Goehring, 2019) that could otherwise potentially contaminate our samples with modern carbon.

Carbon was extracted using the Tulane University Carbon Extraction and Graphitization System (TU-CEGS), following the method of Goehring et al. (2019). Quartz is step-heated in a lithium metaborate (LiBO<sub>2</sub>) flux and a high-purity O<sub>2</sub> atmosphere, first at 500 °C for 30 minutes, then at 1100 °C for three hours. Released carbon species are oxidised to form CO<sub>2</sub> via secondary hot-quartz-bed oxidation, followed by cryogenic collection and purification. Sample yields are measured manometrically, and samples are diluted with <sup>14</sup>C-free CO<sub>2</sub>. A small aliquot of CO<sub>2</sub> is collected for δ<sup>13</sup>C analysis, and the remaining CO<sub>2</sub> is graphitised using H<sub>2</sub> reduction over an Fe catalyst. We measured <sup>14</sup>C/<sup>13</sup>C isotope ratios at either Lawrence Livermore National Laboratory Center for Accelerator Mass Spectrometry (LLNL-CAMS) or Woods Hole National Ocean Sciences Accelerator Mass Spectrometry (NOSAMS) (Table S2.2). Stable carbon isotope ratios were measured at the UC-Davis Stable Isotope Facility.

Apparent exposure ages were calculated using v. 3 of the online calculators formerly known as the CRONUS-Earth online calculators (Balco et al., 2008). The online calculators use the production rate scaling method for neutrons, protons and muons of Lifton et al. (2014) (also known as LSDn). We use repeat measurements of the in situ <sup>14</sup>C concentration of the CRONUS-A interlaboratory comparison standard (Jull et al., 2015; Goehring et al., 2019) to calibrate the <sup>14</sup>C production rate. We assume CRONUS-A is saturated with respect to in situ <sup>14</sup>C, given that, based on geological mapping and an ash chronology, the sampling location has remained ice-free since >11.3 Ma (Marchant et al., 1993). All reported in situ <sup>14</sup>C measurements from CRONUS-A, made at multiple laboratories, yield concentrations equivalent to saturation based on other calibration data from elsewhere in the world (e.g. Jull et al., 2015; Fülöp et al., 2019; Goehring et al., 2019; Lamp et al., 2019). We use the CRONUS-A measurements to calibrate the <sup>14</sup>C production rate to reduce scaling extrapolations. Repeat measurements of both CRONUS-A and other samples using the TU-CEGS show that the reproducibility of in situ <sup>14</sup>C measurements is approximately 6 %. We therefore use a 6 % uncertainty for our measured in situ <sup>14</sup>C

concentrations when calculating exposure ages, as this exceeds the reported analytical uncertainty for all of our in situ  $^{14}\text{C}$  measurements. Ages are included in Table S2.2 for completeness but are primarily discussed in the text as either finite or infinite ages. Infinite ages are those for which the measured concentration is above the uncertainty of the saturation concentration for the elevation of a given sample.

We made seven replicate measurements from four samples from the Schmidt Hills that initially yielded saturation or near-saturation in situ  $^{14}\text{C}$  concentrations. We made the first four replicate measurements using the same samples to test the validity of the saturation or near-saturation initial measurements. The second set of measurements produced in situ  $^{14}\text{C}$  concentrations below saturation. Given the difference between the initial measurements and the replicates, we made a further three measurements from three of the same four samples.

### **3. Results**

The vast majority of the  $^{10}\text{Be}$  ages reported by Hein et al. (2011, 2014) in the Shackleton Range exceed 100 ka, whilst we find finite  $^{14}\text{C}$  ages at both Mt. Skidmore and Mt. Provender (Figs. 2.5 and S2.6). At Mt. Skidmore, finite ages are evident across the entire Mt. Skidmore transect, including those sampled proximal to the Stratton Glacier (Fig. 2.5). Samples were collected from multiple ridges of Mt. Skidmore and thus would not necessarily be expected to form a single age-elevation line. The uppermost sample proximal to the Slessor Glacier, collected ~310 m above the modern ice surface, provides a lower limit for the LGM ice thickness of the ice mass. The two samples proximal to the Stratton Glacier, an erratic and bedrock sample with ~17 m a.s.l. between them, are indistinguishable from one another within uncertainties and constrain the LGM thickness to at least 130 m thicker than present. At Mt. Provender, one sample collected proximal to the local Slessor Glacier margin yields a finite age. A second sample from ~890 m a.s.l. (~655 m above the modern ice surface) yields an infinite age, placing an upper limit on the LGM thickness at ~655 m larger than present. We note that the upper limit of 655 m is based on a single in situ  $^{14}\text{C}$  measurement and discuss this limitation further in Sect. 4.2. If quartz was available for additional samples previously collected from Mt. Provender (Hein et al, 2011, 2014), then further measurements could have been made to validate this measurement. The quartz was, however, exhausted in the process of measuring long-lived nuclides. One sample from Mt. Skidmore, collected from ~284 m a.s.l., yields an infinite age. Above the saturated sample we observe seven finite-aged samples which

require significant periods of burial beneath ice to account for their in situ  $^{14}\text{C}$  concentrations. It is glaciologically impossible to have the sample at  $\sim 284$  m a.s.l. exposed for ca. 35 kyr whilst those above it were covered presumably by the Slessor and Stratton glaciers. The infinite age of the sample could be due to scatter within the  $^{14}\text{C}$  measurements, and the fact that the sample is an erratic does allow the possibility of an unlikely geomorphic scenario. As described in Sect. 1.2, erratic samples may be sourced from mass movement onto glacier surfaces, producing spuriously high  $^{14}\text{C}$  concentrations (Balco et al., 2019).

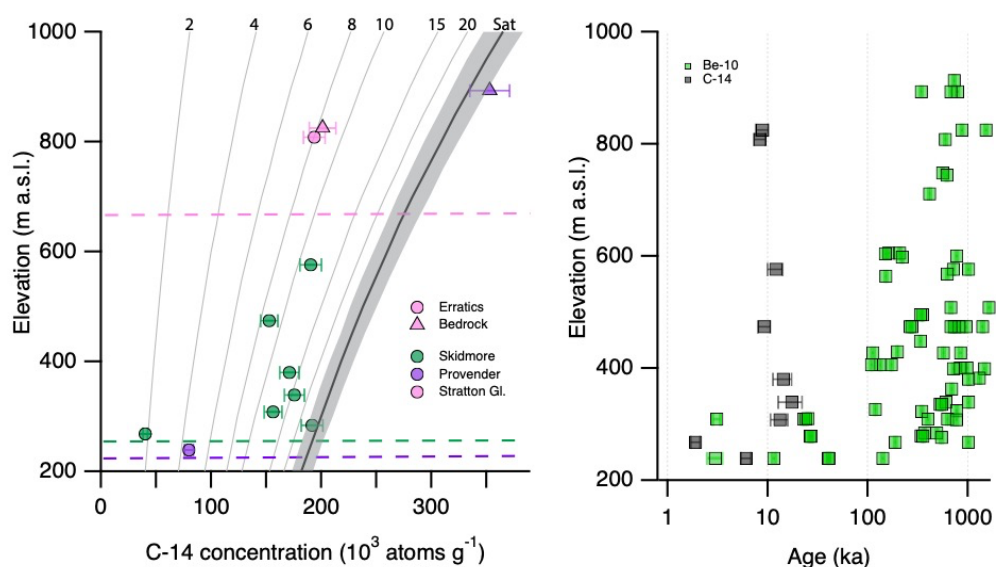


**Figure 2.5:** Left: Elevation versus in situ  $^{14}\text{C}$  concentration of samples from the Shackleton Range. Circles are erratic cobbles, triangles are bedrock. Some error bars are smaller than their respective data points. Horizontal dashed lines show the approximate elevation of the modern ice surface at each site. Light grey lines indicate isochrons of exposure duration. Thick black line and grey shading are the saturation concentration and associated error envelope. Right: Exposure ages from this study (in situ  $^{14}\text{C}$ ) and  $^{10}\text{Be}$  ages of Hein et al. (2011, 2014). Samples yielding infinite in situ  $^{14}\text{C}$  ages are not presented on the right-hand plot.

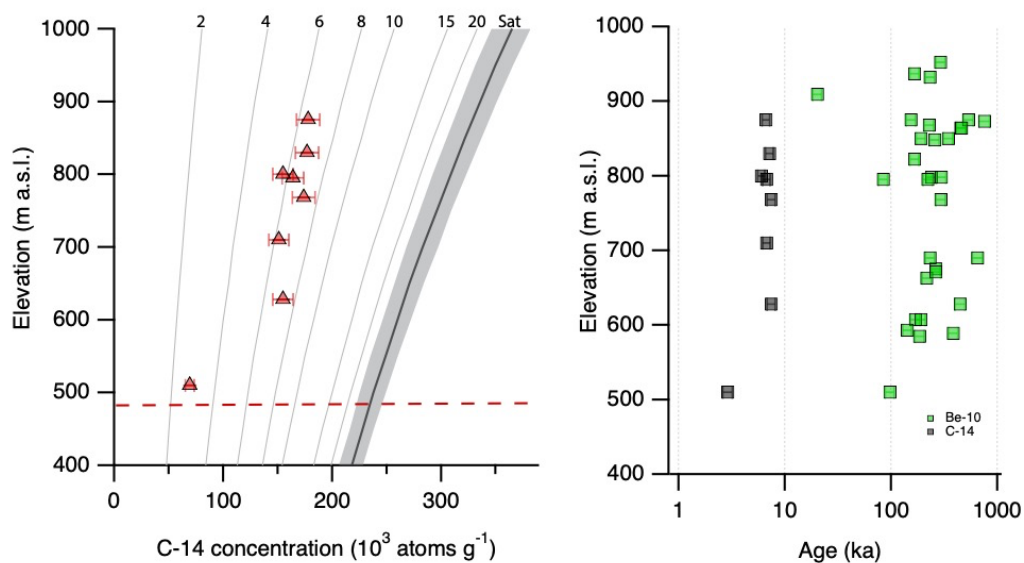


**Figure 2.6:** Left: Elevation versus in situ  $^{14}\text{C}$  concentration of samples collected from the Lassiter Coast. All samples are bedrock. Right: In situ  $^{14}\text{C}$  exposure ages with  $^{10}\text{Be}$  ages of Johnson et al. (2019).

On the Lassiter Coast, Johnson et al. (2019) report  $^{10}\text{Be}$  ages which, with the exception of three measurements, all exceed  $\sim 100$  ka, whilst all of the in situ  $^{14}\text{C}$  ages are finite and fall within the Holocene (Figs. 2.6 and S2.7). The associated in situ  $^{14}\text{C}$  concentrations are similar over the range of sample elevations (Fig. 2.6). The uppermost sample, collected  $\sim 385$  m above the modern ice surface, provides a lower limit on the thickness of LGM ice at the Lassiter Coast. The small range of ages across ca. 300 m elevation transect indicate that ice thinning occurred rapidly at this study site (Johnson et al., 2019).

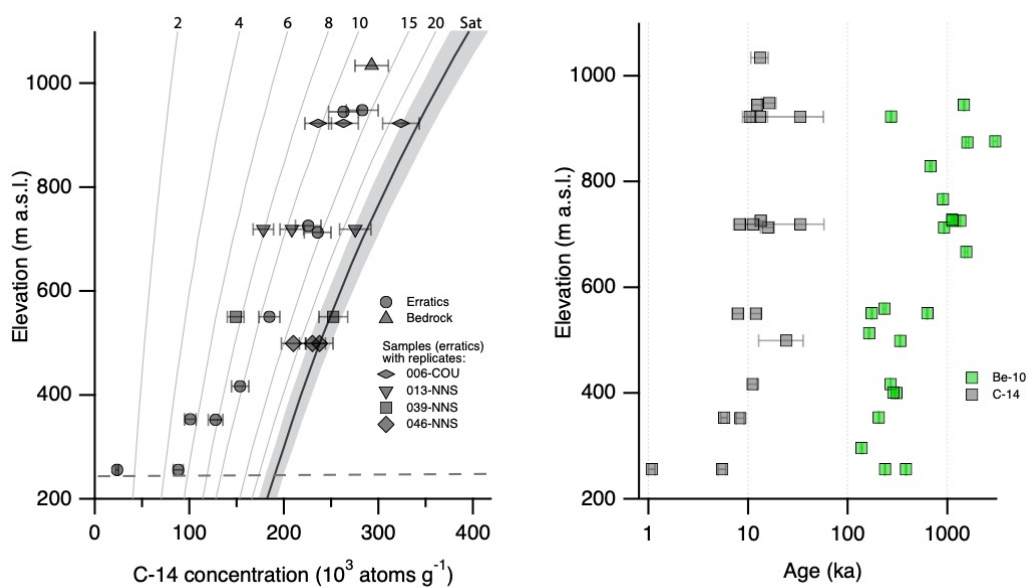


**Figure 2.7:** Left: Elevation versus in situ  $^{14}\text{C}$  concentration of samples collected from the Schmidt Hills. All samples are erratics with the exception of the highest elevation sample, shown with a triangle. Samples with replicate measurements are displayed with differing symbols. Right: Schmidt Hills exposure ages from this study (in situ  $^{14}\text{C}$ ) and those of Balco et al. (2016) and Bentley et al. (2017) ( $^{10}\text{Be}$ ). Measurements yielding infinite in situ  $^{14}\text{C}$  ages are not presented on the right-hand plot.

At the Schmidt Hills,  $^{10}\text{Be}$  ages from Balco et al. (2016) and Bentley et al. (2017) range from  $\sim 140$  ka to 3 Ma (Fig. 2.7). We observe finite ages at low elevations and finite, close to infinite, and infinite ages at higher elevations (Figs. 2.7 and S2.8). Given that higher elevations cannot be covered by ice unless lower elevations were also covered, we remeasured the apparently infinite and near-infinite aged samples ( $\sim 500$  to  $\sim 920$  m a.s.l., or  $\sim 270$  to  $\sim 690$  m above the modern ice surface). The replicate results (Fig. 2.7) show high variability, greater than that observed in previous repeat measurements of CRONUS-A and other samples (Goehring et al., 2019). There is no apparent analytical reason for the initial measurements yielding infinite or near-infinite ages and then yielding differing concentrations with repeat measurements. Samples yielding only finite ages (those that were not measured multiple times) are observed up to  $\sim 420$  m a.s.l., or  $\sim 190$  m above the modern ice surface. In addition, the bedrock sample collected from ca. 1035 m a.s.l. yields a finite age, indicative of a LGM thickness at least  $\sim 800$  m larger than present for the FIS at the Schmidt Hills. The agreement between the bedrock age and the finite measurements from lower elevations means we conclude that, at the Schmidt Hills, the FIS was 800 m thicker than present at the LGM. This conclusion, and the repeat measurements with a high degree of scatter, are discussed in Sect. 4.1 and 4.2.

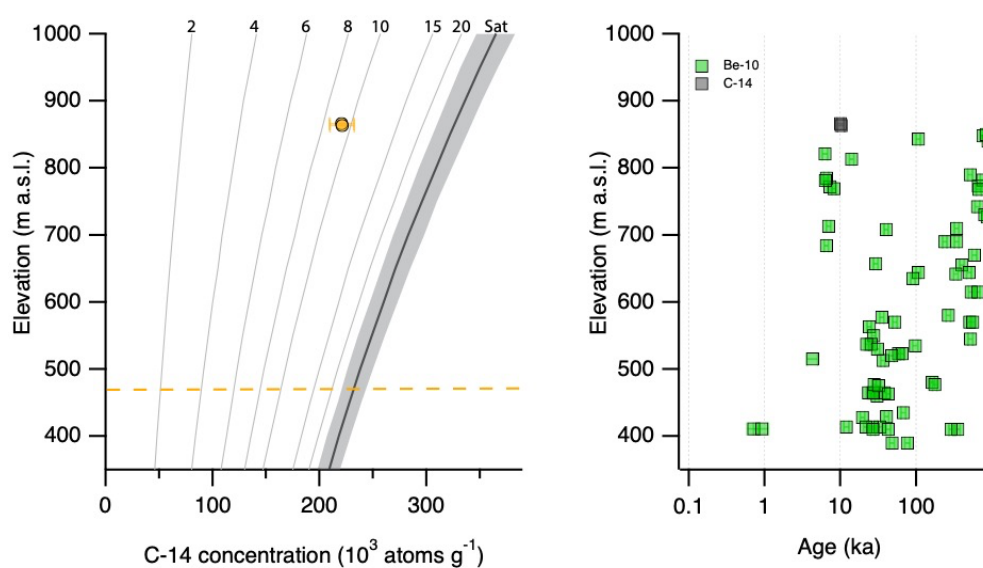


**Figure 2.8:** Left: Elevation versus in situ  $^{14}\text{C}$  concentration of samples collected from the Thomas Hills. All samples are erratics. Note that both plots contain in situ  $^{14}\text{C}$  data for two samples within close

agreement, such that the points overlap. Right: Thomas Hills exposure ages from this study (in situ  $^{14}\text{C}$ ) and those of Balco et al. (2016) and Bentley et al. (2017) ( $^{10}\text{Be}$ ).

The two samples collected from the Thomas Hills yield finite ages within  $\sim 0.2$  ka of one another (Figs. 2.8 and S2.9). Results thus indicate that the FIS was at least  $\sim 320$  m thicker than present at the LGM at the Thomas Hills. The apparent in situ  $^{14}\text{C}$  ages, at  $\sim 10$  ka, are consistent with a cluster of  $^{10}\text{Be}$  ages between 7 and 9 ka in the Thomas Hills reported by Balco et al. (2016) from 225 m above the modern FIS surface, as well as a  $^{10}\text{Be}$  age of 4.2 ka reported by Bentley et al. (2017) collected 125 m above the modern ice surface. Considering the evidence for significant LGM thickening of the FIS from our in situ  $^{14}\text{C}$  results from the Thomas Hills, as well as  $^{10}\text{Be}$  ages of Balco et al. (2016) and Bentley et al. (2017) from both the Williams and Thomas Hills, we infer that it is likely that the FIS reached up to 800 m above its present thickness at the LGM at the Schmidt Hills. We discuss this inference further in the following section.

## **4. Discussion**

### **4.1. Assessment of $^{14}\text{C}$ elevation transects**

The premise of our study is that one can clearly infer if a site was ice-covered at the LGM by determining whether the in situ  $^{14}\text{C}$  concentration of samples from that site are at or below saturation. In this section we assess the success of the approach. To assess the validity of this method, we can, for example, identify where the in situ  $^{14}\text{C}$  data records ice thinning, with saturated samples or the oldest exposure ages at the highest elevations and a trend of decreasing in situ  $^{14}\text{C}$  age toward modern ice surfaces. Consistency between in situ  $^{14}\text{C}$  data and other nuclide concentrations (e.g.  $^{10}\text{Be}$ ) could also help validate the in situ  $^{14}\text{C}$  measurements. We also look at factors beyond the in situ  $^{14}\text{C}$  concentrations, such as the glaciological link between study sites, which may add clarity where the in situ  $^{14}\text{C}$  measurements show a high degree of scatter.

At some sites our results are consistent with the premise, as well as internally consistent. At the Lassiter Coast, ages decrease toward the present ice sheet surface. Though limited by the number of samples, two measurements from Mt. Provender align with the premise of our study, in that we find a finite age located at a low elevation with an infinite age above it. In the Thomas Hills we see consistency between the finite  $^{14}\text{C}$  ages and previously published  $^{10}\text{Be}$  ages (Balco et al., 2016; Bentley et al., 2017). Fogwill et al. (2014) also observe consistency between  $^{14}\text{C}$  and  $^{10}\text{Be}$  ages, which constrain the LGM

thickness and dynamics of the Rutford Ice Stream. However, we observe apparently finite ages above apparently infinite ages at the Schmidt Hills, a scenario that is glaciologically impossible if our assumptions are correct that samples are indeed glacial erratics that have either been deposited previously and repeatedly covered by cold-based ice or delivered to their sampling location during the last glaciation and were sourced subglacially. The scatter observed in the repeat measurements (Fig. 2.7) is greater than that of repeat measurements made of CRONUS-A and other samples made in our laboratory (Goehring et al., 2019). Three samples from the Schmidt Hills (006-COU, 008-NNS and 046-NNS, collected from ~920, ~710 and ~500 m a.s.l., respectively) were previously measured for their in situ  $^{14}\text{C}$  content and were published by Balco et al. (2016). All three of the samples previously measured by Balco et al. (2016) yielded higher concentrations (two of which were above saturation with the third at saturation) than their new measurements presented in this study. Furthermore, two of the three samples (006-COU and 046-NNS) were measured multiple times (in this study) and display the high scatter under discussion. Balco et al. (2016) proposed unrecognised measurement error as the cause of the spuriously high in situ  $^{14}\text{C}$  concentrations. Why the replicate measurements from samples from the Schmidt Hills display a high degree of scatter remains to be determined.

The most likely reason for  $^{14}\text{C}$  measurement error is contamination by modern  $^{14}\text{C}$ , which would result in a spuriously high concentration. In contrast, a spuriously low concentration is less likely, and we are not aware of any documented instances of this. In our laboratory we have found that it is relatively easy to contaminate a sample with modern carbon through the use of organic compounds in the froth flotation mineral separation procedure (Nichols and Goehring, 2019). However, froth flotation was not used to isolate the quartz of any of the samples for which replicate measurements were made. On multiple occasions we have observed spuriously high  $^{14}\text{C}$  concentrations, far in excess of saturation concentrations, from quartz separates of fine grain sizes (ca. 60  $\mu\text{m}$ ) that were not isolated using froth flotation. We do not yet know the reason for the fine grain sizes yielding elevated  $^{14}\text{C}$  concentrations, but one hypothesis is that the finite-aged replicate measurements were unintentionally made using quartz separates with a coarser average grain size than the initial infinite measurements. We believe the above observations indicate that the increased scatter may be the result of measurement difficulties, perhaps lithology- or grain size-specific.

Regardless of the cause of the high degree of scatter observed in the replicate measurements, we need to discuss possible explanations for apparently infinite ages at lower elevations than apparently

finite ages to isolate which measurements (infinite vs finite replicates) are the most valid to base interpretations on. At the Schmidt Hills, the hypothesis that infinite ages situated below finite ages are spurious and due to measurement errors is consistent with the glaciological relationship amongst the Schmidt, Thomas and Williams Hills (see Sect. 4.2) and is also consistent with the finite bedrock age sourced from a higher elevation. The bedrock age is a robust constraint because the sample cannot have been subjected to geomorphic scenarios that could cause the resulting age to misrepresent the timing of deglaciation. The hypothesis that the infinite ages are correct produces a steep LGM surface slope and is not consistent with thickness estimates from the Williams and Thomas Hills. We elaborate on this point in Sect. 4.2.

As described in Sect. 1.2, it is theoretically possible for in situ  $^{14}\text{C}$  saturated erratic samples to occur at lower elevations than finite ages in rare situations if the former were transported by LGM ice. Balco et al. (2019) observed an apparently saturated sample beneath finite aged samples. Supported by field observations, Balco et al. (2019) propose that the saturated sample was sourced from a rockfall upstream and transported to the study site as supraglacial debris, explaining the elevated in situ  $^{14}\text{C}$  concentration. Whilst this could explain the low-elevation saturated sample at Mt. Skidmore, as well as infinite measurements situated beneath finite measurements at the Schmidt Hills, it does not explain the poor reproducibility of the Schmidt Hills measurements.

We conclude that the basic concept works, as shown at the Lassiter Coast and the Shackleton Range, as well as in other aforementioned studies. In the following section we discuss the implications for LGM ice sheet reconstructions. However, it is clear that more investigation into laboratory issues and geological and geomorphic factors is required to identify the cause or causes of apparently site- or lithology-specific excess scatter in in situ  $^{14}\text{C}$  measurements.



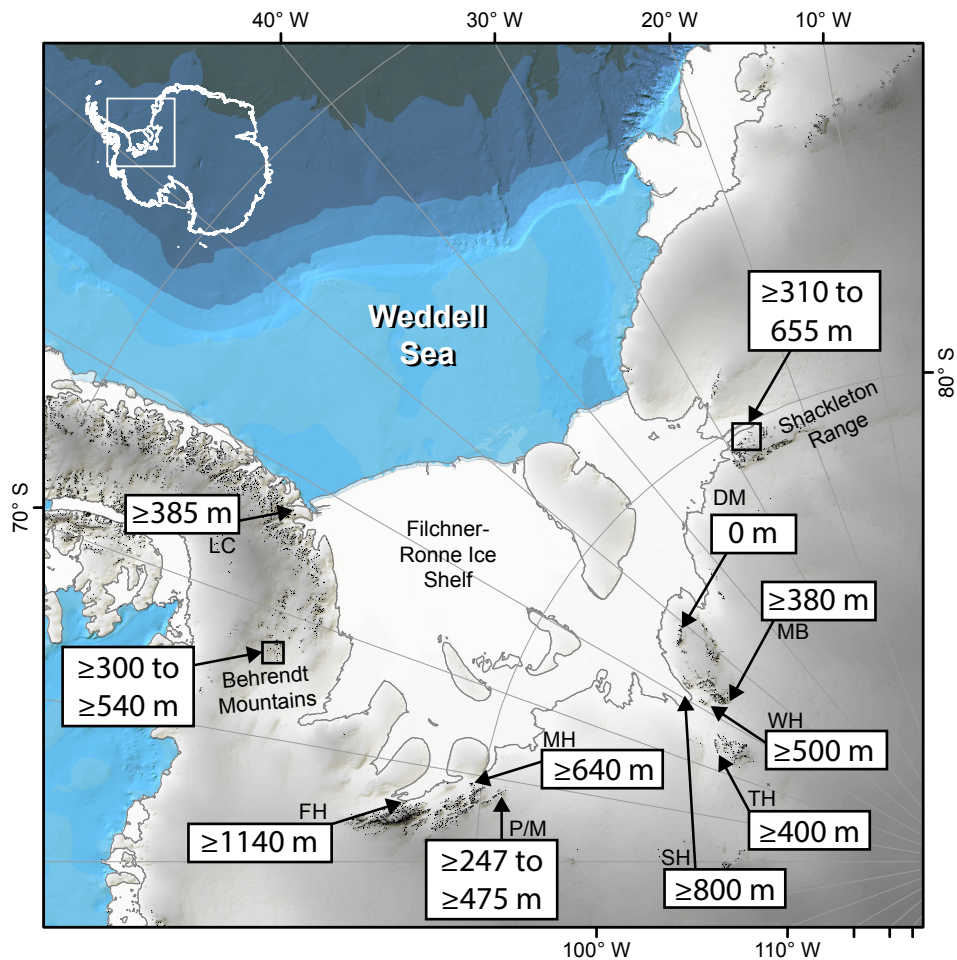


**Figure 2.9:** Terrestrial ice thickness constraints inferred from measurements of cosmogenic nuclides around the WSE. Constraints for the Lassiter Coast (LC), Shackleton Range, and the Schmidt Hills are sourced from this study. All other ice thickness values and locations are the same as in Fig. 2.2.

#### **4.2 LGM ice thicknesses in the Weddell Sea Embayment**

Our LGM thickness estimates are summarised in Fig. 2.9. The new in situ  $^{14}\text{C}$  concentrations indicate that the vast majority, if not the entirety, of Mt. Skidmore, and presumably much of Mt. Provender, were covered by ice at the LGM (Figs. 2.5 and 2.10). The highest elevation samples on Mt. Skidmore proximal to the Slessor Glacier yield infinite ages and indicate that the ice stream was at least 300 m thicker at the LGM than at present. This assumes the samples were not influenced by expansion of local ice masses from the southeast (Fig. S2.1). If so, and assuming the surface gradient of Slessor Glacier during the LGM was similar to today, this would suggest the Slessor Glacier was  $\sim 300$  m thicker at Mt. Provender at the LGM. With no high-elevation infinite ages found on Mt. Skidmore, our thickness estimates for the Slessor Glacier are likely conservative estimates. Finite ages are observed across the entire Mt. Skidmore transect and there is only a single exposed peak (between Ice Tongue A and Ice

Tongue B of the Stratton Glacier, Fig. S2.1) that is at a higher elevation than our sampling locations (ca. 25 m higher). Presumably, given the evidence for the expansion of the Slessor and Stratton glaciers, this small peak was covered by these or local ice masses at the LGM. Our data therefore indicate that, regardless of the source, the Mt. Skidmore site was covered by ice during the LGM, whilst the top of Mt. Provender remained exposed. Whilst the upper limit of LGM ice at Mt. Provender is based on a single sample, we believe this sample is a reliable indicator of LGM ice thickness for the following reasons. The sample is sourced from bedrock and therefore cannot have been subjected to geomorphic scenarios causing the exposure age to misrepresent the timing of ice retreat. Furthermore, froth flotation, which introduces modern carbon to sample material (Nichols and Goehring, 2019), was not used to isolate quartz for this sample. Our thickness constraints (~300-655 m) supersede those of previous exposure dating studies that found no evidence from long-lived isotopes for a thicker Slessor Glacier at the LGM (Hein et al, 2011, 2014). Our LGM thickness constraints for the Slessor Glacier are consistent with our other sites as well as those of previous authors for a significantly thicker FIS at the LGM (Balco et al., 2016; Bentley et al., 2017).

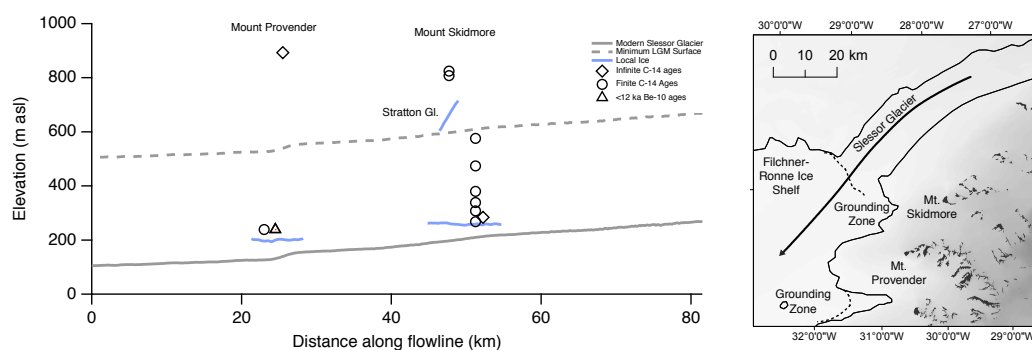


**Figure 2.10:** Exposure-age results projected onto an elevation profile along flowline of the Slessor Glacier. Flowline location is shown in the map (right). Infinite  $^{14}\text{C}$  measurements are offset in regard to their distance along flowline to improve readability. The  $^{10}\text{Be}$  data included are those from Hein et al. (2011, 2014) which yield exposure ages below 12 ka (LSDn scaling, antarctica.ice-d.org). Elevation data for ice surfaces and map shading is sourced from the Reference Elevation Model of Antarctica (REMA; Howat et al., 2018). Grounding line positions sourced from the MEaSUREs program V2 (Rignot et al., 2011, 2014, 2016). Minimum LGM surface is the modern day surface profile with the elevation increased above present using our minimum LGM thickness estimates.

The new in situ  $^{14}\text{C}$  results from the Lassiter Coast show that bedrock surfaces 385 m above the modern ice surface were covered by ice at the LGM. As with results in the Pensacola Mountains, with only a lower limit for the LGM thickness of 360 m, there could have been thicker ice on the Lassiter Coast at the LGM. The in situ  $^{14}\text{C}$  measurements contrast with  $^{10}\text{Be}$  measurements that were likely

influenced by cold-based ice cover, resulting in nuclide inheritance (Johnson et al., 2019). The finite in situ  $^{14}\text{C}$  ages of samples collected from 628 to 875 m a.s.l., with ages between  $6.0 \pm 0.7$  ka and  $7.5 \pm 0.9$  ka, are consistent with a minimum age of grounded ice retreat from a marine sediment core close to the modern ice shelf edge of  $5.3 \pm 0.3$  ka BP (Hedges et al., 1995; Crawford et al., 1996; Fig. 2.1). The fact that significant thinning occurred in the Holocene may help explain the misfit between GIA models and GPS measurements in Palmer Land (Wolstencroft et al., 2015). A thicker ice load at the LGM than that used by current ice models, or present ice load estimates that persist into the Holocene, are two potential solutions postulated by Wolstencroft et al. (2015) to explain the misfit. Further work is needed to take our new ice history into account and to investigate if a minimum of 385 m of ice at the LGM and subsequent rapid thinning at  $\sim 7$  ka at the Lassiter Coast can help account for the offset.

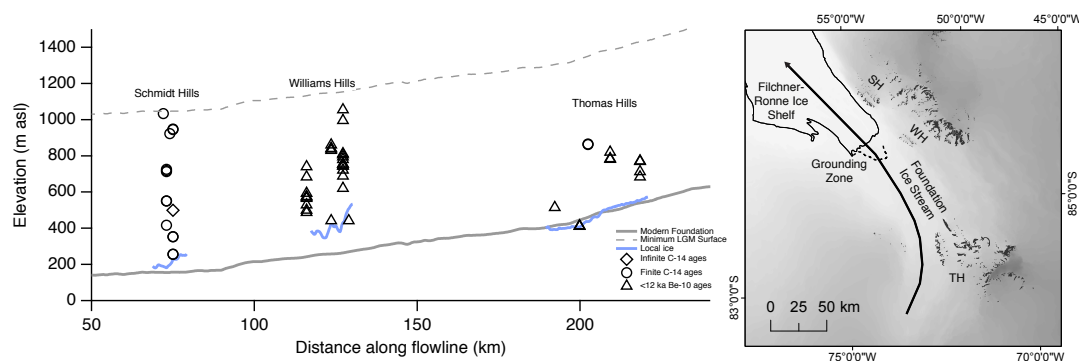


**Figure 2.11:** Exposure-age results projected onto an elevation profile along flowline of the Foundation Ice Stream. Flowline location is shown in the map (right). Infinite  $^{14}\text{C}$  measurements are offset in regard to their distance along flowline to improve readability. The  $^{10}\text{Be}$  data included are those from Balco et al. (2016) and Bentley et al. (2017) which yield exposure ages below 12 ka (LSDn scaling, antarctica.ice-d.org). Elevation data for ice surfaces and map shading is sourced from the Reference Elevation Model of Antarctica (REMA; Howat et al., 2019). Local ice margins are highly simplified. Grounding line positions are sourced from the MEASUREs program V2 (Rignot et al., 2011, 2014, 2016)). Minimum LGM surface is the modern day surface profile with the elevation increased above present using our minimum LGM thickness estimates.

Our in situ  $^{14}\text{C}$  data indicate that the FIS was at least 800 m thicker than present at the Schmidt Hills at the LGM, which contrasts with previous studies which found no evidence for the LGM thickness of the FIS at the Schmidt Hills (Balco et al., 2016; Bentley et al., 2017). We base our LGM thickness estimate on the aforementioned finite-aged repeat measurements and the finite aged bedrock sample, rather than on the poorly reproduced infinite aged-measurements. There is robust evidence for a FIS that was at least 500 m thicker than present at the LGM at the Williams Hills, located only 50 km upstream of the Schmidt Hills (Figs. 2.1 and 2.11; Balco et al., 2016; Bentley et al., 2017). Given the evidence for a significantly thicker FIS proximal to the Schmidt Hills, we argue that the repeat measurements and the

bedrock measurement indicative of the FIS being 800 m thicker are glaciologically most-likely, and thus base our LGM ice thickness estimates on them. Using the infinite measurements and accompanying constraint at the Schmidt Hills for the LGM thickness of 320 m thicker than present produces a steep surface slope from the nearby Williams Hills (Fig. 2.11), though less so than the surface slope produced when no LGM thickening is inferred at the Schmidt Hills based on  $^{10}\text{Be}$  measurements (Balco et al., 2016). The two measurements from the Thomas Hills provide a lower limit for the LGM thickness, but the possibility remains that there was more thickening than the ca. 320 m in situ  $^{14}\text{C}$  constraint. Fig. 2.11 tentatively indicates that the FIS may have been ~900 m thicker when using the modern surface profile of the FIS increased in elevation up to the height of the finite ages from the Schmidt Hills and post-12 ka  $^{10}\text{Be}$  ages from Balco et al. (2016) and Bentley et al. (2017) from the Williams Hills. This is a tentative interpretation because, if thickening is sea level controlled, there would be progressively less thinning expected upstream.

Our LGM ice thickness constraints are consistent with evidence for significantly thicker ice at the LGM in the Ellsworth Mountains (Hein et al., 2016, Fig. 2.2), and also likely consistent with measurements in Bentley et al. (2006). The post-LGM exposure ages of Hein et al. (2016) constrain LGM thicknesses to between 475, 373 and 247 m larger than present at three study sites in the Ellsworth Mountains. A pulse of up to 410 m of thinning appears similar both in scale and timing to the rapid ice surface lowering of 385 m recorded at the Lassiter Coast. Furthermore, measurements of long-lived nuclides by Bentley et al. (2006) show that there has been at least 300 m of thinning since the LGM in the Behrendt Mountains.

#### **4.3 Grounding line position and flowline modelling comparison**

Whitehouse et al. (2017) use their flowline model to reproduce the modern FIS ice surface profile and investigate the response of the ice stream to the onset of glacial and interglacial conditions. The following results from Whitehouse et al. (2017) are from their experiments in which the FIS is routed to the east of Berkner Island, which it is believed to have done during the LGM based on modelling studies (Le Brocq et al., 2011; Whitehouse et al., 2012) and aforementioned marine geological evidence for the former presence of grounded ice (Sect. 1.1). Under glacial conditions the FIS thickens by ~300 to ~500 m adjacent to the Thomas Hills, ~200 to ~400 m adjacent to the Williams Hills, ~150 to ~350 m adjacent to the Schmidt Hills, and ~100 to ~300 m proximal to the Shackleton Range. The lower value

for each location is sourced from flowline experiments during which the grounding line of the FIS reaches a stable position at the northern margin of Berkner Island, with the higher value sourced from a scenario during which the grounded ice stream stabilises at the shelf edge. Our in situ  $^{14}\text{C}$  LGM thickness constraints at each study location in the Pensacola Mountains and Shackleton Range exceed the upper estimates of the FIS flowline model of Whitehouse et al. (2017) under glacial conditions. The flowline model shows that the FIS, a major contributor to the total WSE ice flux, is able to reach a stable position at the shelf edge when tuned using LGM thickness constraints lower than those presented here. Therefore, our thickness estimates add strength to the hypothesis that grounded ice occupying the WSE during the LGM reached a stable position located at the shelf edge (Bentley and Anderson, 1998; Hillenbrand et al., 2014).

#### **4.4 Sea level contribution**

To estimate the contribution to post-LGM sea level rise of the WSE we use a highly simplified scenario in which a range of minimum LGM thickness change estimates are distributed evenly across the WSE using an area for the sector defined by Hillenbrand et al. (2014). Distributing the lowest of our minimum LGM thickness constraints, 310 m for the Slessor Glacier, over the entire WSE produces a minimum sea level equivalent (SLE) of 2.2 m. When using the highest of our minimum thickness estimates, 800 m for the FIS, the minimum SLE increases to 5.8 m. Using the average minimum LGM thickness constraint for our three study sites (580 m) produces a minimum SLE for the sector of 4.2 m. This scenario lacks any glaciological basis and is unrealistic, with no variation in ice thickness with location and no consideration of ice dynamics, isostasy, or bathymetry. Hence, further work is required to produce a realistic SLE for the WSE using our in situ  $^{14}\text{C}$  thickness constraints.

We compare our in situ  $^{14}\text{C}$  LGM thickness estimates with the predicted LGM thickness change of three published ice sheet models at each of our study sites to evaluate our minimum SLE estimates. We also quantify the WSE-sourced SLE for each model output. By comparing our data with the predicted LGM thickness from the model outputs, we can see which models predict LGM thickness changes in excess of and below our in situ  $^{14}\text{C}$  thickness constraints. We compare our data with the predicted LGM thickness change at each of our sites from the ice sheet modelling of Le Brocq et al. (2011), Whitehouse et al. (2012), and Golledge et al. (2014), which predict a SLE for the WSE of ca. 3.0 m, 1.5 m, and 4.6 m, respectively.

From Fig. 2.12 it is apparent that the model output of Golledge et al. (2014) exceeds the thickness constraints at each of our sites. With a SLE of ca. 4.6 m for the WSE, this places a more robust upper limit on the minimum SLE contribution of the WSE using our data, showing that our upper minimum SLE estimate of 5.8 m is likely an overestimation due to the limitations outlined above. The only site where our minimum LGM ice thickness constraint exceeds any of the predicted LGM thickness changes from the model outputs is at the Lassiter Coast, where a LGM thickness of 385 m larger than present exceeds the model output-based thickness estimate of both Le Brocq et al. (2011) and Whitehouse et al. (2012). The Lassiter Coast data indicate that the lower limit for the SLE for the WSE is between 3.0 m and 4.6 m, whilst evidence from all other sites suggests it was <1.5 m.

Based on the above, we conclude that our minimum LGM thickness constraints indicate that the WSE contributed <4.6 m, and possibly as little as <1.5 m, toward postglacial sea level rise. This is a range of minimum contributions to sea level rise and not a minimum-maximum range, as the values are informed using only minimum thickness constraints. Because this is an estimate for the lower limit of the SLE for the WSE, we cannot rule out a larger contribution.

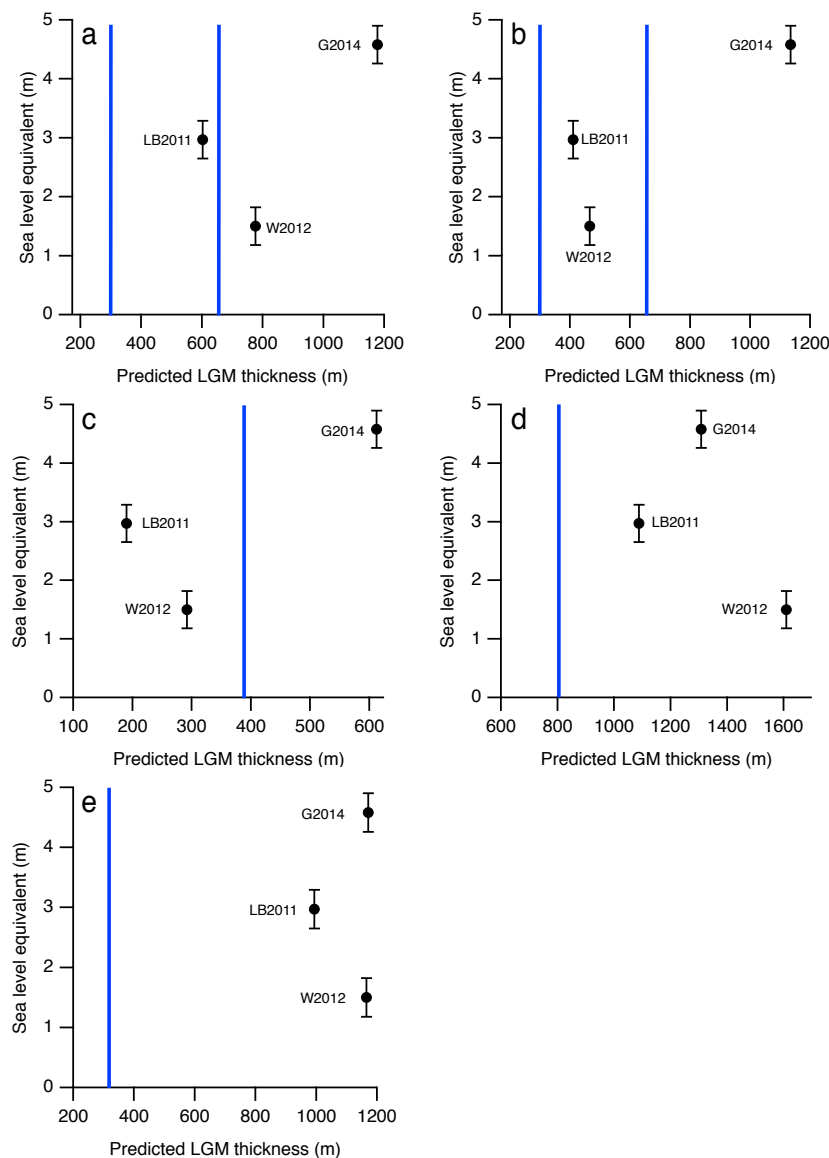


**Figure 2.12:** Predicted LGM ice thickness change from three ice sheet model outputs at each of our study sites and their associated sea level equivalent (SLE) for the Weddell Sea Embayment (WSE) sector of the Antarctic ice sheet. A. is Mt. Skidmore, B. Mt. Provender, C. the Lassiter Coast, D. Schmidt Hills, and E. Thomas Hills. Vertical blue lines show the interpreted LGM thickness change at each site based on our in situ  $^{14}\text{C}$  data. For A. and B., the two vertical blue lines show the range of thickness estimates for the two sites, with the upper limit constrained by the highest elevation saturated sample at Mt. Provender. “G2014” refers to Golledge et al. (2014), “LB2011” refers to Le Brocq et al. (2011), and “W2012” refers to Whitehouse et al. (2012). Errors are not provided for the model outputs. The average error of published SLEs associated with model outputs for the entire ice sheet is 1.45 m (see Simms et al., 2019). We therefore use an error of 0.3 m for the three model SLEs, which is 22% of the average error (22% is the proportion of the AIS that the WSE drains, see Joughin et al. (2006)).

A SLE value of <4.6 m places our estimate between those modelled by Bentley et al. (2010) (1.4 m to 2 m) and Bassett et al. (2007) (13.1 to 14.1 m). Using the estimate based on all sites with the exception of the Lassiter Coast data, the minimum SLE estimate of <1.5 m is consistent with the lower end of published SLEs for the sector. Our exposure ages indicate the Weddell Sea sector contributed to

sea level during the early- to mid-Holocene, though they do not preclude a significant contribution earlier than this. Our estimates imply that the sector provided a modest contribution to global sea level. Whitehouse et al. (2017) estimate the sea level contribution of the FIS to between  $\sim 0.05$  and  $\sim 0.13$  m. Given that our  $^{14}\text{C}$  thickness constraints for the FIS, including those in the Shackleton Range, exceed all of those used by Whitehouse et al. (2017) to tune their flowline model, we propose that the sea level contribution for the FIS was greater than their upper estimate of  $\sim 0.13$  m.

## **5. Conclusions**

We present LGM ice thickness constraints for three locations within the WSE of Antarctica. In situ  $^{14}\text{C}$  measurements constrain the LGM thickness of the Foundation Ice Stream to at least ca. 800 m thicker than present in the Schmidt Hills and at least 320 m thicker than present in the Thomas Hills, both in the Pensacola Mountains. The Slessor Glacier was at least 310 m and up to 655 m thicker than present at the LGM. Finally, LGM ice was at least 385 m thicker than present at the Lassiter Coast. Our thickness constraints resolve a significant disconnect between previous terrestrial evidence for minimal LGM thickening in some locations from long-lived nuclides, and marine evidence for a significantly laterally expanded ice sheet with the grounding line located at the shelf edge. Our in situ  $^{14}\text{C}$  measurements made from samples at the Schmidt Hills exhibit higher than expected scatter in replicate measurements. Identifying the source of excess scatter will take further work. In terms of the contribution of the ice sheet sector to global sea level rise since the LGM, we estimate, primarily based on minimum estimates which do not constrain the upper limit of ice thickness changes, that the WSE contributed  $<4.6$  m, and possibly  $<1.5$  m.

## **Acknowledgements**

KN and BG acknowledge support from NSF-OPP grant 1542936. GB acknowledges support from NSF-OPP 1542976 and from the Ann and Gordon Getty Foundation. Geospatial support for this work provided by the Polar Geospatial Center under NSF-OPP awards 1043681 and 1559691. This work forms part of the British Antarctic Survey 'Polar Science for Planet Earth' programme, funded by the Natural Environment Research Council.



## **References**

- Ackert, R. P., Mukhopadhyay, S., Parizek, B. R. and Borns, H. W.: Ice elevation near the West Antarctic Ice Sheet divide during the Last Glaciation, *Geophys. Res. Lett.*, 34(21), 1–6, doi:10.1029/2007GL031412, 2007.
- Arndt, J. E., Schenke, H. W., Jakobsson, M., Nitsche, F. O., Buys, G., Goleby, B., Rebesco, M., Bohoyo, F., Hong, J., Black, J., Greku, R., Udintsev, G., Barrios, F., Reynoso-Peralta, W., Taisei, M. and Wigley, R.: The international bathymetric chart of the Southern Ocean (IBCSO) version 1.0-A new bathymetric compilation covering circum-Antarctic waters, *Geophys. Res. Lett.*, 40(12), 3111–3117, doi:10.1002/grl.50413, 2013.
- Arndt, J. E., Hillenbrand, C.-D., Grobe, H., Kuhn, G. and Wacker, L.: Evidence for a dynamic grounding line in outer Filchner Trough, Antarctica, until the early Holocene, *Geology*, 45(11), 1035–1038, doi:10.1130/G39398.1, 2017.
- Balco, G., Stone, J. O., Lifton, N. A. and Dunai, T. J.: A complete and easily accessible means of calculating surface exposure ages or erosion rates from  $^{10}\text{Be}$  and  $^{26}\text{Al}$  measurements, *Quat. Geochronol.*, 3(3), 174–195, doi:10.1016/j.quageo.2007.12.001, 2008.
- Balco, G., Todd, C., Huybers, K., Campbell, S., Vermeulen, M., Hegland, M., Goehring, B. M. and Hillebrand, T. R.: Cosmogenic-nuclide exposure ages from the Pensacola Mountains adjacent to the foundation ice stream, Antarctica, *Am. J. Sci.*, 316(6), 542–577, doi:10.2475/06.2016.02, 2016.

- Balco, G., Todd, C., Goehring, B.M., Moening-Swanson, I., Nichols, K.: Glacial geology and cosmogenic-nuclide exposure ages from the Tucker Glacier - Whitehall Glacier confluence, northern Victoria Land, Antarctica, *Am. J. Sci.*, 319(April), 255–286, doi:10.2475/04.2019.01, 2019.
- Bassett, S. E., Milne, G. A., Bentley, M. J. and Huybrechts, P.: Modelling Antarctic sea-level data to explore the possibility of a dominant Antarctic contribution to meltwater pulse IA, *Quat. Sci. Rev.*, 26(17–18), 2113–2127, doi:10.1016/j.quascirev.2007.06.011, 2007.
- Bentley, M. J. and Anderson, J. B.: Glacial and marine geological evidence for the ice sheet configuration in the Weddell Sea–Antarctic Peninsula region during the Last Glacial Maximum, *Antarct. Sci.*, 10(3), 309–325, doi:10.1017/s0954102098000388, 1998.
- Bentley, M. J., Fogwill, C. J., Kubik, P. W. and Sugden, D. E.: Geomorphological evidence and cosmogenic  $^{10}\text{Be}/^{26}\text{Al}$  exposure ages for the Last Glacial Maximum and deglaciation of the Antarctic Peninsula Ice Sheet, *Geol. Soc. Am. Bull.*, 118(9–10), 1149–1159, doi:10.1130/B25735.1, 2006.
- Bentley, M. J., Fogwill, C. J., Brocq, A. M. Le, Hubbard, A. L., Sugden, D. E., Dunai, T. J. and Freeman, S. P. H. T.: Deglacial history of the West Antarctic Ice Sheet in the Weddell Sea embayment: Constraints on past ice volume change, *Geology*, 38(5), 411–414, doi:10.1130/G30754.1, 2010.
- Bentley, M. J., Hein, A. S., Sugden, D. E., Whitehouse, P. L., Shanks, R., Xu, S. and Freeman, S. P. H. T.: Deglacial history of the Pensacola Mountains, Antarctica from glacial geomorphology and cosmogenic nuclide surface exposure dating, *Quat. Sci. Rev.*, 158, 58–76, doi:10.1016/j.quascirev.2016.09.028, 2017.
- Briggs, R. D., Pollard, D. and Tarasov, L.: A data-constrained large ensemble analysis of Antarctic evolution since the Eemian, *Quat. Sci. Rev.*, 103, 91–115, doi:10.1016/j.quascirev.2014.09.003, 2014.
- Le Brocq, A. M., Bentley, M. J., Hubbard, A., Fogwill, C. J., Sugden, D. E. and Whitehouse, P. L.: Reconstructing the Last Glacial Maximum ice sheet in the Weddell Sea embayment, Antarctica, using numerical modelling constrained by field evidence, *Quat. Sci. Rev.*, 30(19–20), 2422–2432, doi:10.1016/j.quascirev.2011.05.009, 2011.

- Chmeleff, J., Blanckenburg, F. Von, Kossert, K. and Jakob, D.: Determination of the  $^{10}\text{Be}$  half-life by multicollector ICP-MS and liquid scintillation counting, *Nucl. Inst. Methods Phys. Res. B*, 268(2), 192–199, doi:10.1016/j.nimb.2009.09.012, 2010.
- Crawford, K., Kuhn, G. and Hambrey, M.: Changes in the character of glaciomarine sedimentation in the southwestern Weddell Sea, Antarctica: evidence from the core PS1423-2, *Ann. Glaciol.*, 22, 200–204, 10.3189/1996AoS22-1-200-204, 1996.
- Fogwill, C. J., Bentley, M. J., Sugden, D. E., Kerr, A. R. and Kubik, P. W.: Cosmogenic nuclides  $^{10}\text{Be}$  and  $^{26}\text{Al}$  imply limited Antarctic Ice Sheet thickening and low erosion in the Shackleton Range for  $>1$  m.y, *Geology*, 32(3), 265–268, doi:10.1130/G19795.1, 2004.
- Fogwill, C.J., Turney, C.S.M., Golledge, N.R., Rood, D.H., Hippe, K., Wacker, L., Wieler, R., Rainsley, E.B. and Jones, R.S.: Drivers of abrupt Holocene shifts in West Antarctic ice stream direction determined from combined ice sheet modelling and geologic signatures, *Antarctic Science*, 26(6), 674–686, doi:10.1017/S0954102014000613, 2014.
- Fülöp, R. H., Fink, D., Yang, B., Codilean, A. T., Smith, A., Wacker, L., Levchenko, V. and Dunai, T. J.: The ANSTO – University of Wollongong in-situ  $^{14}\text{C}$  extraction laboratory, *Nucl. Instruments Methods Phys. Res. Sect. B Beam Interact. with Mater. Atoms*, 438, 204–213, doi:10.1016/j.nimb.2018.04.018, 2019.
- Gjermundsen, E. F., Briner, J. P., Akçar, N., Foros, J., Kubik, P. W., Salvigsen, O. and Hormes, A.: Minimal erosion of Arctic alpine topography during late Quaternary glaciation, *Nat. Geosci.*, 8(10), 789–792, doi:10.1038/ngeo2524, 2015.
- Goehring, B. M., Wilson, J. and Nichols, K.: A fully automated system for the extraction of in situ cosmogenic carbon-14 in the Tulane University cosmogenic nuclide laboratory, *Nucl. Instruments Methods Phys. Res. Sect. B Beam Interact. with Mater. Atoms*, 455, 284–292, doi:10.1016/j.nimb.2019.02.006, 2019.
- Golledge, N. R., Menviel, L., Carter, L., Fogwill, C. J., England, M. H., Cortese, G. and Levy, R. H.: Antarctic contribution to meltwater pulse 1A from reduced Southern Ocean overturning, *Nat. Commun.*, 5, 1–10, doi:10.1038/ncomms6107, 2014.
- Hedges, R. E. M., Housley, R. A., Ramsey, C. B. and Van Klinken, G. J.: Radiocarbon Dates from the Oxford AMS System: Archaeometry Datelist 19, *Archaeometry*, 37(1), 195–214, 1995.

- Hein, A. S., Fogwill, C. J., Sugden, D. E. and Xu, S.: Glacial/interglacial ice-stream stability in the Weddell Sea embayment, Antarctica, *Earth Planet. Sci. Lett.*, 307(1–2), 211–221, doi:10.1016/j.epsl.2011.04.037, 2011.
- Hein, A. S., Fogwill, C. J., Sugden, D. E. and Xu, S.: Geological scatter of cosmogenic-nuclide exposure ages in the Shackleton Range, Antarctica: Implications for glacial history, *Quat. Geochronol.*, 19, 52–66, doi:10.1016/j.quageo.2013.03.008, 2014.
- Hein, A. S., Marrero, S. M., Woodward, J., Dunning, S. A., Winter, K., Westoby, M. J., Freeman, S. P. H. T., Shanks, R. P. and Sugden, D. E.: Mid-Holocene pulse of thinning in the Weddell Sea sector of the West Antarctic ice sheet, *Nat. Commun.*, 7, 1–8, doi:10.1038/ncomms12511, 2016.
- Herber, L. J.: Separation of feldspar from quartz by flotation, *Am. Mineral.*, 54, 1212–1215, doi:10.4144/rpsj1954.25.192, 1969.
- Hillenbrand, C. D., Melles, M., Kuhn, G. and Larter, R. D.: Marine geological constraints for the grounding-line position of the Antarctic Ice Sheet on the southern Weddell Sea shelf at the Last Glacial Maximum, *Quat. Sci. Rev.*, 32, 25–47, doi:10.1016/j.quascirev.2011.11.017, 2012.
- Hillenbrand, C. D., Bentley, M. J., Stollendorf, T. D., Hein, A. S., Kuhn, G., Graham, A. G. C., Fogwill, C. J., Kristoffersen, Y., Smith, J. A., Anderson, J. B., Larter, R. D., Melles, M., Hodgson, D. A., Mulvaney, R. and Sugden, D. E.: Reconstruction of changes in the Weddell Sea sector of the Antarctic Ice Sheet since the Last Glacial Maximum, *Quat. Sci. Rev.*, 100, 111–136, doi:10.1016/j.quascirev.2013.07.020, 2014.
- Hodgson, D. A., Bentley, M. J., Schnabel, C., Cziferszky, A., Fretwell, P., Convey, P. and Xu, S.: Glacial geomorphology and cosmogenic  $^{10}\text{Be}$  and  $^{26}\text{Al}$  exposure ages in the northern Dufek Massif, Weddell Sea embayment, Antarctica, *Antarct. Sci.*, 24(4), 377–394, doi:10.1017/S0954102012000016, 2012.
- Howat, I. M., Porter, C., Smith, B. E., Noh, M.-J. and Morin, P.: The Reference Elevation Model of Antarctica, *Cryosph. Discuss.*, 13, 1–16, doi:10.5194/tc-2018-240, 2019.
- Johnson, J. S., Nichols, K. A., Goehring, B. M., Balco, G. and Schaefer, J. M.: Abrupt mid-Holocene ice loss in the western Weddell Sea Embayment of Antarctica, *Earth Planet. Sci. Lett.*, 518, 127–135, doi:10.1016/j.epsl.2019.05.002, 2019.

- Joughin, I., Bamber, J. L., Scambos, T., Tulaczyk, S., Fahnestock, M. and MacAyeal, D. R.: Integrating satellite observations with modelling: Basal shear stress of the Filcher-Ronne ice streams, Antarctica, *Philos. Trans. R. Soc. A Math. Phys. Eng. Sci.*, 364(1844), 1795–1814, doi:10.1098/rsta.2006.1799, 2006.
- Jull, A. J. T., Scott, E. M. and Bierman, P.: The CRONUS-Earth inter-comparison for cosmogenic isotope analysis, *Quat. Geochronol.*, 26(1), 3–10, doi:10.1016/j.quageo.2013.09.003, 2015.
- Korschinek, G., Bergmaier, A., Faestermann, T., Gerstmann, U. C., Knie, K., Rugel, G., Wallner, A., Dillmann, I., Dollinger, G., Lierse von Gostomski, C., Kossert, K., Maiti, M., Poutivtsev, M. and Remmert, A.: A new value for the half-life of  $^{10}\text{Be}$  by Heavy-Ion Elastic Recoil Detection and liquid scintillation counting, *Nucl. Inst. Methods Phys. Res. B*, 268(2), 187–191, doi:10.1016/j.nimb.2009.09.020, 2010.
- Lamp, J. L., Young, N. E., Koffman, T., Schimmelpfennig, I., Tuna, T., Bard, E. and Schaefer, J. M.: Update on the cosmogenic in situ  $^{14}\text{C}$  laboratory at the Lamont-Doherty Earth Observatory, *Nucl. Instruments Methods Phys. Res. Sect. B Beam Interact. with Mater. Atoms*, 465, 157–162, doi:10.1016/j.nimb.2019.05.064, 2019.
- Larter, R. D., Graham, A. G. C., Hillenbrand, C.-D., Smith, J. A. and Gales, J. A.: Late Quaternary grounded ice extent in the Filchner Trough, Weddell Sea, Antarctica: New marine geophysical evidence, *Quat. Sci. Rev.*, 53(C), 111–122, doi:10.1016/j.quascirev.2012.08.006, 2012.
- Lifton, N., Sato, T. and Dunai, T. J.: Scaling in situ cosmogenic nuclide production rates using analytical approximations to atmospheric cosmic-ray fluxes, *Earth Planet. Sci. Lett.*, 386, 149–160, doi:10.1016/j.epsl.2013.10.052, 2014.
- Marchant, D. R., Denton, G. H. and Swisher, C. C.: Miocene-Pliocene-Pleistocene Glacial History of Arena Valley, Quartermain Mountains, Antarctica, *Geogr. Ann. Ser. A, Phys. Geogr.*, 75(4), 269–301, doi:10.2307/521204, 1993.
- Nichols, K. A. and Goehring, B. M.: Isolation of quartz for cosmogenic in situ  $^{14}\text{C}$  analysis, *Geochronol. Discuss.*, doi.org/10.5194/gchron-2019-7, in review, 2019.
- Norris, T. L., Gancarz, A. J., Rokop, D. J. and Thomas, K. W.: Half-Life of  $^{26}\text{Al}$ , *J. Geophys. Res.*, 88, B331–B333, 1983.

- Peltier, W. R. and Fairbanks, R. G.: Global glacial ice volume and Last Glacial Maximum duration from an extended Barbados sea level record, *Quat. Sci. Rev.*, 25(23–24), 3322–3337, doi:10.1016/j.quascirev.2006.04.010, 2006.
- Pollard, D., Chang, W., Haran, M., Applegate, P. and DeConto, R.: Large ensemble modeling of the last deglacial retreat of the West Antarctic Ice Sheet: Comparison of simple and advanced statistical techniques, *Geosci. Model Dev.*, 9(5), 1697–1723, doi:10.5194/gmd-9-1697-2016, 2016.
- Pollard, D., Gomez, N. and Deconto, R. M.: Variations of the Antarctic Ice Sheet in a Coupled Ice Sheet-Earth-Sea Level Model: Sensitivity to Viscoelastic Earth Properties, *J. Geophys. Res. Earth Surf.*, 122(11), 2124–2138, doi:10.1002/2017JF004371, 2017.
- Rignot, E., Mouginot, J. and Scheuchl, B.: Antarctic grounding line mapping from differential satellite radar interferometry, *Geophys. Res. Lett.*, 38, 1–6, doi:10.1029/2011GL047109, 2011.
- Rignot, E., Mouginot, J., Morlighem, M., Seroussi, H. and Scheuchl, B.: Widespread, rapid grounding line retreat of Pine Island, Thwaites, Smith, and Kohler glaciers, West Antarctica, from 1992 to 2011, *Geophys. Res. Lett.*, 41, 3502–3509, doi:10.1002/2014GL060140, 2014.
- Rignot, E., J. Mouginot, and B. Scheuchl.: MEaSURES Antarctic Grounding Line from Differential Satellite Radar Interferometry, Version 2, [All subsets], NASA National Snow and Ice Data Center Distributed Active Archive Center, <https://doi.org/10.5067/IKBWW4RYHF1Q>, [Accessed 9th January 2019], 2016.
- Simms, A. R., Lisiecki, L., Gebbie, G., Whitehouse, P. L. and Clark, J. F.: Balancing the last glacial maximum (LGM) sea-level budget, *Quat. Sci. Rev.*, 205, 143–153, doi:10.1016/j.quascirev.2018.12.018, 2019.
- Stone, J. O., Balco, G. A., Sugden, D. E., Caffee, M. W., Sass, L. C., Cowdery, S. G. and Siddoway, C.: Holocene deglaciation of Marie Byrd Land, West Antarctica, *Science*, 299, 99–102, doi:10.1126/science.1077998, 2003.
- Stroeven, A. P., Fabel, D., Harbor, J., Hättstrand, C. and Kleman, J.: Quantifying the erosional impact of the Fennoscandian ice sheet in the Torneträsk-Narvik corridor, northern Sweden, based on cosmogenic radionuclide data, *Geogr. Ann. Ser. A Phys. Geogr.*, 84(3–4), 275–287, doi:10.1111/j.0435-3676.2002.00182.x, 2002.
- Sugden, D. E., Balco, G., Sass, L. C., Cowdery, S. G. and Stone, J. O.: Selective glacial erosion

and weathering zones in the coastal mountains of Marie Byrd Land, Antarctica, *Geomorphology*, 67(3–4), 317–334, doi:10.1016/j.geomorph.2004.10.007, 2005.

Sugden, D. E., Hein, A. S., Woodward, J., Marrero, S. M., Rodes, A., Dunning, S. A., Stuart, F.

M., Freeman, S. P. H. T., Winter, K. and Westoby, M. J.: The million-year evolution of the glacial trimline in the southernmost Ellsworth Mountains, Antarctica, *Earth Planet. Sci. Lett.*, 469, 42–52, doi:10.1016/j.epsl.2017.04.006, 2017.

Whitehouse, P. L., Bentley, M. J. and Le Brocq, A. M.: A deglacial model for Antarctica:

Geological constraints and glaciological modelling as a basis for a new model of Antarctic glacial isostatic adjustment, *Quat. Sci. Rev.*, 32, 1–24, doi:10.1016/j.quascirev.2011.11.016, 2012.

Whitehouse, P. L., Bentley, M. J., Vieli, A., Jamieson, S. S. R., Hein, A. S. and Sugden, D. E.:

Controls on Last Glacial Maximum ice extent in the Weddell Sea embayment, Antarctica, *J. Geophys. Res. Earth Surf.*, 122(1), 371–397, doi:10.1002/2016JF004121, 2017.

Wolstencroft, M., King, M. A., Whitehouse, P. L., Bentley, M. J., Nield, G. A., King, E. C.,

McMillan, M., Shepherd, A., Barletta, V., Bordoni, A., Riva, R. E. M., Didova, O. and Gunter, B. C.: Uplift rates from a new high-density GPS network in Palmer Land indicate significant late Holocene ice loss in the southwestern Weddell Sea, *Geophys. J. Int.*, 203(1), 737–754, doi:10.1093/gji/ggv327, 2015.

**Supplement**

Study Site	Sub-site	Sample ID	Type	Latitude	Longitude	Elevation (m asl)	Shielding factor	Thickness (cm)
	Mt Coulter south peak	10-MPS-035-CSP	E	-83.29642	-58.12907	256.0	0.9942	5.0
	Mt Coulter south peak	10-MPS-031-CSP	E	-83.29642	-58.12907	256.1	0.9942	7.0
	Mt Coulter south peak	10-MPS-022-CSP	E	-83.29109	-58.10028	352.4	0.9937	6.0
	Mt Coulter south peak	10-MPS-024-CSP	E	-83.29109	-58.10028	353.6	0.9937	5.0
	No Name Spur	10-MPS-043-NNS	E	-83.28226	-58.16298	417.0	0.9942	4.5
	No Name Spur	10-MPS-046-NNS	E	-83.27825	-58.16226	499.3	0.9958	10.0
	No Name Spur	10-MPS-038-NNS	E	-83.27782	-58.14376	550.6	0.9986	5.0
Schmidt Hills	No Name Spur	10-MPS-039-NNS	E	-83.27782	-58.14376	550.6	0.9986	5.0
	No Name Spur	10-MPS-008-NNS	E	-83.27115	-58.11433	713.2	0.9997	6.0
	No Name Spur	10-MPS-013-NNS	E	-83.27087	-58.11204	719.2	0.9997	4.5
	No Name Spur	10-MPS-012-NNS	E	-83.27025	-58.10951	725.6	0.9999	5.0
	Mt Coulter main massif	10-MPS-006-COU	E	-83.28515	-57.97676	922.8	0.9945	4.5
	Mt Coulter south peak	10-MPS-015-CSP	E	-83.29515	-57.97547	945.1	0.9998	4.0
	Mt Coulter south peak	10-MPS-016-CSP	E	-83.29484	-57.97671	948.3	0.9999	9.0
	Mt Nervo	10-MPS-051-NVO	B	-83.23921	-57.93532	1034.0	1.0000	3.3
Thomas Hills	Mt Warnke summit	11-ATH-201-WAR	E	-84.34063	-64.86995	866.0	0.9999	6.0
		11-ATH-202-WAR	E	-84.34055	-64.86749	863.0	0.9991	7.0
Lassiter Coast	Coastal Bowman Pen.	P11.14.1	B	-74.57452	-62.48812	510.0	0.9771	3.5
	Coastal Bowman Pen.	P11.11.4	B	-74.57352	-62.48075	628.0	0.9974	3.2



	Mt Lampert	P11.13.3	B	-74.54893	-62.5897	710.0	0.9774	4.7
	Mt Lampert	P11.13.5	B	-74.54652	-62.5919	768.0	0.9975	3.0
	Mt Lampert	P11.13.6	B	-74.54567	-62.5934	795.0	0.9996	5.3
	Bowman Pen.	P11.12.1	B	-74.55700	-62.4676	800.0	0.9998	3.5
	Bowman Pen.	P11.12.2	B	-74.55505	-62.4692	830.0	0.9999	5.5
	Coastal Bowman Pen.	P11.12.6	B	-74.55322	-62.472	875.0	1.0000	3.1
		CF_60_08	E	-80.26188	-28.84317	268.0	0.9919	5.0
		CF_147_08	E	-80.27216	-28.77998	284.0	0.9997	5.0
		CF_143_08	E	-80.27383	-28.7768	308.0	0.9997	4.5
		CF_108_08	E	-80.27386	-28.73442	339.0	0.9992	5.0
Shackleton Range	Mt Skidmore	CF_104_08	E	-80.27812	-28.71819	380.0	0.9992	5.0
		CF_44_08	E	-80.28497	-28.68849	474.0	0.9919	3.5
		CF_36_08	E	-80.29020	-28.67029	576.0	0.9919	3.0
		CF_120_08	E	-80.32436	-28.85522	808.0	0.9992	4.0
		CF_119_08	B	-80.32545	-28.83897	825.0	0.9992	5.0
		CF_184_08	E	-80.38455	-30.06789	239.0	0.9968	4.5
	Mt Provender	CF_160_08	B	-80.38144	-29.95613	893.0	0.9982	4.5

**Table S2. 1:** Sample information. Photographs for samples (where available) available in ICE-D at <http://antarctica.ice-d.org>.

Study Site	Sub-site	Sample ID	TUCNL	AMS Lab	AMS ID	Quartz weight (g)	C yield (µg)
	Mt Coulter south peak	10-MPS-035-CSP	163	NOSAMS	N/A9	6.031	32.9
	Mt Coulter south peak	10-MPS-031-CSP	126	LLNL	176522	2.414	52.1
	Mt Coulter south peak	10-MPS-022-CSP	96	LLNL	176186	6.089	68.4
	Mt Coulter south peak	10-MPS-024-CSP	97	LLNL	176187	6.082	56.7
	No Name Spur	10-MPS-043-NNS	291	NOSAMS	OS-140541	5.090	55.4
	No Name Spur	10-MPS-046-NNS	103	LLNL	176509	5.058	40.2
	No Name Spur	10-MPS-038-NNS	125	LLNL	176521	5.055	38.1
Schmidt Hills	No Name Spur	10-MPS-039-NNS	137	LLNL	176866	4.991	44.8
	No Name Spur	10-MPS-008-NNS	105	LLNL	176511	5.105	49.6
	No Name Spur	10-MPS-013-NNS	136	LLNL	176865	5.356	70.1
	No Name Spur	10-MPS-012-NNS	139	LLNL	176867	4.499	38.8
	Mt Coulter main massif	10-MPS-006-COU	107	LLNL	176513	5.011	52.9
	Mt Coulter south peak	10-MPS-015-CSP	101	LLNL	176507	5.023	31.4
	Mt Coulter south peak	10-MPS-016-CSP	102	LLNL	176508	4.994	46.8
	Mt Nervo	10-MPS-051-NVO	393	NOSAMS	OS-144278	2.002	28.6
	No Name Spur	10-MPS-046-NNS	300	NOSAMS	OS-141775	10.015	89.9
	No Name Spur	10-MPS-039-NNS	301	NOSAMS	OS-141776	4.983	37.9
Repeat measurements	No Name Spur	10-MPS-013-NNS	298	NOSAMS	OS-141773	10.044	114.1
	Mt Coulter main massif	10-MPS-006-COU	297	NOSAMS	OS-141790	10.057	84.6
	No Name Spur	10-MPS-046-NNS	334	NOSAMS	OS-143032	3.114	31.5

	No Name Spur	10-MPS-013-NNS	331	NOSAMS	OS-143028	3.051	32.5
	Mt Coulter main massif	10-MPS-006-COU	332	NOSAMS	OS-143029	3.119	31.1
Thomas Hills	Mt Warnke summit	11-ATH-201-WAR	305	NOSAMS	OS-141780	6.018	57.7
		11-ATH-202-WAR	306	NOSAMS	OS-141781	5.216	38.6
	Coastal Bowman Pen.	P11.14.1	384	NOSAMS	OS-146891	4.996	3.9
	Coastal Bowman Pen.	P11.11.4	218	NOSAMS	OS-136997	5.106	11.3
	Mt Lampert	P11.13.3	181	NOSAMS	OS-134207	4.915	8.6
Lassiter Coast	Mt Lampert	P11.13.5	214	NOSAMS	OS-136996	5.079	13.3
	Mt Lampert	P11.13.6	182	NOSAMS	OS-134208	4.982	9.0
	Bowman Pen.	P11.12.1	177	NOSAMS	OS-134202	4.941	7.4
	Bowman Pen.	P11.12.2	180	NOSAMS	OS-134205	4.928	9.4
	Coastal Bowman Pen.	P11.12.6	264	NOSAMS	OS-139206	3.040	5.9
		CF_60_08	272	NOSAMS	OS-139204	5.006	24.4
		CF_147_08	296	NOSAMS	OS-141771	4.467	62.4
		CF_143_08	271	NOSAMS	OS-139201	5.085	23.7
		CF_108_08	294	NOSAMS	OS-141770	5.043	116.2
Shackleton Range	Mt Skidmore	CF_104_08	270	NOSAMS	OS-139197	4.993	38.5
		CF_44_08	269	NOSAMS	OS-139203	4.967	13.1
		CF_36_08	267	NOSAMS	OS-139202	5.032	18.9
		CF_120_08	265	NOSAMS	OS-139199	2.954	96.2
		CF_119_08	266	NOSAMS	OS-139198	4.944	11.3
		CF_184_08	302	NOSAMS	OS-141778	4.028	87.1
	Mt Provender	CF_160_08	303	NOSAMS	OS-141779	3.970	31.0

$\pm 1\sigma$ ( $\mu\text{g}$ )	Diluted Gas Mass ( $\mu\text{g}$ )	$\pm 1\sigma$ ( $\mu\text{g}$ )	$^{14}\text{C}/^{13}\text{C}$ corrected	$\pm 1\sigma$	$\delta^{13}\text{C}$ ( $\text{‰}$ )	$\pm 1\sigma$ ( $\text{‰}$ )	$^{14}\text{C}/\text{C}$ total	$\pm 1\sigma$	total $^{14}\text{C}$ atoms blank corrected
0.4	104.4	1.3	4.14E-12	4.57E-14	-6.33	0.96	4.53E-14	5.02E-16	1.42E+05
0.7	383.2	4.9	1.47E-12	2.63E-14	-6.92	0.50	1.61E-14	2.88E-16	2.13E+05
0.9	380.6	4.9	4.16E-12	3.07E-14	-1.14	0.50	4.58E-14	3.38E-16	7.78E+05
0.7	381.6	4.9	3.37E-12	2.74E-14	-0.93	0.50	3.71E-14	3.02E-16	6.14E+05
0.7	102.2	1.3	1.52E-11	1.09E-13	-13.57	0.50	1.65E-13	1.19E-15	7.82E+05
0.5	382.2	4.9	6.14E-12	3.30E-14	0.20	0.50	6.77E-14	3.64E-16	1.20E+06
0.5	376.2	4.8	4.97E-12	5.03E-14	-3.94	0.50	5.45E-14	5.52E-16	9.33E+05
0.6	383.2	4.9	6.44E-12	2.41E-14	-6.36	0.50	7.05E-14	2.66E-16	1.26E+06
0.6	387.9	5.0	6.05E-12	5.61E-14	0.30	0.50	6.67E-14	6.19E-16	1.20E+06
0.9	382.9	4.9	7.47E-12	2.82E-14	-6.63	0.50	8.18E-14	3.10E-16	1.48E+06
0.5	346.0	4.4	5.84E-12	2.63E-14	-6.09	0.50	6.40E-14	2.90E-16	1.02E+06
0.7	378.5	4.8	8.22E-12	4.83E-14	-0.97	0.50	9.06E-14	5.33E-16	1.62E+06
0.4	383.2	4.9	6.68E-12	3.78E-14	1.45	0.50	7.37E-14	4.18E-16	1.32E+06
0.6	380.1	4.9	7.17E-12	4.60E-14	0.70	0.50	7.91E-14	5.09E-16	1.41E+06
0.4	97.6	1.2	1.11E-11	5.99E-14	-12.63	0.50	1.21E-13	6.54E-16	5.79E+05
1.2	105.5	1.4	3.75E-11	1.77E-13	-8.68	0.50	4.10E-13	1.94E-15	2.10E+06
0.5	99.3	1.3	1.49E-11	1.26E-13	-10.14	0.50	1.62E-13	1.37E-15	7.43E+05
1.5	114.1	1.5	3.45E-11	1.57E-13	-8.76	0.50	3.77E-13	1.72E-15	2.09E+06
1.1	111.7	1.4	4.43E-11	1.78E-13	-8.90	0.50	4.84E-13	1.95E-15	2.65E+06
0.4	113.1	1.4	1.28E-11	7.92E-14	-25.19	0.50	1.38E-13	8.53E-16	7.17E+05

0.4	93.9	1.2	1.20E-11	8.74E-14	-19.65	0.50	1.29E-13	9.46E-16	5.44E+05
0.4	99.7	1.3	1.48E-11	8.58E-14	-17.12	0.50	1.60E-13	9.32E-16	7.37E+05
0.7	89.9	1.2	2.86E-11	1.77E-13	-15.64	0.50	3.10E-13	1.93E-15	1.33E+06
0.5	109.5	1.4	2.03E-11	1.29E-13	-8.72	0.50	2.22E-13	1.41E-15	1.16E+06
0.1	110.4	1.4	5.90E-12	4.61E-14	-13.53	0.50	6.42E-14	5.02E-16	3.42E+05
0.1	110.8	1.4	1.41E-11	1.29E-13	-4.57	0.50	1.54E-13	1.42E-15	7.92E+05
0.1	110.6	1.4	1.37E-11	7.49E-14	-5.63†	0.50	1.50E-13	8.23E-16	7.36E+05
0.2	107.2	1.4	1.61E-11	1.44E-13	-5.00	0.50	1.77E-13	1.58E-15	8.86E+05
0.1	106.7	1.4	1.55E-11	8.38E-14	-5.63†	0.50	1.70E-13	9.21E-16	8.14E+05
0.1	106.2	1.4	1.46E-11	7.39E-14	-5.63†	0.50	1.60E-13	8.13E-16	7.54E+05
0.1	105.5	1.4	1.65E-11	8.14E-14	-5.63†	0.50	1.81E-13	8.96E-16	8.61E+05
0.1	108.8	1.4	1.01E-11	6.46E-14	-5.88	0.50	1.11E-13	7.09E-16	5.39E+05
0.3	112.9	1.4	4.26E-12	3.88E-14	-6.51	0.50	4.66E-14	4.25E-16	1.99E+05
0.8	110.9	1.4	1.52E-11	1.04E-13	-11.21	0.50	1.66E-13	1.14E-15	8.57E+05
0.3	109.8	1.4	1.42E-11	6.79E-14	-7.10	0.50	1.56E-13	7.46E-16	7.93E+05
1.5	116.2	1.5	1.50E-11	1.33E-13	-10.42	0.50	1.63E-13	1.45E-15	8.86E+05
0.5	110.2	1.4	1.52E-11	7.90E-14	-7.70	0.50	1.66E-13	8.67E-16	8.51E+05
0.2	110.2	1.4	1.36E-11	7.13E-14	-6.58	0.50	1.49E-13	7.83E-16	7.58E+05
0.2	110.5	1.4	1.68E-11	7.52E-14	-7.68	0.50	1.84E-13	8.25E-16	9.53E+05
1.2	96.2	1.2	1.20E-11	6.71E-14	-6.66	0.50	1.32E-13	7.37E-16	5.70E+05
0.1	111.8	1.4	1.72E-11	1.00E-13	-6.55	0.50	1.88E-13	1.10E-15	9.89E+05
1.1	114.7	1.5	7.15E-12	8.31E-14	-11.96	0.50	7.79E-14	9.05E-16	3.83E+05
0.4	99.8	1.3	2.70E-11	1.65E-13	-8.10	0.50	2.95E-13	1.81E-15	1.41E+06

$\pm 1\sigma$	$^{14}\text{C}$ conc.	$\pm 1\sigma$	$\pm 6\%$	$^{14}\text{C}$ age	$\pm 1\sigma_{\text{int}}$	$\pm 1\sigma_{\text{ext}}$	Effective blank	$\pm 1\sigma$	Effective Blank as % of total $^{14}\text{C}$ At Sample
(at)	(at.g-1)	(at.g-1)	(at.g-1)	(ka)	(ka)	(ka)	(at)	(at)	
7.18E+03	2.35E+04	1.11E+03	1.41E+03	1.1	0.1	0.1	9.53E+04	5.95E+03	40.2
9.03E+03	8.83E+04	2.96E+03	5.30E+03	5.5	0.5	0.6	9.53E+04	5.95E+03	30.9
1.42E+04	1.28E+05	2.08E+03	7.67E+03	8.4	0.9	1.1	9.53E+04	5.95E+03	10.9
1.23E+04	1.01E+05	1.79E+03	6.06E+03	5.8	0.5	0.7	9.53E+04	5.95E+03	13.4
1.42E+04	1.54E+05	2.52E+03	9.21E+03	10.4	1.3	1.6	6.47E+04	6.85E+03	7.6
1.90E+04	2.38E+05	3.49E+03	1.43E+04	--	--	--	9.53E+04	5.95E+03	7.4
1.78E+04	1.85E+05	2.86E+03	1.11E+04	12.0	1.6	2.1	9.53E+04	5.95E+03	9.3
1.90E+04	2.52E+05	3.67E+03	1.51E+04	--	--	--	9.53E+04	5.95E+03	7.0
2.14E+04	2.36E+05	3.46E+03	1.41E+04	15.7	2.8	3.7	9.53E+04	5.95E+03	7.3
2.18E+04	2.75E+05	3.92E+03	1.65E+04	33.4	27.7	36.0	9.53E+04	5.95E+03	6.1
1.62E+04	2.26E+05	3.43E+03	1.35E+04	13.4	2.0	2.6	9.53E+04	5.95E+03	8.6
2.49E+04	3.24E+05	4.55E+03	1.94E+04	33.2	27.0	35.1	9.53E+04	5.95E+03	5.5
2.07E+04	2.63E+05	3.80E+03	1.58E+04	12.3	1.7	2.2	9.53E+04	5.95E+03	6.7
2.24E+04	2.83E+05	4.05E+03	1.70E+04	16.3	3.1	4.0	9.53E+04	5.95E+03	6.3
9.36E+03	2.89E+05	4.39E+03	1.74E+04	12.8	1.8	2.4	1.33E+04	5.14E+03	2.3
3.04E+04	2.10E+05	2.85E+03	1.26E+04	24.2	8.8	11.4	6.47E+04	6.85E+03	3.0
1.42E+04	1.49E+05	2.49E+03	8.94E+03	7.9	0.8	1.0	6.47E+04	6.85E+03	8.0
3.01E+04	2.08E+05	2.83E+03	1.25E+04	11.2	1.4	1.8	6.47E+04	6.85E+03	3.0
3.70E+04	2.63E+05	3.52E+03	1.58E+04	13.2	1.9	2.5	6.47E+04	6.85E+03	2.4

1.31E+04	2.30E+05	3.90E+03	1.38E+04	--	--	--	6.47E+04	6.85E+03	8.3
1.13E+04	1.78E+05	3.40E+03	1.07E+04	8.3	0.9	1.1	6.47E+04	6.85E+03	10.6
1.32E+04	2.36E+05	3.96E+03	1.42E+04	10.4	1.2	1.6	6.47E+04	6.85E+03	8.1
2.11E+04	2.22E+05	3.19E+03	1.33E+04	10.1	1.2	1.5	6.47E+04	6.85E+03	4.6
1.87E+04	2.22E+05	3.27E+03	1.33E+04	10.3	1.2	1.6	6.47E+04	6.85E+03	5.3
6.94E+03	6.84E+04	1.27E+03	4.11E+03	2.9	0.2	0.3	1.33E+04	5.14E+03	3.8
1.51E+04	1.55E+05	2.53E+03	9.30E+03	7.5	0.7	0.9	6.47E+04	6.85E+03	7.6
1.30E+04	1.51E+05	2.49E+03	9.05E+03	6.7	0.6	0.8	9.53E+04	5.95E+03	11.5
1.63E+04	1.74E+05	2.75E+03	1.05E+04	7.4	0.7	0.9	6.47E+04	6.85E+03	6.8
1.40E+04	1.64E+05	2.64E+03	9.87E+03	6.7	0.6	0.8	9.53E+04	5.95E+03	10.5
1.31E+04	1.55E+05	2.54E+03	9.31E+03	6.0	0.5	0.7	9.53E+04	5.95E+03	11.2
1.44E+04	1.77E+05	2.79E+03	1.06E+04	7.2	0.7	0.9	9.53E+04	5.95E+03	10.0
1.10E+04	1.78E+05	3.41E+03	1.07E+04	6.7	0.6	0.8	6.47E+04	6.85E+03	10.7
8.01E+03	4.01E+04	1.53E+03	2.41E+03	1.9	0.1	0.2	6.47E+04	6.85E+03	24.5
1.50E+04	1.92E+05	3.05E+03	1.15E+04	--	--	--	6.47E+04	6.85E+03	7.0
1.36E+04	1.56E+05	2.55E+03	9.37E+03	13.3	2.0	2.6	6.47E+04	6.85E+03	7.5
1.63E+04	1.76E+05	2.77E+03	1.05E+04	17.5	3.6	4.7	6.47E+04	6.85E+03	6.8
1.44E+04	1.71E+05	2.73E+03	1.03E+04	14.3	2.3	3.0	6.47E+04	6.85E+03	7.1
1.33E+04	1.53E+05	2.53E+03	9.16E+03	9.3	1.0	1.3	6.47E+04	6.85E+03	7.9
1.54E+04	1.91E+05	2.94E+03	1.14E+04	12.1	1.6	2.1	6.47E+04	6.85E+03	6.4
1.12E+04	1.94E+05	3.60E+03	1.16E+04	8.4	0.9	1.1	6.47E+04	6.85E+03	10.2
1.63E+04	2.01E+05	3.07E+03	1.21E+04	8.9	1.0	1.3	6.47E+04	6.85E+03	6.1
1.03E+04	9.52E+04	2.22E+03	5.71E+03	6.1	0.5	0.7	6.47E+04	6.85E+03	14.4

2.20E+04	3.55E+05	5.06E+03	2.13E+04	--	--	--	6.47E+04	6.85E+03	4.4
----------	----------	----------	----------	----	----	----	----------	----------	-----

<sup>‡</sup>Average of values measured by isotope ratio mass spectrometry. Actual measured values otherwise.

<sup>§</sup>Representative of the blanks run during the running of the samples.

<sup>§</sup>Sample run at no cost during test run by NOMSAMS, no AMS ID

**Table S2. 2:** In situ <sup>14</sup>C analytical data and exposure ages. TUCNL column contains the Tulane University Cosmogenic Nuclide Laboratory code for each sample.



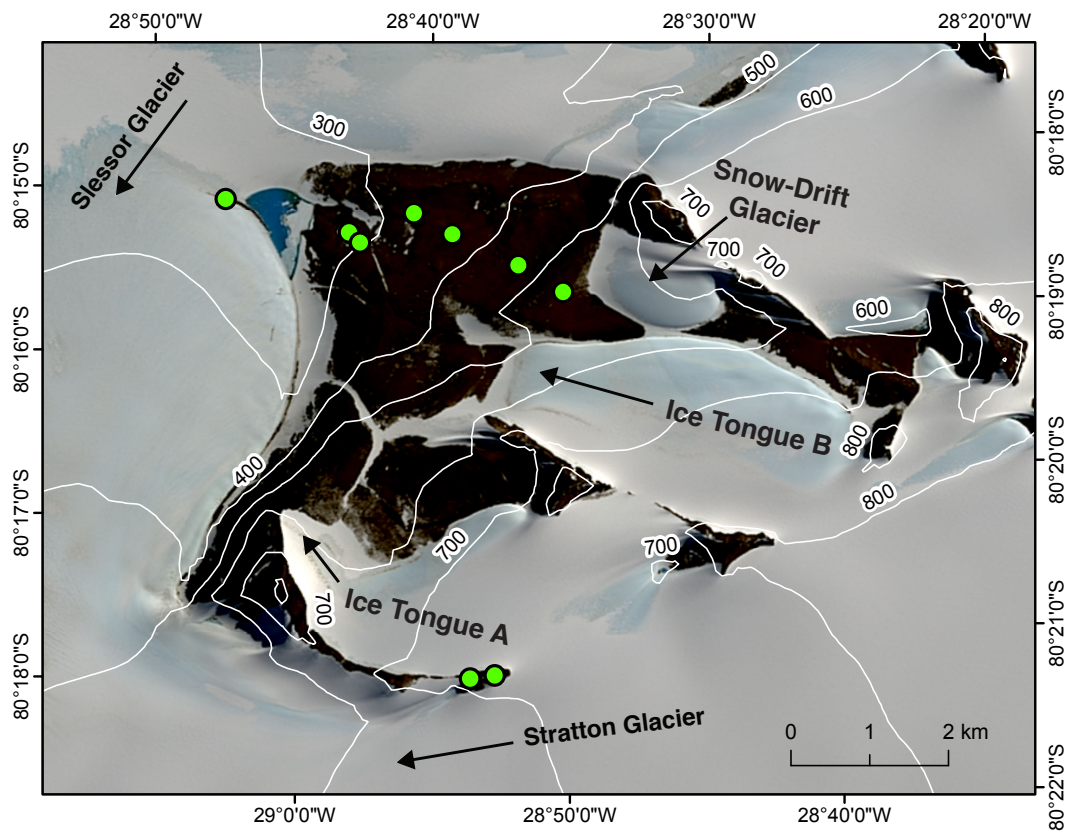


**Figure S2.1:** Sample locations at Mount Skidmore. Landsat 8 imagery courtesy of the U.S. Geological Survey. Contours at 100 m interval generated using the Reference Elevation Model of Antarctica (REMA; Howat et al., 2019).

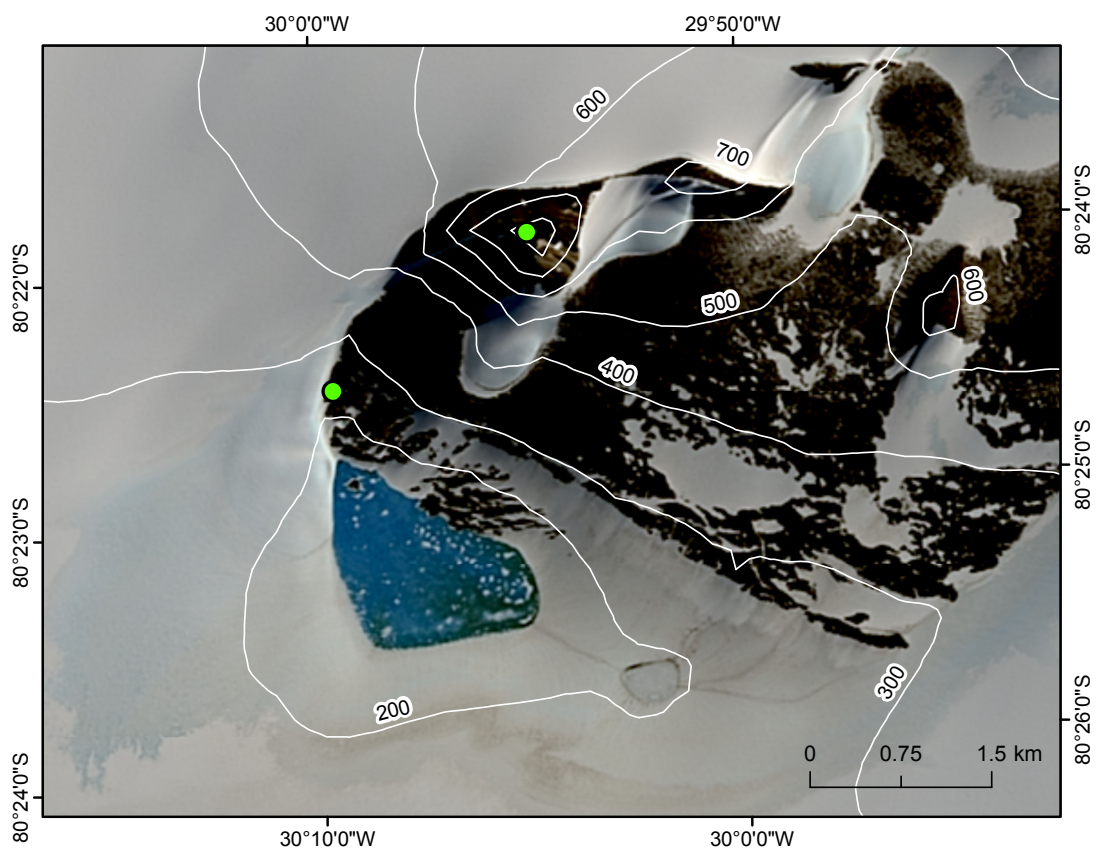


**Figure S2.2:** Sample locations at Mount Provender. Landsat 8 imagery courtesy of the U.S. Geological Survey. Contours at 100 m interval generated using the Reference Elevation Model of Antarctica (REMA; Howat et al., 2019).

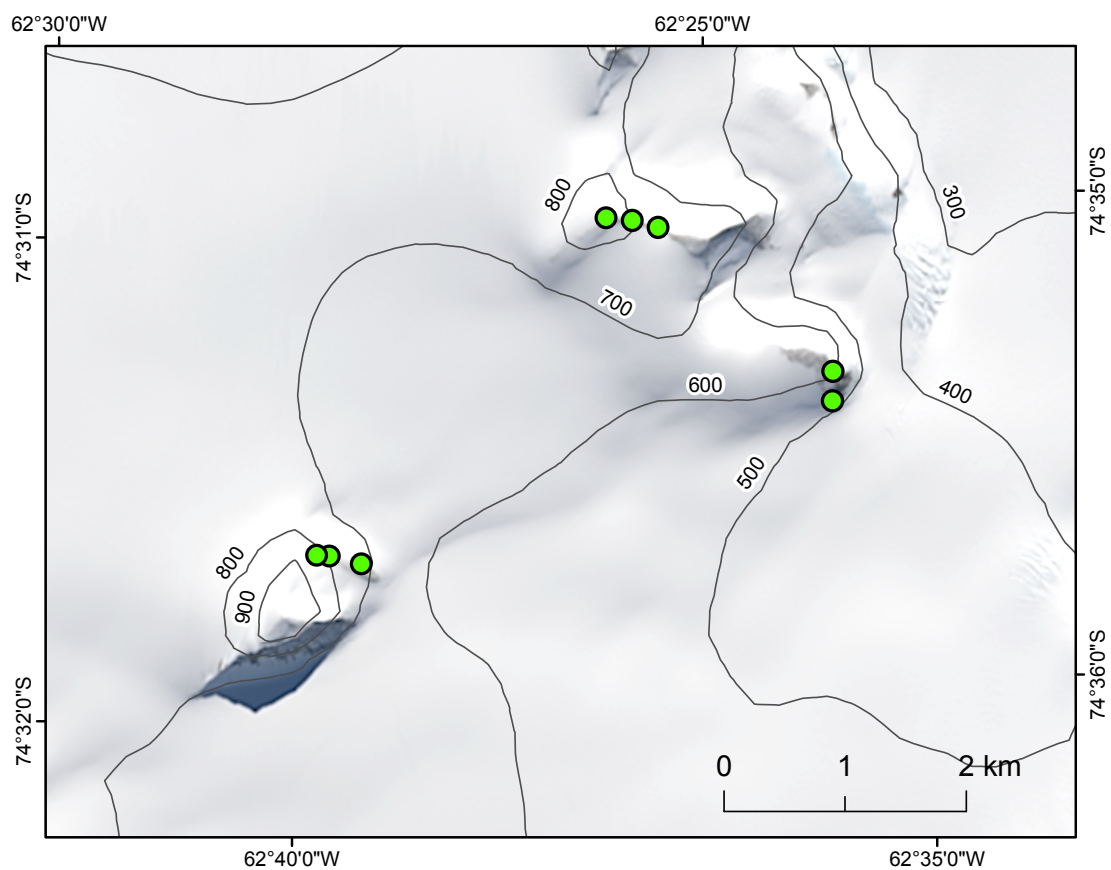


**Figure S2.3:** Sample locations on Mount Lampert and an unnamed nunatak, Lassiter Coast. Landsat 8 imagery courtesy of the U.S. Geological Survey. Contours at 100 m interval generated using the Reference Elevation Model of Antarctica (REMA; Howat et al., 2019).

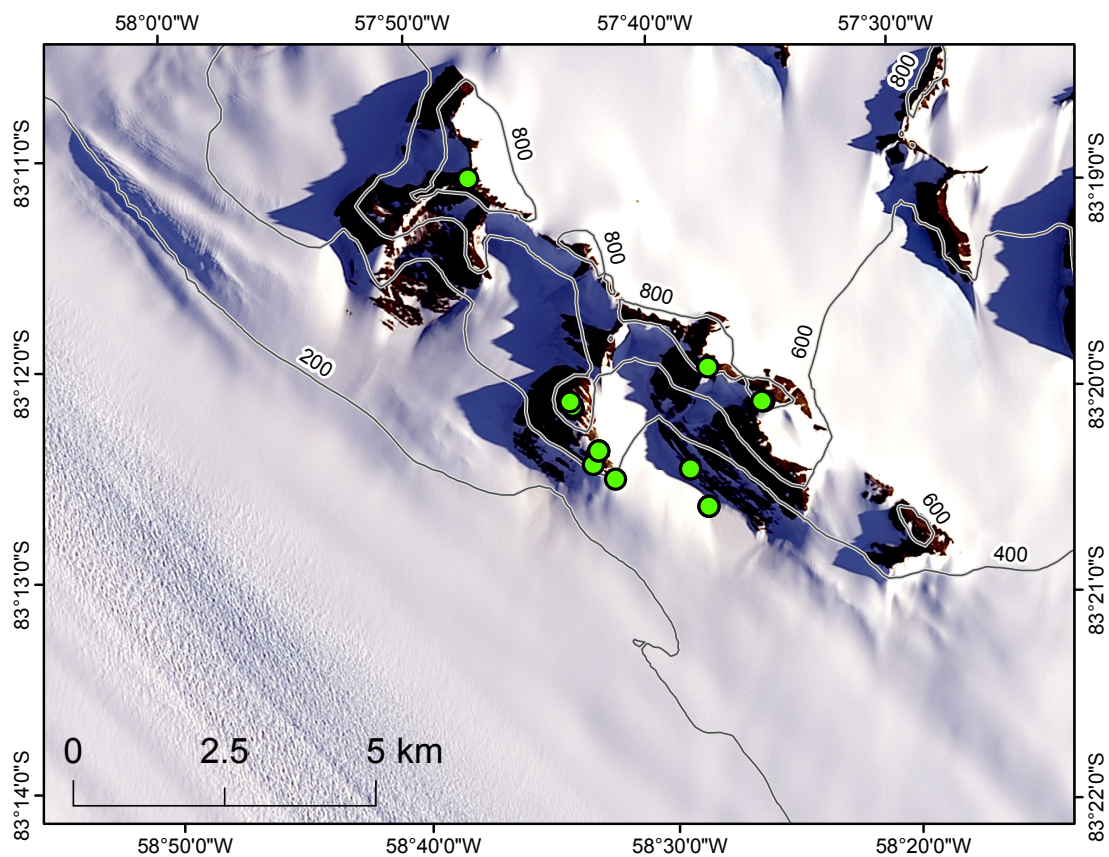


**Figure S2.4:** Sample locations in the Schmidt Hills, Pensacola Mountains. Landsat 8 imagery courtesy of the U.S. Geological Survey. Contours at 200 m interval generated using the Reference Elevation Model of Antarctica (REMA; Howat et al., 2019).



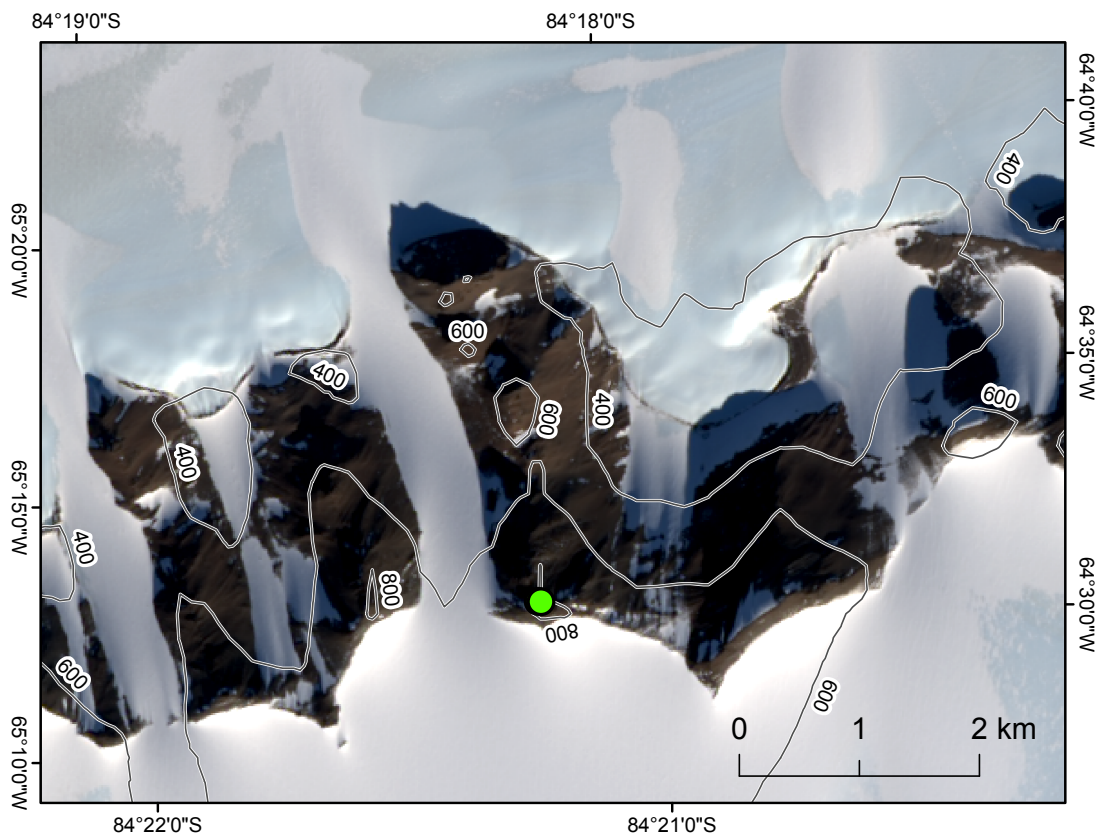


**Figure S2.5:** Sample locations in the Thomas Hills, Pensacola Mountains. Two samples were collected within close proximity such that their markers overlap. Landsat 8 imagery courtesy of the U.S. Geological Survey. Contours at 200 m interval generated using the Reference Elevation Model of Antarctica (REMA; Howat et al., 2019).

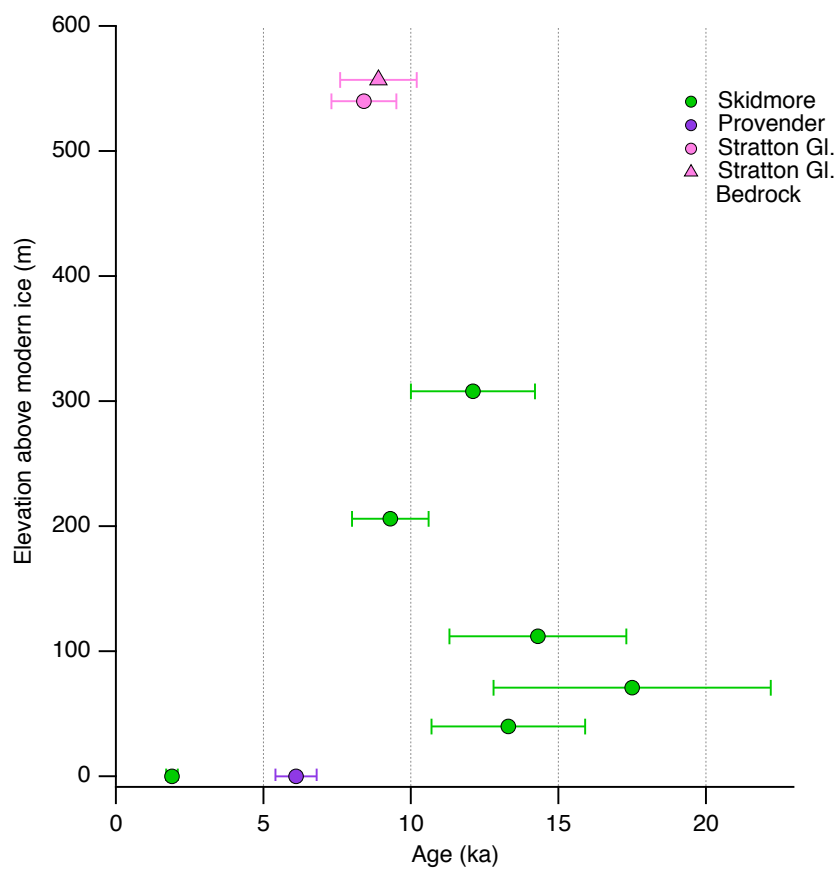


**Figure S2.6:** Elevation versus in situ <sup>14</sup>C age of samples from the Shackleton Range. Samples with in situ <sup>14</sup>C concentrations equivalent to saturation are not shown.

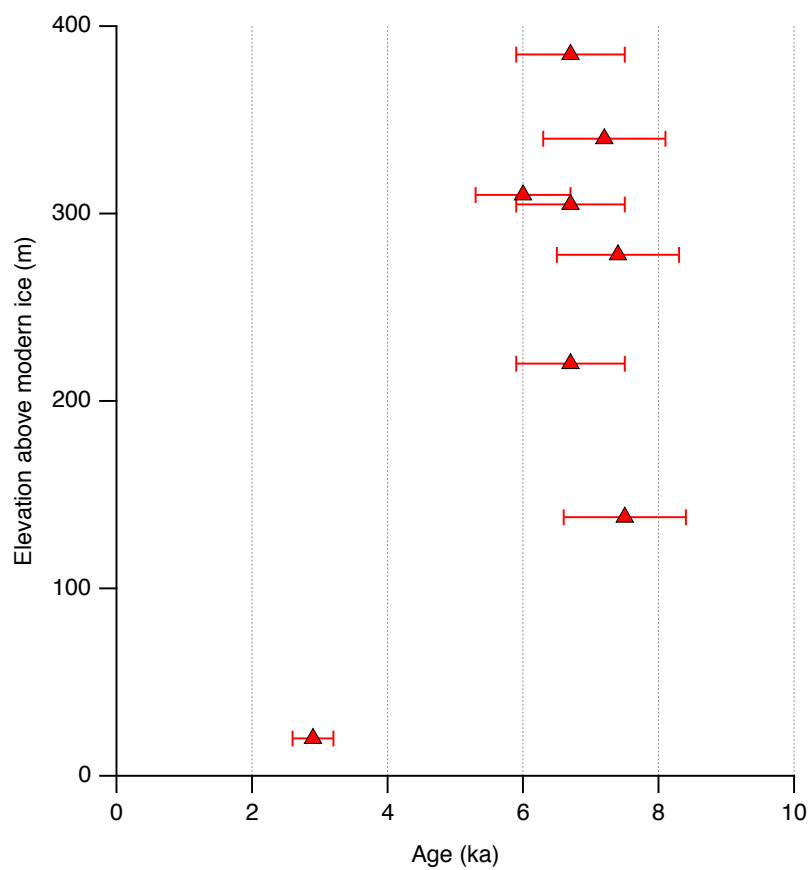


**Figure S2.7:** Elevation versus in situ  $^{14}\text{C}$  age of samples from the Lassiter Coast.

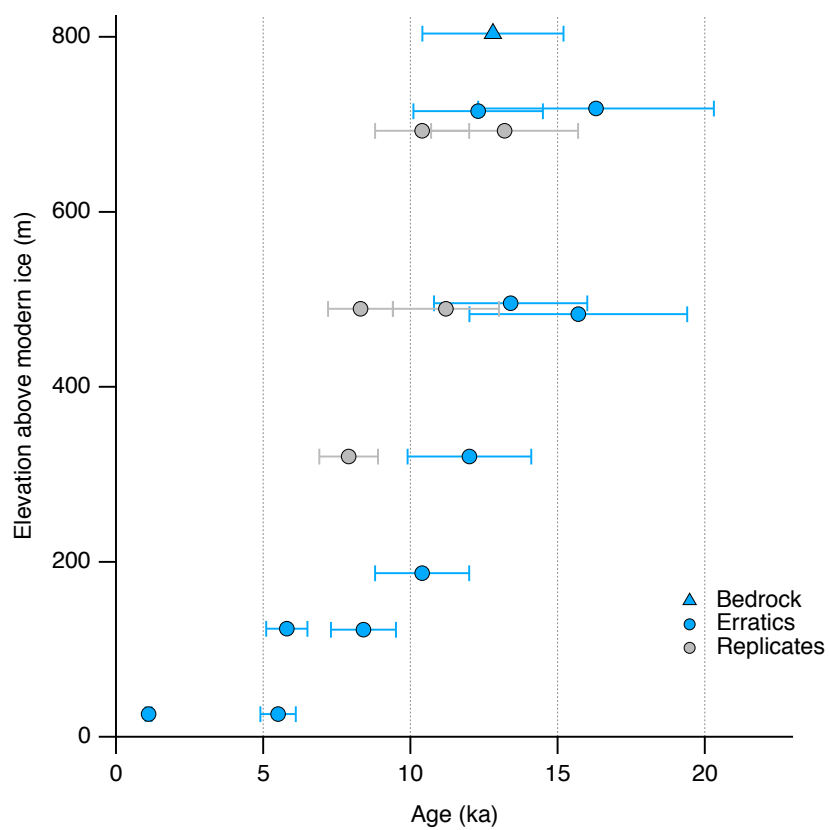


**Figure S2.8:** Elevation versus in situ <sup>14</sup>C age of samples from the Schmidt Hills. Only measurements yielding exposure ages  $\leq 20$  ka are presented.



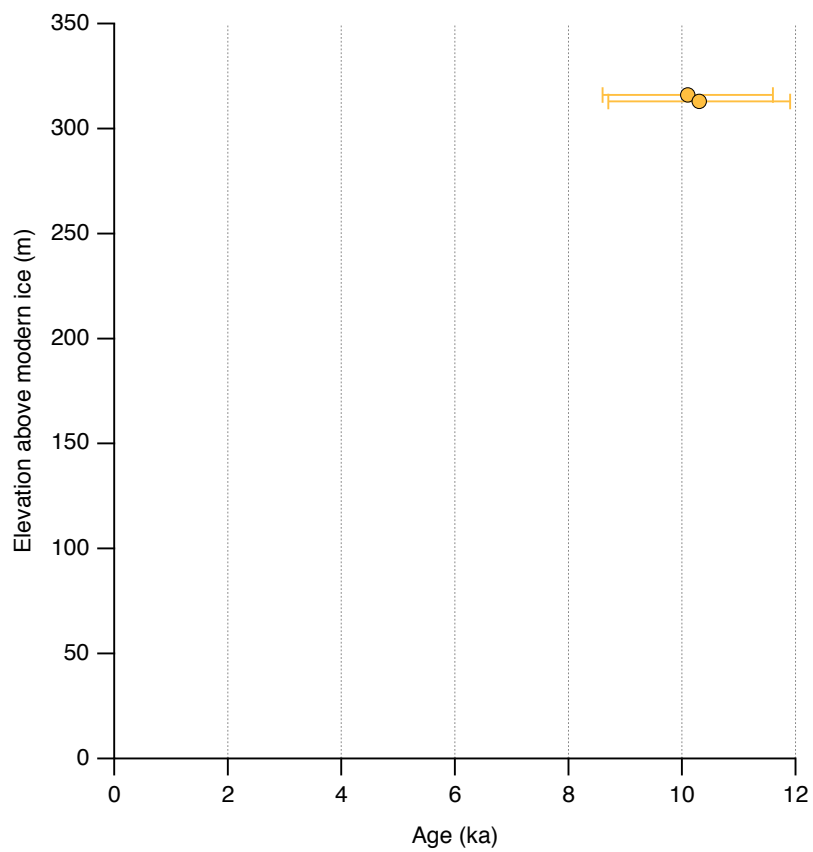


**Figure S2.9:** Elevation versus in situ  $^{14}\text{C}$  age of samples from the Thomas Hills.

### **Chapter 3. Isolation of quartz for cosmogenic in situ $^{14}\text{C}$ analysis**

Keir A. Nichols<sup>1</sup>, Brent M. Goehring<sup>1</sup>

<sup>1</sup>Department of Earth and Environmental Sciences, Tulane University, New Orleans, LA, 70118, USA

Published in *Geochronology*

<https://doi.org/10.5194/gchron-1-43-2019>

## **Abstract**

Froth flotation is a commonly used procedure for separating feldspars and micas from quartz for the preparation of quartz mineral separates to carry out cosmogenic nuclide analysis. Whilst extracting carbon from quartz we observed in situ carbon-14 ( $^{14}\text{C}$ ) concentrations which were anomalously high and in excess of theoretical geological maximum concentrations. Further etching of sample material reduced carbon yields and  $^{14}\text{C}$  concentrations, yet the latter remained unrealistically high. When quartz from the original whole rock sample was isolated in our laboratory, we observed even lower carbon yields and geologically plausible in situ  $^{14}\text{C}$  concentrations. After ruling out unlikely geological scenarios and systematic measurement issues, we decided to investigate the quartz isolation procedure as a potential source of  $^{14}\text{C}$  contamination. We hypothesised that laurylamine (dodecylamine), an organic compound used as part of the froth flotation procedure, elevates  $^{14}\text{C}$  concentrations if residual laurylamine is present. We demonstrate that laurylamine has a  $^{14}\text{C}$  modern carbon source and thus has the potential to influence in situ  $^{14}\text{C}$  measurements if present in minute but measurable quantities. Furthermore, we show that insufficient sample etching results in contaminant  $^{14}\text{C}$  persisting through step heating of quartz that is subsequently collected with the in situ component released at 1100 °C. We demonstrate that froth flotation contaminates in situ  $^{14}\text{C}$  measurements. We provide guidelines for the preparation of quartz based on methods developed in our laboratory and demonstrate that all froth flotation-derived carbon and  $^{14}\text{C}$  is removed when applied. We recommend that the procedures presented be used at a minimum when using froth flotation to isolate quartz for in situ  $^{14}\text{C}$  measurements.

## **1. Introduction**

In the course of extracting carbon from quartz we have, on multiple occasions, observed concentrations of in situ  $^{14}\text{C}$  that were anomalously high and in excess of geologically plausible maximum concentrations. We hypothesise that the elevated in situ  $^{14}\text{C}$  concentrations are sourced from part of the widely used mineral separation procedure known as froth flotation, a process that relies on three organic compounds; laurylamine (also known as dodecylamine,  $\text{C}_{12}\text{H}_{27}\text{N}$ ), eucalyptol ( $\text{C}_{10}\text{H}_{18}\text{O}$ ), and acetic acid ( $\text{C}_2\text{H}_4\text{O}_2$ ). Our observations, combined with a desire to continue use of froth flotation for the benefits it provides during quartz separation, form the motivation for this paper. In this study we

explore both the potential influence that quartz isolation procedures have on resulting measured  $^{14}\text{C}$  concentrations as well as procedures to minimise potential contamination during use of froth flotation.

Froth flotation is a method by which feldspars and, to a lesser extent, micas are separated from quartz (Herber, 1969). The method precedes acid etching as part of the quartz isolation process for cosmogenic nuclide analysis and is used by numerous cosmogenic nuclide laboratories. It is useful for samples containing large proportions of feldspars and vastly reduces the resources required to etch samples. A motivating factor for this study was the realisation that froth flotation introduces carbon to sample material through the use of three aforementioned organic compounds. Use of the organic compounds was previously of no consequence as the method was primarily used to isolate quartz for the measurement of  $^{10}\text{Be}$  and  $^{26}\text{Al}$ . There is no standard procedure for froth flotation or post-froth flotation sample etching. As a result, different laboratories use various quantities of laurylamine, eucalyptol, and acetic acid, as well as varying etching procedures, which complicates the matter further. The carbon content, and especially the  $^{14}\text{C}$  content, of the three organic compounds used in our laboratory has yet to be measured, thus the potential for contamination of in situ  $^{14}\text{C}$  measurements is unquantified.

In the first part of this work, we summarise the froth flotation procedure as well as the overall quartz isolation process used for in situ  $^{14}\text{C}$  analysis. We describe the range of methodologies used today, and detail those used at Tulane. We then describe the initial measurements that led us to hypothesise that froth flotation could be causing contamination of in situ  $^{14}\text{C}$  results. Finally, we describe the methodology and results of a systematic study that demonstrates laurylamine contains modern carbon, that froth flotation does contaminate samples with regards to both  $^{14}\text{C}$  and carbon in general, and that contaminant  $^{14}\text{C}$  can be removed with sufficient sample etching. We demonstrate that the post-froth flotation etching methodology used in our laboratory ensures that quartz is isolated effectively and without influencing the resulting in situ  $^{14}\text{C}$  measurements. We conclude that froth flotation should be applied with care if in situ  $^{14}\text{C}$  is to be measured, and that the post-froth flotation etching methodology described below should be applied at a minimum to ensure that samples are free of contaminant  $^{14}\text{C}$  from froth flotation.

## **1.1 Froth flotation and the isolation of quartz from whole rock material**

### **1.1.1 Pre-Froth Flotation**

Prior to froth flotation, whole rock material is typically crushed, milled and sieved to isolate the 250 - 500  $\mu\text{m}$  size fraction. This is then rinsed with tap or deionised water to remove any fine grain-sized material. At this point samples are ready for froth flotation, although we commonly first dry samples so that a magnetic mineral separation can be performed to remove any mafic material present prior to frothing, which we find improves overall frothing efficiency. The sample is ready for froth flotation following the removal of fine grain-sized material and the optional magnetic separation.

Our method for froth flotation is largely based on that used at PRIME Lab ([http://www.physics.purdue.edu/primelab/MSL/froth\\_floatation.html](http://www.physics.purdue.edu/primelab/MSL/froth_floatation.html)). The first stage of froth flotation is the conditioning of sample material with dilute (< 5% v/v) hydrofluoric acid (HF). Conditioning the sample makes the feldspar (and mica) grains hydrophobic and the quartz grains hydrophilic, which is key to the separation process. We condition each sample in a 1 L Nalgene bottle with enough 5 % HF/HNO<sub>3</sub> to saturate and cover the sample, without agitation beyond gently swirling the bottle a few times. The sample is left to sit for no more than five minutes before decanting the acid solution and beginning froth flotation. Some laboratories condition the sample with dilute HF (1 to 5 %) for up to 60 minutes on a shaker table; we have found that five minutes with 5 % HF/HNO<sub>3</sub> is sufficient and improves separation efficiency.

### **1.1.2 Frothing Solution**

Laurylamine is combined with glacial acetic acid by dissolution to form the frothing solution, typically at a 1:1 ratio. We combine approximately 300 ml of glacial acetic acid and 300 ml of laurylamine to form a 600 ml stock frothing solution. The frothing solution is then combined with water and carbonated or mixed with bubbly tap water. Some laboratories add the concentrated frothing solution directly to sample material, followed by the addition of carbonated or bubbly tap water. Other laboratories make the stock solution of glacial acetic acid and laurylamine and combine it with water before adding it to the sample material. For each sample, we combine approximately 6 ml of frothing solution with 20 L of water. The net concentration of both acetic acid and laurylamine in the frothing solution is 0.03% v/v. In terms of their purpose in the froth flotation procedure, laurylamine acts as a

collector agent, or surfactant, and is thus required to separate the hydrophobic and hydrophilic mineral grains. Glacial acetic acid is used because laurylamine dissolves into it more readily compared to water, and it keeps the pH of the solution low.

### **1.1.3 Froth Flotation**

A few drops of eucalyptus oil are added to the sample in a bowl (usually metal or plastic) before the frothing solution is applied to the sample. The eucalyptus oil holds the bubbles together to which the feldspar and mica grains attach. We use a hose connected to a soda-fountain carbonator to dispense the frothing solution. The now carbonated and dilute frothing solution is used to move the sample material from the 1 L bottle to the bowl. The frothing solution is then applied to the sample material in the bowl. The feldspar grains, owing to their hydrophobic nature, float to the top of the mixture whilst the quartz grains remain at the bottom. We apply 3 to 4 L of dilute frothing solution to the sample before waiting a few seconds and decanting the feldspar grains into a second bowl. The feldspar grains are usually discarded, though they may be saved for  $^{36}\text{Cl}$  analysis. The froth flotation procedure is repeated until most of the feldspar fraction has been removed or no additional separation of quartz and feldspar is accomplished. For a granitic sample of ca. 400 to 500 g, we find that five to six rounds of froth flotation are needed before either the froth flotation process is complete and the vast majority of feldspar has been removed, or froth flotation becomes less effective and the sample requires further conditioning. After reconditioning the sample in 5 % HF/HNO<sub>3</sub> for five minutes, additional rounds of froth flotation can be performed.

### **1.1.4 Post-Froth Flotation Acid Etching**

Froth flotation is followed by etching the sample in HF or HF/HNO<sub>3</sub> to remove extraneous minerals, to partially dissolve or etch the quartz grains to remove meteoric cosmogenic nuclides, and to lower major ion concentrations (e.g., Fe, Ti, Al). Generally, the etching process follows a heavily modified version of the method of Kohl and Nishiizumi (1992). A typical procedure used by many laboratories involves first etching samples in 5 or 1 % HF or HF/HNO<sub>3</sub> on a shaker table or sample roller for multiple periods, followed by etching in 1 % HF or HF/HNO<sub>3</sub> in an ultrasonic bath. Some laboratories

etch samples in an ultrasonic bath without the use of a sample roller or shaker table beforehand. Between etches, samples are rinsed with deionised water (i.e., 18.2 MΩ H<sub>2</sub>O). The number of etches will vary due to factors such as sample lithology, amount of sample material, effectiveness of the froth flotation procedure, in addition to the varying minimum standard procedures for a given laboratory. For in situ <sup>14</sup>C analysis, samples are often etched until they pass a visual test under a binocular microscope and the sample appears to be solely composed of quartz.

## **1.2 Initial Anomalous C-14 Measurements**

Whilst measuring the in situ <sup>14</sup>C concentration of glacial erratic samples as part of multiple projects we observed in situ <sup>14</sup>C measurements that were in excess of geologically plausible maximum concentrations (Fig. 3.1). In each case the maximum concentration for a sample is set by the in situ <sup>14</sup>C saturation concentration for the given sample location, shown in Fig. 3.1. The only way elevated in situ <sup>14</sup>C concentrations could be explained is with an unlikely geomorphic scenario in which the samples were exposed at much higher elevations for a significant period of time before being rapidly transported to their sampling location. This phenomenon was described by Balco et al. (2016) and potentially observed by Balco et al. (2019). Subsequent elevated in situ <sup>14</sup>C concentrations measured from bedrock samples led us to rule out this scenario as the sole source of the observed elevated in situ <sup>14</sup>C concentrations, and we began to explore other explanations.

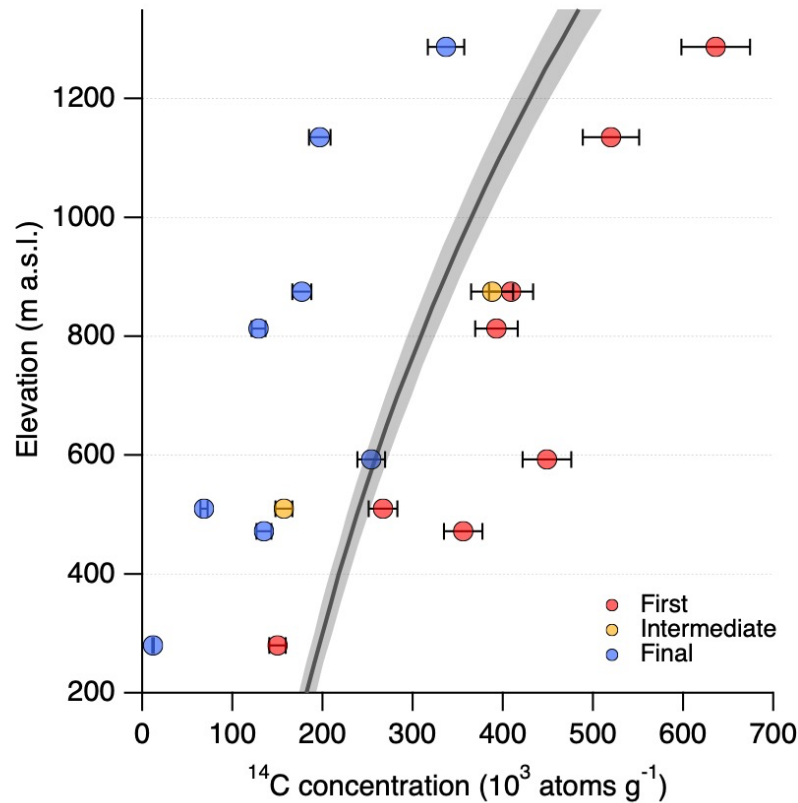


**Figure 3.1:** Elevation versus in situ  $^{14}\text{C}$  concentration of samples that initially yielded anomalously high  $^{14}\text{C}$  concentrations. Measurements at the same elevation are from the same sample. For each sample, the highest in situ  $^{14}\text{C}$  concentration is sourced from the first measurement (red). For the two samples measured three times at 510 and 875 m a.s.l., the intermediate measurement was made following additional etching and yields the intermediate in situ  $^{14}\text{C}$  concentration (yellow). For every sample, the final measurement (blue) was made from quartz isolated from whole rock at Tulane. Error bars reflect a long-term 6 % uncertainty. Some error bars are smaller than their respective data points. Thick grey line and grey shading are the saturation concentration and associated error envelope.

To investigate the cause or causes for the anomalously high in situ  $^{14}\text{C}$  measurements we performed additional measurements of in situ  $^{14}\text{C}$  concentrations of samples displaying elevated concentrations following additional etches in 1 %  $\text{HF}/\text{HNO}_3$  for two 24-hour periods. Further etching resulted in unit yields comparable to the initial measurements and lower, but still anomalously high,  $^{14}\text{C}$  concentrations (Fig. 3.1) (Hillenbrand, unpub.). We note that the quartz from which the anomalously high in situ  $^{14}\text{C}$  concentrations and elevated carbon yields were measured was isolated at other laboratories that use slight variations in their quartz isolation procedures to ours. To investigate further, we measured the in situ  $^{14}\text{C}$  concentration from the same samples but isolated the quartz from whole rock material using our standard procedure (Sect. 1.1). With the exception of one sample, carbon yields were reduced (Fig. 3.2), and for all samples the resulting  $^{14}\text{C}$  concentrations were both lower and geologically plausible (Fig. 3.1).



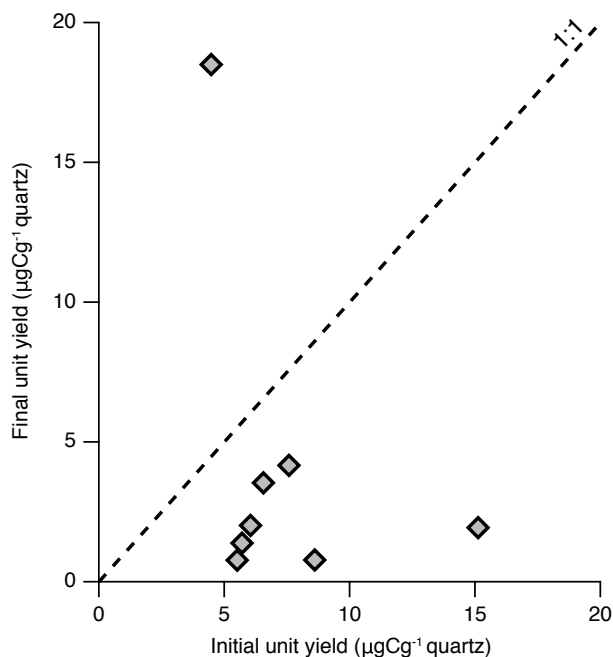


**Figure 3.2:** Initial and final unit yields associated with the same measurements presented in Fig. 3.1. The initial unit yield measurements for each sample were made using quartz isolated at external laboratories, whilst the final unit yield measurements were made using quartz isolated at Tulane using our standard procedure. Error bars are smaller than the data points.

The additional measurements left two potential explanations for the elevated concentrations; unidentified systematic measurement issues or contamination of sample material. Repeat measurements of the quartz interlaboratory comparison material CRONUS-A (Jull et al., 2015; Goehring et al., 2019) and other samples allowed us to rule out systematic measurement issues and conclude that there must be an unidentified source of  $^{14}\text{C}$  contamination. Measurements presented in Figs. 3.1 and 3.2 were made using quartz which was not only visually pure but had initially been isolated for  $^{10}\text{Be}$  measurements. The samples had previously been sent for ICP-MS analysis to test their suitability for  $^{10}\text{Be}$  analysis, confirming that they were comprised of sufficiently pure quartz and thus were ready for  $^{14}\text{C}$  analysis as well. We are therefore confident that the elevated  $^{14}\text{C}$  concentrations were not sourced from other minerals that persisted through quartz isolation. We suspected that the froth flotation procedure was a potential source of  $^{14}\text{C}$  contamination because it involves the introduction of carbon to sample material through the use of three aforementioned compounds. We focused on the long-chain compound laurylamine because eucalyptol is volatile at room temperature and is thus unlikely to persist through sample etching. Acetic acid is predominantly sourced from methanol which is, in turn, largely derived from  $^{14}\text{C}$  dead natural gas, though it can be produced using modern material and therefore may have the potential to contaminate samples with  $^{14}\text{C}$ . However, regardless of the source, acetic acid is a simple

compound that would be relatively easy to break down during etching when compared to laurylamine. There is a complicating factor, in that acetic acid and laurylamine can form complex molecules that behave as a singular species (Karlsson et al., 2001), which may increase the potential for acetic acid to remain on sample material after froth flotation and contribute to potential  $^{14}\text{C}$  contamination. Again, though the predominantly  $^{14}\text{C}$  dead source material minimises potential acetic acid influence. Nonetheless, we focused on laurylamine but acknowledge that it may not be the sole contributor to residual  $^{14}\text{C}$  following froth flotation. The potential of laurylamine to contaminate in situ  $^{14}\text{C}$  concentrations depends on the carbon source of the compound. With a modern source of carbon, laurylamine has the potential to introduce large quantities, relative to the in situ component, of  $^{14}\text{C}$  to samples. The observed changes in  $^{14}\text{C}$  concentration (seemingly dependent on where quartz was isolated and potentially the differing procedures used to isolate quartz) necessitated a systematic study into the potential source and scale of contamination and, if possible, how to efficiently and reliably remove it.

## **2. Systematic Investigation**

We isolated quartz from a whole rock sample using five different methods in order to investigate the cause of contamination. The sample selected for this purpose is Caledonian trondhjemite bedrock (Ragnhildstveit et al., 1998) from Utsira, Norway. The sample contains significant feldspar, mica and quartz, making it ideal for use with froth flotation. The  $^{14}\text{C}$  concentration of the sample is irrelevant for the present study; what is important is the ability to observe any potential contamination from the froth flotation procedure. Prior to froth flotation, the sample was crushed, milled, sieved (to isolate the 250 - 500  $\mu\text{m}$  fraction), and magnetically separated. Following magnetic separation, quartz was isolated for aliquot 1 without froth flotation via four days on a shaker table in 5 % HF/HNO<sub>3</sub> followed by two days in an ultrasonic bath in 1 % HF/HNO<sub>3</sub>. The ultrasonic bath is not heated, but through continued use reaches ca. 40 °C. Aliquot 1 thus forms a baseline against which the other aliquots are compared. Froth flotation was used with aliquots 2 to 5, which were then etched with different acid mixtures (HF and HF/HNO<sub>3</sub>), and varied agitation methods (shaker table and an ultrasonic bath; Table 3.1). Aliquot 2 spent two days on the shaker table in 5 % HF/HNO<sub>3</sub> and two days in the ultrasonic bath in 1 % HF/HNO<sub>3</sub>, which is the minimum duration of etching that all samples receive in our laboratory. Aliquot 3 also spent two days on the shaker table and two days in the ultrasonic bath but was etched in only HF (5 % on the shaker table and 1 % HF in the ultrasonic bath). Aliquot 3 is essentially our standard procedure but

without the inclusion of  $\text{HNO}_3$ . Aliquots 4 and 5 were not etched on the shaker table and both spent two days in the ultrasonic bath, after which they were visually pure, with the former etched in 1 %  $\text{HF}/\text{HNO}_3$ , and the latter etched in 1 %  $\text{HF}$ . Etching samples until quartz is visually pure is a common procedure used to isolate quartz for cosmogenic nuclide analysis. Aliquots 4 and 5 thus represent a feasible minimum duration of etching and were analysed to test if the short duration is sufficient to remove potential contamination. A new acid mixture was used with the samples following a set of rinses with ultrapure 18.2 M $\Omega$  water, such that each aliquot received a new acid mixture once every 24 hours.

We extracted carbon from the five quartz aliquots using the Tulane University Carbon Extraction and Graphitization System (TU-CEGS) following the method of Goehring et al. (2019). Quartz is step-heated in the presence of a lithium metaborate ( $\text{LiBO}_2$ ) flux and a high-purity  $\text{O}_2$  atmosphere, first at 500 °C for 30 minutes, then at 1100 °C for three hours. The former step is to remove any adsorbed atmospheric  $\text{CO}_2$  and combust any carbon derived from sample handling. Released carbon species from the latter 1100 °C step are oxidised to form  $\text{CO}_2$  via secondary hot-quartz-bed oxidation. This is followed by cryogenic collection and purification of the  $\text{CO}_2$ . Sample yields are measured manometrically (Table 3.2), and samples are diluted with  $^{14}\text{C}$ -free  $\text{CO}_2$ . A small aliquot of  $\text{CO}_2$  is collected for  $\delta^{13}\text{C}$  analysis, and the remaining  $\text{CO}_2$  is graphitised using  $\text{H}_2$  reduction over an Fe catalyst (e.g. Southon, 2007). Cathodes containing the graphite were sent to the Woods Hole National Ocean Sciences Accelerator Mass Spectrometry (NOSAMS) to measure  $^{14}\text{C}/^{13}\text{C}$  isotope ratios (Table 3.2) relative to NIST SRM4990c Oxalic Acid II primary standard. The primary standard was produced in the same graphite reactors used for the unknowns, ensuring full internal normalisation. Stable carbon isotope ratios were measured at the UC-Davis Stable Isotope Facility (Table 3.2). Repeat measurements of the CRONUS-A interlaboratory comparison standard (Jull et al., 2015) and other samples using the TU-CEGS show that the reproducibility of in situ  $^{14}\text{C}$  measurements is approximately 6 % (Goehring et al., 2019). We therefore present our  $^{14}\text{C}$  concentrations with a conservative 6 % uncertainty as this exceeds the reported analytical uncertainty for all of our  $^{14}\text{C}$  measurements. Typical total analytical uncertainties are 1.5 to 2.5 %. Blank corrections as a percentage of the total  $^{14}\text{C}$  atoms in each sample range from 13.5 to 17.0 % (Table 3.2).

We also measured the carbon isotope ratio of laurylamine to both identify the presence of a modern carbon source for our laurylamine, and to permit a mass balance calculation to quantify the amount of laurylamine left behind after the frothing and etching process. We extracted carbon from 1.9

mg of laurylamine using the TU-CEGS. We used the process regularly used in our laboratory to extract carbon from oxalic acid. This was appropriate given the similarity of the decomposition temperatures of oxalic acid (~189 °C) and laurylamine (~178 °C). We combusted the sample at 150 °C for ten minutes in ~0.2 MPa (or ~2 atm) of ultra-high purity O<sub>2</sub>, after which the temperature was increased to 500 °C to ensure complete combustion. The resulting CO<sub>2</sub> was then cryogenically collected and purified, followed by catalytic reduction via H<sub>2</sub> to graphite. As with the five quartz aliquots, the cathode was sent to NOSAMS to measure the <sup>14</sup>C/<sup>13</sup>C isotope ratio relative to NIST SRM4990c Oxalic Acid II primary standard.

### **3. Results**

Firstly, the fraction modern (Fm) value of laurylamine is  $1.0338 \pm 0.0020$ , indicative of a modern carbon source.

Results for the five aliquots are shown in Table 3.2, with the unit yields and <sup>14</sup>C concentrations also presented in Fig. 3.3. The total carbon yields for aliquots 1 and 2 are lower than those of aliquots 3 to 5. Aliquots 1 and 2 were isolated without froth flotation and with the TUCNL standard procedure (including froth flotation), respectively. Because slightly differing masses of quartz were used for in situ <sup>14</sup>C analysis, a direct comparison can be made using the carbon unit yields (Fig. 3.3 and Table 3.2). The unit yield for aliquots 1 and 2 are the same within 1 $\sigma$  uncertainty. We observe elevated unit yields for aliquots 3 to 5 relative to those of aliquots 1 and 2.

As with the unit yields, the <sup>14</sup>C concentration of aliquots 1 and 2 are the same within uncertainties and are distinguishable from the unit yields of aliquots 3 to 5 when using the conservative 6 % uncertainty (Fig. 3.3). We observe elevated <sup>14</sup>C concentrations for aliquots 3 to 5 relative to those of aliquots 1 and 2, with a particularly high <sup>14</sup>C concentration for aliquot 5 (Fig. 3.3B). Figure 3.3 shows that the higher unit yields correspond with higher measured <sup>14</sup>C concentrations. With aliquot 5, a small increase in unit yield results in a disproportionately high <sup>14</sup>C concentration that dwarfs those of aliquots 1 to 4.

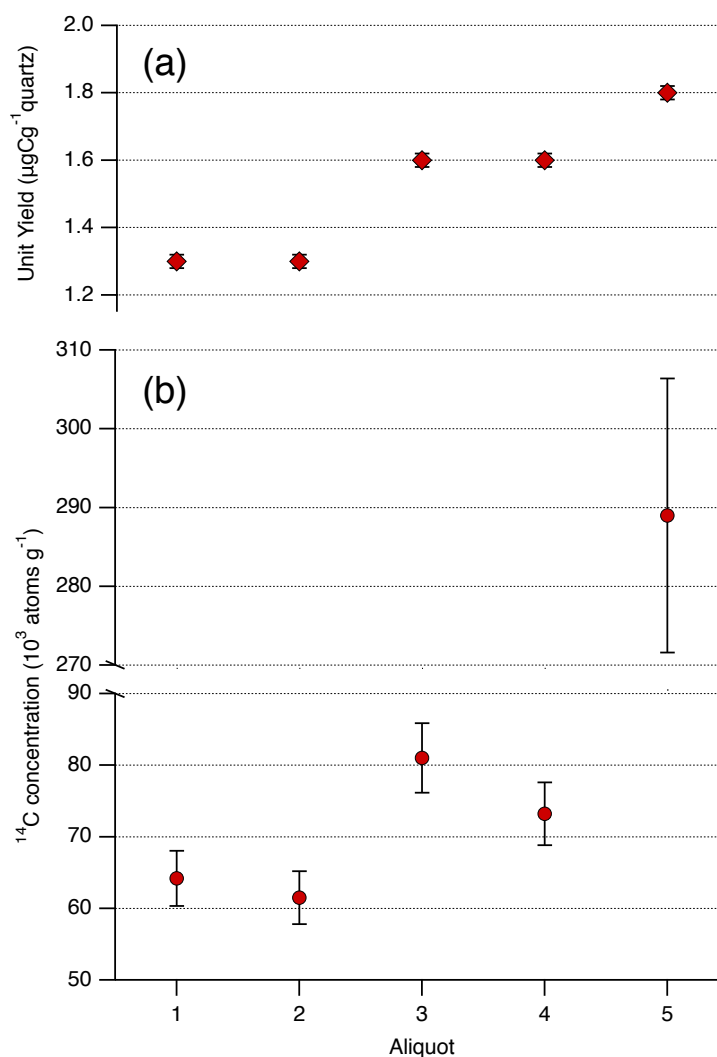


**Figure 3.3:** A: Unit yield for the five quartz separates. Aliquot numbers refer to those in Table 3.1. B: C-14 concentration for the five quartz aliquots; error bars reflect a long-term 6 % uncertainty. B has a split y-axis to present both the differences in <sup>14</sup>C concentrations between aliquots 1 to 4 and the difference between aliquot 5 and aliquots 1 to 4. See Table 3.1 for the different quartz isolation procedures used. For reference, all aliquots other than Aliquot 1 were subject to froth flotation. Aliquot 2 was processed using the TUCNL standard procedure.

#### **4. Discussion**

The modern carbon source, identified with the measured Fm of our laurylamine, shows that laurylamine is not <sup>14</sup>C dead and thus has the potential to contaminate samples with respect to <sup>14</sup>C. We did not measure the Fm of acetic acid or eucalyptol due to the rationale described above (Sect. 1.2) and thus we cannot rule out their potential to contaminate samples with <sup>14</sup>C. However, the modern carbon source of laurylamine confirms that the froth flotation procedure, regardless of the contributing compound, introduces <sup>14</sup>C to sample material. The measured <sup>14</sup>C/<sup>12</sup>C ratio for laurylamine is  $1.19 \times 10^{-12}$ . This means that, for example, 20 µg contains  $\sim 9.3 \times 10^5$  atoms of <sup>14</sup>C. The elevated carbon yields and

unit yields of aliquots 3 to 5 relative to those of aliquots 1 and 2 may indicate that the former are contaminated with total carbon and, of particular importance,  $^{14}\text{C}$ . However, elevated carbon yields and unit yields are not sufficient evidence alone to indicate contamination because the maximum difference in carbon yields (2.2  $\mu\text{g}$ , Table 3.2) is within the range of carbon yields of process blanks in our laboratory (Goehring et al., 2019). Therefore, the differing yields may simply be the result of varying blank magnitude and not due to contamination from froth flotation. However, the elevated  $^{14}\text{C}$  concentrations of aliquots 3 to 5 relative to those of aliquots 1 and 2 do indicate that the former are contaminated with  $^{14}\text{C}$ . The difference in  $^{14}\text{C}$  concentration between aliquots 1 and 2 and those of aliquots 3 to 5 is much greater than the  $^{14}\text{C}$  content of process blanks in our laboratory (Goehring et al., 2019), therefore the difference cannot be explained by varying blank magnitudes alone and is indicative of  $^{14}\text{C}$  contamination. The elevated unit yields may therefore also be due to carbon contamination. The unit yields and  $^{14}\text{C}$  concentrations of aliquots 1 and 2 are indistinguishable from one another, which indicates that our standard procedure for quartz isolation (Aliquot 2) removes carbon introduced by laurylamine. Differing quartz isolation procedures used at other laboratories may therefore explain why quartz isolated from the same samples at Tulane and elsewhere produced vastly different  $^{14}\text{C}$  concentrations (Sect. 1.2).

We use the excess measured  $^{14}\text{C}$  atoms in aliquots 3 to 5 (the total  $^{14}\text{C}$  atoms for each aliquot in excess of the average of those of aliquots 1 and 2) with the measured  $^{14}\text{C}/^{12}\text{C}$  ratio for laurylamine to calculate the corresponding mass of residual carbon and laurylamine, per gram of quartz, that was collected with the in situ  $^{14}\text{C}$  component. We assume aliquots 1 and 2 were not contaminated with  $^{14}\text{C}$  and thus excess  $^{14}\text{C}$  is sourced solely from laurylamine, though it could be sourced from eucalyptol or acetic acid if they were to persist through sample etching. To calculate the mass of contaminant ( $M_{contam}$ ) carbon or laurylamine we follow

$$M_{contam} = {}^{14}\text{C}_{excess} \left( \frac{{}^{14}\text{C}}{{}^{12}\text{C}} \right)_{LA} \frac{M}{A}$$

where  ${}^{14}\text{C}_{excess}$  is the measured number of excess  $^{14}\text{C}$  atoms,  $({}^{14}\text{C}/^{12}\text{C})_{LA}$  is the measured ratio for laurylamine ( $1.19 \times 10^{-12}$ ),  $M$  is the molar mass of carbon or molecular mass of laurylamine, and  $A$  Avogadro's Number. This calculation is an estimate as it does not take into account the ca. 1.1 %  $^{13}\text{C}$  in laurylamine. The excess  $^{14}\text{C}$  accounts for an estimated 0.06, 0.03 and 0.74  $\mu\text{g}$  carbon  $\text{g}^{-1}$  quartz, and 0.08,

0.04, 0.95  $\mu\text{g g}^{-1}$  of laurylamine for aliquots 3, 4 and 5, respectively (Table 3.2). We can use the same method for the samples that produced the initial anomalous measurements shown in Fig. 3.1. To do so we assume that the final measurement made for each sample is free from laurylamine contamination. For the samples presented in Fig. 3.1, the excess  $^{14}\text{C}$  concentrations range from  $1.38 \times 10^5$  to  $3.23 \times 10^5$  at  $\text{g}^{-1}$ . The associated residual carbon ranges from 2.32 to 5.42  $\mu\text{g g}^{-1}$ , and the residual laurylamine ranges from 2.98 to 6.96  $\mu\text{g g}^{-1}$ , both per gram of quartz. We speculate that the latter residual carbon and laurylamine estimates, an order of magnitude greater than those presented in this study, may be an artefact of the differing froth flotation and etching procedures used at the laboratories at which the quartz was isolated. Contributing factors could include, but are not limited to, a greater amount of laurylamine used in the quartz separation process, the concentration at which the laurylamine comes into contact with sample material (dilute or undilute), the acids used in the etching procedure, and the duration of acid etching. As noted in Sect. 1.2, we are confident that the elevated  $^{14}\text{C}$  concentrations were not sourced from other minerals that persisted through quartz isolation because the quartz separates were previously analysed by ICP-MS to confirm their suitability for  $^{10}\text{Be}$  analysis. Though fluid inclusions may contribute to elevated carbon yields, they would presumably be devoid of  $^{14}\text{C}$  and thus could not explain the anomalous  $^{14}\text{C}$  concentrations. Production of  $^{14}\text{C}$  on  $^{14}\text{N}$  in fluid inclusions through thermal neutron capture is possible, however, the presumably low abundance of  $^{14}\text{N}$  means that this production mechanism is unlikely to contribute significantly to  $^{14}\text{C}$  concentrations when compared to the spallation component (Lal and Jull, 1998).

The elevated carbon yields and  $^{14}\text{C}$  concentrations of aliquots 3 to 5 relative to those of aliquots 1 and 2 suggest two things. Firstly, it is apparent that  $\text{HNO}_3$  is needed to remove laurylamine-derived carbon, both total carbon and  $^{14}\text{C}$ , contamination from quartz. The importance of  $\text{HNO}_3$  is demonstrated by the higher unit yields and  $^{14}\text{C}$  concentrations of aliquots that were etched with only HF compared to aliquots that had the same quartz isolation method and duration of etching but were etched with a combination of HF and  $\text{HNO}_3$  (aliquot 3 vs 2 and aliquot 5 vs 4). We hypothesise that, as an oxidiser,  $\text{HNO}_3$  is key in the decomposition of laurylamine. Before carbon is extracted from aliquots, quartz is leached in 50 % v/v  $\text{HNO}_3$  for 30 minutes in an unheated ultrasonic bath (Lifton et al., 2001; Goehring et al., 2019). This is important to note because it is apparent that this additional leach with strong  $\text{HNO}_3$  is not sufficient alone to remove contaminant  $^{14}\text{C}$  and highlights the importance of HF as well as  $\text{HNO}_3$  in the etching procedure and their role in the removal of contamination. We hypothesise that dissolution

of quartz using HF helps to release contamination stored within microfractures of quartz grains (elaborated further below). Secondly, two days in an ultrasonic bath with 1 % acid mixture, regardless of whether HF or HF/HNO<sub>3</sub> is used for etching, appears to be insufficient to remove froth flotation-derived contaminants. Aliquots 4 and 5, which were not etched on the shaker table and spent a total of two days etching in an ultrasonic bath, both appeared visually pure and thus looked ready for in situ <sup>14</sup>C analysis without the context of potential froth flotation-derived contamination. It is possible that that contamination would have been removed if aliquots 4 and 5 were etched with 5 % rather than 1 % HF/HNO<sub>3</sub>. However, the purpose of aliquots 4 and 5 was to test if the minimum feasible duration of etching and strength of acid used by laboratories to isolate quartz would be sufficient to remove potential contamination from froth flotation. Evidently, a standard procedure to etch samples until they are visually pure is not necessarily sufficient when froth flotation has been used. If a laboratory has only a shaker table or an ultrasonic bath, we would speculate that a minimum of four 24-hour periods in 5 % HF/HNO<sub>3</sub> would be sufficient to remove froth flotation-derived contamination.

The observation that the <sup>14</sup>C concentration increase from froth flotation is of the same order of magnitude as that of typical in situ <sup>14</sup>C measurements is of great concern and highlights the need for a sufficiently thorough minimum procedure to eliminate contamination from the quartz isolation process. Carbon introduced by froth flotation is evidently persisting through the 500 °C step heat, the first stage of extracting <sup>14</sup>C from quartz with the TU-CEGS and in other in situ <sup>14</sup>C laboratories (e.g., Hippe et al., 2013; Lifton et al., 2015; Goehring et al., 2019; Lamp et al., 2019). The 500 °C bake was previously shown to remove contaminant <sup>14</sup>C (Lifton et al., 2001), though this was presumably from sample handling and the atmosphere and pre-dates the implementation of froth flotation for quartz separation. We suspect that the observed contamination is sourced from laurylamine or other froth flotation-derived contaminants residing within microfractures of quartz grains, which may explain why the contamination is able to persist through the 500 °C bake and possibly accounts for differences in the degree of contamination between previously analysed samples and those as part of this study due to differences in the quartz grain characteristics. The potential quantity of laurylamine or other contaminants able to reside in the microfractures of a particular sample will presumably vary with the lithology and geologic history of the sample, as well as the methods of sample preparation. The natural abundance of microfractures in a sample prior to sample collection will vary and microfractures may also be introduced during sample collection, crushing and milling. Figures 3.4 and 3.5 show evidence of microfractures on the surface of



quartz grains from all aliquots. In addition, Fig. 3.4 shows a quartz grain from an unetched aliquot that was sourced from the same whole rock sample as the five aliquots. Anecdotally, whilst using the SEM we observed microfractures that seemed to be opened up to a greater extent in aliquots 1 and 2, which received the longest duration of etching, compared to aliquots 3 to 5. Note the high surface roughness of the unetched sample (Fig. 3.4a and b) and the relative smoothness of the grains in all aliquots (Figs. 3.4 and 3.5), a result of the partial dissolution by HF of quartz grains which will have presumably removed some microfractures entirely. We observe that further etching, both in our initial measurements (Sect. 1.2) and when comparing aliquots 2 and 3 with aliquots 4 and 5, lowers carbon yields and  $^{14}\text{C}$  concentrations. The longer duration in acid may indicate that the HF is opening up microfractures and allowing contamination to be more thoroughly removed, highlighting the importance of HF in the removal of contamination, though this would be difficult to test, and an extensive systematic study would be required to make conclusions with any statistical significance. Whilst the presence of microfractures does not confirm our hypothesis, Figs. 3.3 and 3.4 do show that there are abundant microfractures and surface features for contaminants to potentially reside in following froth flotation.

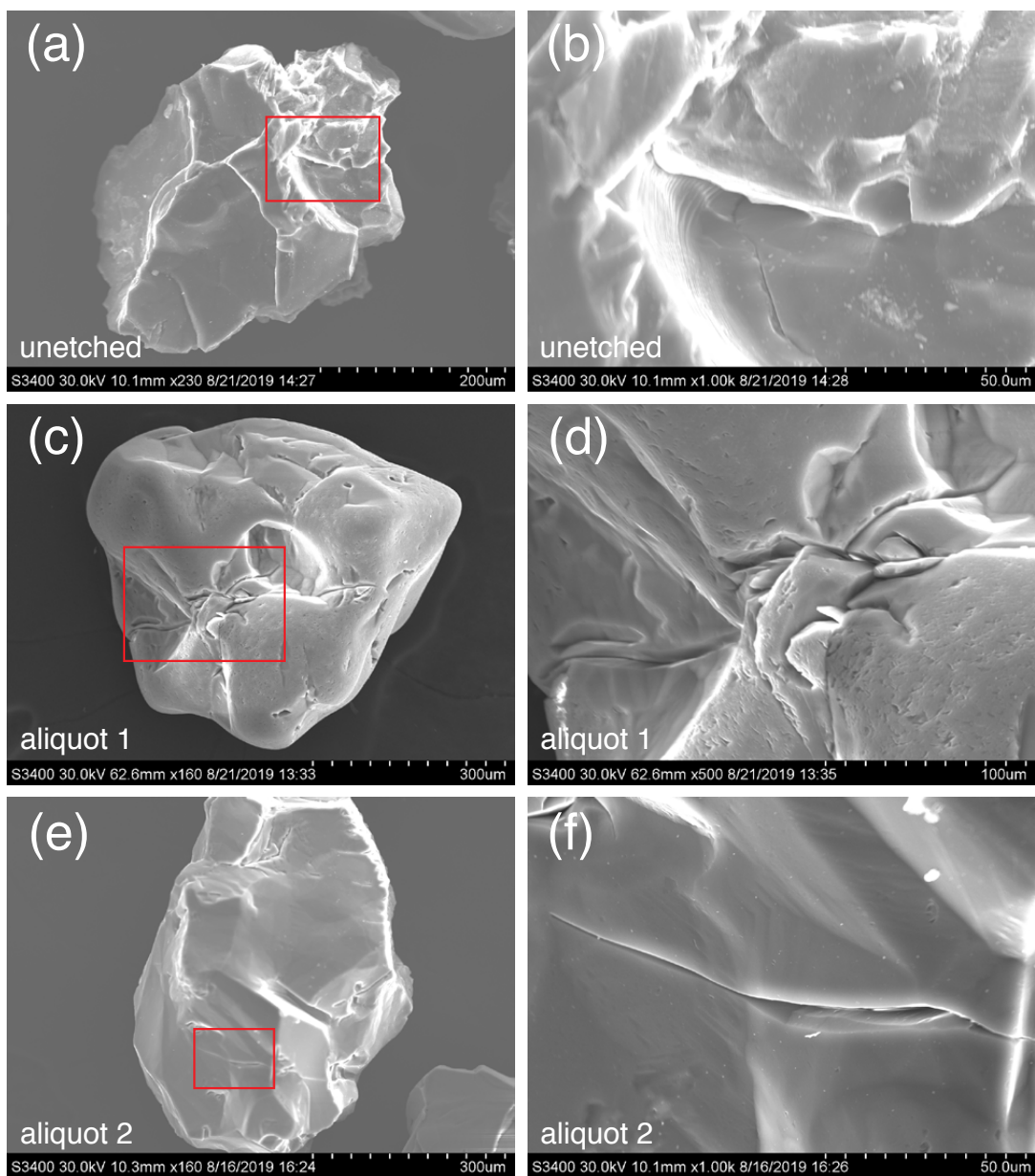


**Figure 3.4:** SEM images of quartz grains of an unetched sample and aliquots 1 and 2. Red boxes on the left show the location of the adjacent image to the right. The unetched sample is sourced from the same whole rock sample as the five aliquots and was crushed, milled, sieved, rinsed and magnetically separated. Note the conchoidal fracture in B.

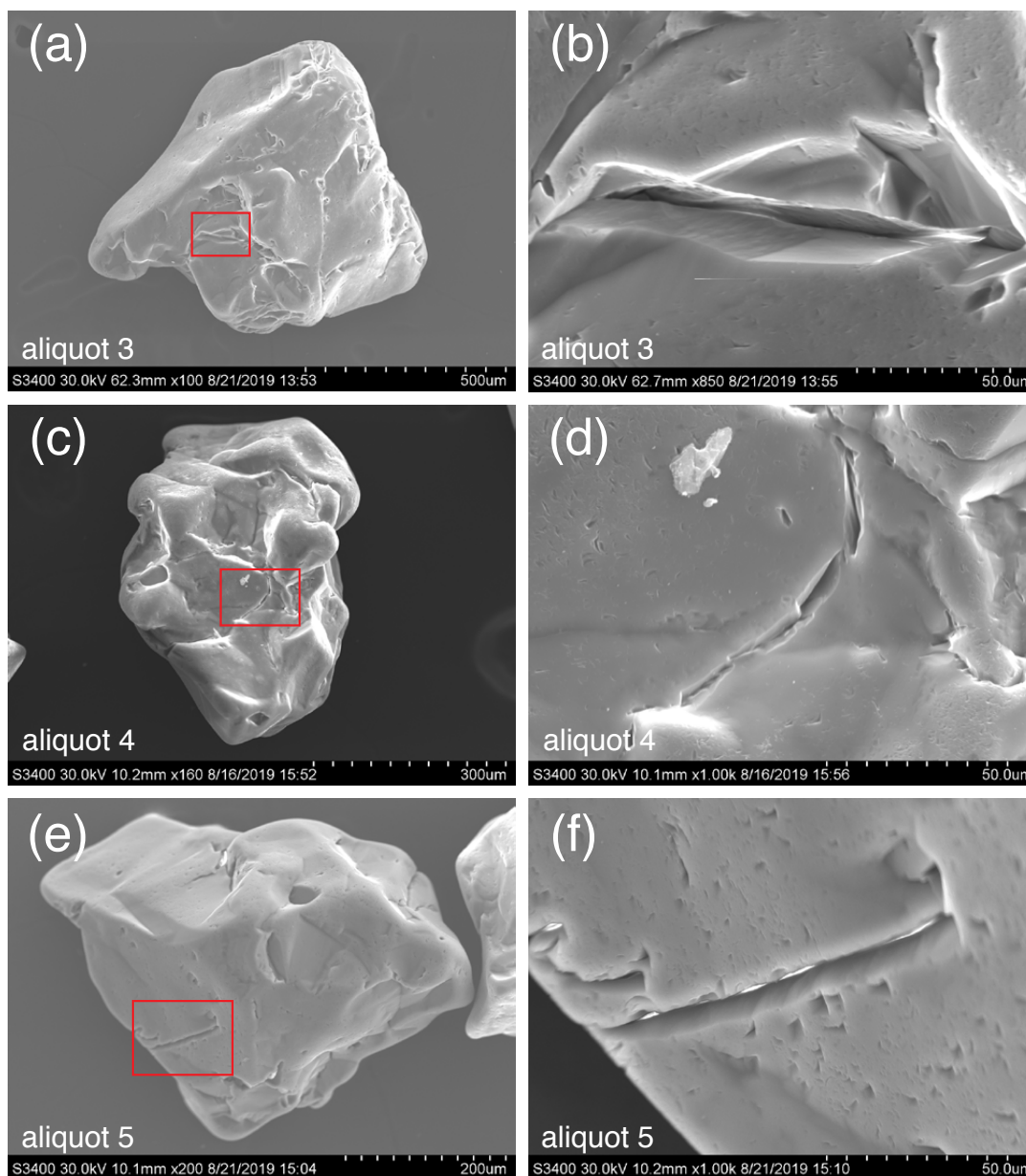


**Figure 3.5:** SEM images of quartz grains of aliquots 3 to 5.

## **5. Conclusion**

We found that laurylamine is manufactured with a modern carbon source and thus introduces modern  $^{14}\text{C}$  to sample material during froth flotation. We have shown through a systematic study that contaminant  $^{14}\text{C}$  from froth flotation persists through sample etching and is collected with in situ  $^{14}\text{C}$  if etching is not rigorous enough. Nitric acid, combined with hydrofluoric acid, is required to effectively remove contaminant  $^{14}\text{C}$ , which is shown by the elevated  $^{14}\text{C}$  concentrations of quartz separates isolated without nitric acid relative to those extracted with nitric acid. We have outlined a reliable method for

ensuring no contaminant  $^{14}\text{C}$  from froth flotation remains with quartz following etching. In short, two 24-hour periods on a shaker table with 5 % HF/HNO<sub>3</sub>, followed by two 24-hour periods in an ultrasonic bath in 1 % HF/HNO<sub>3</sub>, is sufficient to produce in situ  $^{14}\text{C}$  concentrations indistinguishable from a sample for which quartz was isolated without froth flotation. Ultimately, froth flotation should be used with caution and the sample etching procedure outlined above should be used at an absolute minimum.

### **Acknowledgements**

KN and BG would like to acknowledge NOSAMS for their outstanding measurements. We would also like to acknowledge the fruitful discussions with Trevor Hillenbrand, John Stone, and Greg Balco that greatly helped to develop the study. Sample material was collected with the help of Jan Mangerud and John-Inge Svendsen. We would like to thank Jibao He for training and assistance in the use of the SEM in the CIF Microscopy Laboratory at Tulane University. We would also like to thank Anthony Jull and an anonymous reviewer for their reviews that helped to improve the manuscript.

## **References**

- Balco, G., Todd, C., Goehring, B.M., Moening-Swanson, I., Nichols, K.: Glacial geology and cosmogenic-nuclide exposure ages from the Tucker Glacier - Whitehall Glacier confluence, northern Victoria Land, Antarctica, *Am. J. Sci.*, 319(April), 255–286, doi:10.2475/04.2019.01, 2019.
- Balco, G., Todd, C., Huybers, K., Campbell, S., Vermeulen, M., Hegland, M., Goehring, B. M. and Hillebrand, T. R.: Cosmogenic-nuclide exposure ages from the Pensacola Mountains adjacent to the foundation ice stream, Antarctica, *Am. J. Sci.*, 316(6), 542–577, doi:10.2475/06.2016.02, 2016.
- Goehring, B. M., Wilson, J. and Nichols, K.: A fully automated system for the extraction of in situ cosmogenic carbon-14 in the Tulane University cosmogenic nuclide laboratory, *Nucl. Instruments Methods Phys. Res. Sect. B Beam Interact. with Mater. Atoms*, 455, 284–292, doi:10.1016/j.nimb.2019.02.006, 2019.
- Herber, L. J.: Separation of feldspar from quartz by flotation, *Am. Mineral.*, 54, 1212–1215, doi:10.4144/rpsj1954.25.192, 1969.
- Hippe, K., Kober, F., Wacker, L., Fahrni, S. M., Ivy-Ochs, S., Akçar, N., Schlüchter, C. and Wieler, R.: An update on in situ cosmogenic <sup>14</sup>C analysis at ETH Zürich, *Nucl. Instruments Methods Phys. Res. Sect. B Beam Interact. with Mater. Atoms*, 294, 81–86, doi:10.1016/j.nimb.2012.06.020, 2013.
- Jull, A. J. T., Scott, E. M. and Bierman, P.: The CRONUS-Earth inter-comparison for ' cosmogenic isotope analysis, *Quat. Geochronol.*, 26(1), 3–10, doi:10.1016/j.quageo.2013.09.003, 2015.

- Karlsson, S., Friman, R., Björkvist, M., Lindström, B. and Backlund, S.: Phase Behavior and Characterization of the System Acetic Acid-Dodecylamine-Water, *Langmuir*, 17(12), 3573–3578, doi:10.1021/la001594m, 2001.
- Kohl, C. P. and Nishiizumi, K.: Chemical isolation of quartz for measurement of in-situ-produced cosmogenic nuclides, *Geochim. Cosmochim. Acta*, 56(9), 3583–3587, doi:10.1016/0016-7037(92)90401-4, 1992.
- Lal, D. and Jull, A. J. .: In-situ cosmogenic  $^{14}\text{C}$ : Production and examples of its unique applications in studies of terrestrial and extraterrestrial processes, *Radiocarbon*, 43(2B), 731–742, 1998.
- Lamp, J. L., Young, N. E., Koffman, T., Schimmelpfennig, I., Tuna, T., Bard, E. and Schaefer, J. M.: Update on the cosmogenic in situ  $^{14}\text{C}$  laboratory at the Lamont-Doherty Earth Observatory, *Nucl. Instruments Methods Phys. Res. Sect. B Beam Interact. with Mater. Atoms*, 465, 157–162, doi:10.1016/j.nimb.2019.05.064, 2019.
- Lifton, N., Goehring, B., Wilson, J., Kubley, T. and Caffee, M.: Progress in automated extraction and purification of in situ  $^{14}\text{C}$  from quartz: Results from the Purdue in situ  $^{14}\text{C}$  laboratory, *Nucl. Instruments Methods Phys. Res. Sect. B Beam Interact. with Mater. Atoms*, 361, 381–386, doi:10.1016/j.nimb.2015.03.028, 2015.
- Lifton, N. A., Jull, A. J. T. and Quade, J.: A new extraction technique and production rate estimate for in situ cosmogenic  $^{14}\text{C}$  in quartz, *Geochim. Cosmochim. Acta*, 65(12), 1953–1969, doi:10.1016/S0016-7037(01)00566-X, 2001.
- Ragnhildstveit, E., Naterstad, J., Jorde, K., Egeland, B.: *Beskrivelse Til Geologisk Kart Over Norge - 1: 250.000 Haugesund, Norges Geol. Undersøkelse.*, 1998.
- Southon, J.: Graphite reactor memory-Where is it from and how to minimize it?, *Nucl. Instruments Methods Phys. Res. Sect. B Beam Interact. with Mater. Atoms*, 259(1), 288–292, doi:10.1016/j.nimb.2007.01.251, 2007.

**Tables**

Sample ID	Aliquot Number	Days on shaker table	Days in ultrasonic bath	Total	Notes
16-UT-004-QUA-NOFROTH	1	4	2	6	No froth flotation, etched with HF/HNO <sub>3</sub>
16-UT-004-QUA-NORM	2	2	2	4	Froth flotation, etched with HF/HNO <sub>3</sub> in shaker table and ultrasonic bath
16-UT-004-QUA-HFONLY	3	2	2	4	Froth flotation, etched with HF in shaker table and ultrasonic bath
16-UT-004-QUA-NOSTABLE1	4	0	2	2	Froth flotation, etched with HF/HNO <sub>3</sub> in ultrasonic bath
16-UT-004-QUA-NOSTABLE12	5	0	2	2	Froth flotation, etched with HF in ultrasonic bath

**Table 3. 1:** Aliquot information and quartz isolation procedures. Whilst on the shaker table, samples were etched in 5 % HF/HNO<sub>3</sub> or 5 % HF. Whilst in the ultrasonic bath, samples were etched in 1 % HF/HNO<sub>3</sub> or 1 % HF.

Aliquot Number	TUCNL	AMS Lab	AMS ID	Quartz weight (g)	C yield ( $\mu\text{g}$ )	$\pm 1\sigma$ ( $\mu\text{g}$ )	Unit Yield ( $\mu\text{g g}^{-1}$ )	Diluted Gas Mass ( $\mu\text{g}$ )	$\pm 1\sigma$ ( $\mu\text{g}$ )	$^{14}\text{C}/^{13}\text{C}$	$\pm 1\sigma$	$\delta^{13}\text{C}$ ( $\text{‰}$ )	$\pm 1\sigma$ ( $\text{‰}$ )
1	309	NOSAMS	OS-141782	5.196	6.9	0.1	1.3	85.5	1.1	8.47E-12	8.56E-14	-4.98	0.5
2	307	NOSAMS	OS-141784	5.122	6.5	0.1	1.3	100.3	1.3	6.88E-12	8.23E-14	-4.54	0.5
3	308	NOSAMS	OS-141785	5.104	8.3	0.1	1.6	88.0	1.1	9.88E-12	9.58E-14	-5.20	0.5
4	310	NOSAMS	OS-141786	5.134	8.4	0.1	1.6	83.7	1.1	9.57E-12	9.27E-14	-5.13	0.5
5	311	NOSAMS	OS-141788	5.080	9.1	0.1	1.8	76.7	1.0	3.64E-11	1.90E-13	-5.78	0.5
$^{14}\text{C}/\text{C total}$	$\pm 1\sigma$	Total $^{14}\text{C}$ atoms blank corrected	$\pm 1\sigma$ (at)	$^{14}\text{C conc.}$ (at.g $^{-1}$ )	$\pm 1\sigma$ (at.g $^{-1}$ )	$\pm 6\%$ (at.g $^{-1}$ )	Effective blank (at)	$\pm 1\sigma$ (at)	Effective Blank as % of total $^{14}\text{C}$ At Sample	Residual C ( $\mu\text{g g}^{-1}$ )	Residual $\text{C}_{12}\text{H}_{27}\text{N}$ ( $\mu\text{g g}^{-1}$ )		
9.29E-14	9.39E-16	3.34E+05	9.439E+03	6.42E+04	1.64E+03	3.85E+03	6.47E+04	6.85E+03	16.25	-	-		
7.55E-14	9.04E-16	3.15E+05	9.548E+03	6.15E+04	1.64E+03	3.69E+03	6.47E+04	6.85E+03	17.04	-	-		
1.08E-13	1.05E-15	4.13E+05	1.029E+04	8.10E+04	1.80E+03	4.86E+03	6.47E+04	6.85E+03	13.53	0.06	0.08		
1.05E-13	1.02E-15	3.76E+05	9.845E+03	7.32E+04	1.73E+03	4.39E+03	6.47E+04	6.85E+03	16.25	0.03	0.04		
3.99E-13	2.08E-15	1.47E+06	2.230E+04	2.89E+05	4.10E+03	1.74E+04	6.47E+04	6.85E+03	14.69	0.74	0.95		



**Table 3. 2:** In situ  $^{14}\text{C}$  analytical data. Aliquot number is described in the text. See Table 3.1 for the different quartz isolation procedures used for each aliquot. TUCNL is a unique sample identifier for each sample analysed at the Tulane University Cosmogenic Nuclide Laboratory. C yield is the carbon yield prior to dilution. Unit yield is the carbon yield divided by the quartz mass. Total  $^{14}\text{C}$  blank corrected is the total number of  $^{14}\text{C}$  atoms corrected using the effective blank. Effective blank is representative of the blank during the running of the samples presented. See Sect. 2 for rationale behind the use of the 6 % uncertainty for the  $^{14}\text{C}$  concentrations. We also include  $1\sigma$  uncertainty for the  $^{14}\text{C}$  concentrations for completeness. The mass of residual carbon and laurylamine for aliquots 3 to 5 are calculated using the  $^{14}\text{C}/^{12}\text{C}$  ratio of laurylamine as measured (see Sect. 4)

**Chapter 4: An evaluation of ice sheet model-derived ice histories using cosmogenic nuclide measurements from the Weddell Sea Embayment sector of Antarctica**

Keir A. Nichols, Brent M. Goehring, Greg Balco

To be submitted to *The Cryosphere, Earth and Planetary Science Letters*, or *Geophysical Research Letters*

## **Abstract**

We use a compilation of terrestrial cosmogenic nuclide measurements from the Weddell Sea Embayment to evaluate the results of numerical ice sheet modelling studies simulating deglaciation of the Antarctic Ice Sheet. Before simulating the response of an ice sheet to future changes in climate, models must be tested against palaeo data to evaluate their ability to reproduce past known configurations of an ice sheet. A number of recent surface exposure dating studies in the Weddell Sea Embayment contribute to an improved understanding of the LGM configuration and pattern of deglaciation in this region. Our aim is to inform future modelling efforts in the WSE by identifying model behaviour that is inconsistent and not inconsistent with exposure age constraints in terms of both predicted ice thickness and the timing of changes in ice thickness. We locate regions that are best and least well modelled with respect to geologic evidence for the LGM configuration and subsequent thinning. The majority of cosmogenic nuclide constraints in the embayment provide minimum constraints, thus we find that models prescribing relatively thick LGM ice are most often not inconsistent with geologic constraints. With respect to how well numerical ice sheet models predict the timing of changes in ice thickness indicated by exposure ages, we find that the timing and rate of the majority of post-LGM ice thinning predicted by ice sheet models is often both premature and more rapid than indicated by exposure ages.

## **1. Introduction**

Simulating the response of the Antarctic Ice Sheet to future climate perturbations is necessary to quantify future sea-level projections and inform policy makers. The future contribution of the Antarctic Ice Sheet to sea level rise is the largest uncertainty in projections of future global sea level (Levermann et al., 2020). Numerical ice sheet models have been used for decades to study the Antarctic Ice Sheet (e.g. Huybrechts (1990)); however, before simulating the response of an ice sheet to future climate change, the performance of the model needs to be validated against past and present ice sheet configurations and dynamics. There is a wealth of information with respect to ice sheet behaviour and extent for the Last Glacial Maximum (LGM, ca. 26 to 15 ka; Peltier and Fairbanks, 2006). Consequently, the LGM configuration of the Antarctic Ice Sheet is often used to calibrate ice sheet models. In a review of the reconstruction of palaeo-ice sheets, Stokes et al. (2015) state that “our confidence in future

predictions of ice sheet mass balance and sea level rise will benefit from numerical ice sheet models that have been rigorously tested against palaeo-data.” A number of terrestrial cosmogenic nuclide exposure dating studies in the Weddell Sea Embayment (WSE) sector of Antarctica published over the last decade have filled large spatial gaps in terms of both the LGM configuration and pattern of deglaciation of this sector of the ice sheet (e.g. Balco et al., 2016; Hein et al., 2016; Bentley et al., 2017; Johnson et al., 2019). Thus, we contribute toward the testing of ice sheet model outputs by using the recently-updated dataset of post-LGM terrestrial cosmogenic nuclide exposure ages from the Weddell Sea Embayment to evaluate the results of multiple ice sheet models.

In this study, we use post-LGM  $^{10}\text{Be}$  and in situ  $^{14}\text{C}$  exposure ages from the WSE to evaluate the results of six Antarctic Ice Sheet numerical ice sheet modelling studies, which use a total of three different numerical ice sheet models and one ice loading history inversion. The numerical ice sheet model outputs are sourced from Whitehouse et al. (2012), Golledge et al. (2014), Pollard et al. (2016; 2017), Kingslake et al. (2018), and Tigchelaar et al. (2018), in addition to the Antarctic component of the global ice loading history of Argus et al. (2014). We describe recent advances in our knowledge of the deglacial history of the WSE before outlining the use of cosmogenic nuclide measurements and their role as geologic constraints for numerical ice sheet models. Our evaluation focusses on model predicted total ice thickness change since the LGM and the timing of ice thinning. We find that many model outputs predict ice thickness change on a scale not inconsistent with geologic constraints in many locations, but the timing of ice thinning often leads or lags the actual ice thickness change indicated by exposure ages. We also find that the LGM-to-present ice thickness change at some sites is systematically underpredicted and postulate as to why this is the case. Finally, we apply a method through which model outputs can be evaluated using individual measurements of the short-lived cosmogenic nuclide, in situ  $^{14}\text{C}$ .

### **1.1 Deglaciation in the Weddell Sea Embayment**

The WSE was occupied by laterally and vertically expanded ice at the LGM (Bentley and Anderson, 1998). Marine geological and geophysical evidence shows that grounded Weddell Sea Embayment ice advanced to the shelf edge during the last glacial cycle, with the grounding line located either across the entire width of the embayment, or at least between the deep Ronne and Filchner troughs in the west and east of the embayment, respectively (Hillenbrand et al., 2012; 2014; Larter et al., 2012; Arndt et al.,

2017). Until recently, terrestrial evidence from long-lived cosmogenic nuclides indicated that the vertical extent of ice in the WSE at the LGM was spatially variable. Exposure ages from the Ellsworth Mountains show that LGM ice was at least ca. 1.1 km thicker than present (Fig. 4.1; Fogwill et al., 2014), and ice was at least 300 to 500 m thicker at other locations around the embayment (Fig. 4.1; Bentley et al., 2006; Balco et al., 2016; Hein et al., 2016; Bentley et al., 2017). Conversely, studies in the Shackleton Range (Hein et al., 2011; 2014) and the Schmidt Hills in the Pensacola Mountains (Balco et al., 2016; Bentley et al., 2017) suggest little to no ice thickness change at the LGM relative to the present. The spatially variable LGM thickness estimates are difficult to reconcile with evidence for significant thickening at some but not all locations, and simultaneously with marine evidence for greatly expanded lateral ice (Hillenbrand et al., 2014; Whitehouse et al., 2017).

More recently, measurements of the short-lived cosmogenic nuclide *in situ*  $^{14}\text{C}$  show that ice was indeed thicker than present in the Shackleton Range, Schmidt Hills, and also on the Lassiter Coast on the southern Antarctic Peninsula. Post-LGM *in situ*  $^{14}\text{C}$  ages show that ice was 300 to 655 m thicker than present in the Shackleton Range, at least 800 m thicker than present in the Schmidt Hills (Nichols et al., 2019), and at least 385 m thicker than present at the Lassiter Coast (Johnson et al., 2019) (Fig. 4.1). New exposure age constraints have also been added for the Pirrit Hills, close to the Ellsworth Mountains, and the Whitmore Mountains at the West Antarctic Ice Sheet (WAIS) Divide (Fig. 4.1; Spector et al., 2019). There is now sufficient paleo ice thickness constraints that we have a comprehensive understanding of the extent of ice in the WSE during the LGM. We are thus motivated to undertake an evaluation of past ice sheet model outputs to explore how well deglaciation in the WSE has been modelled in the past.

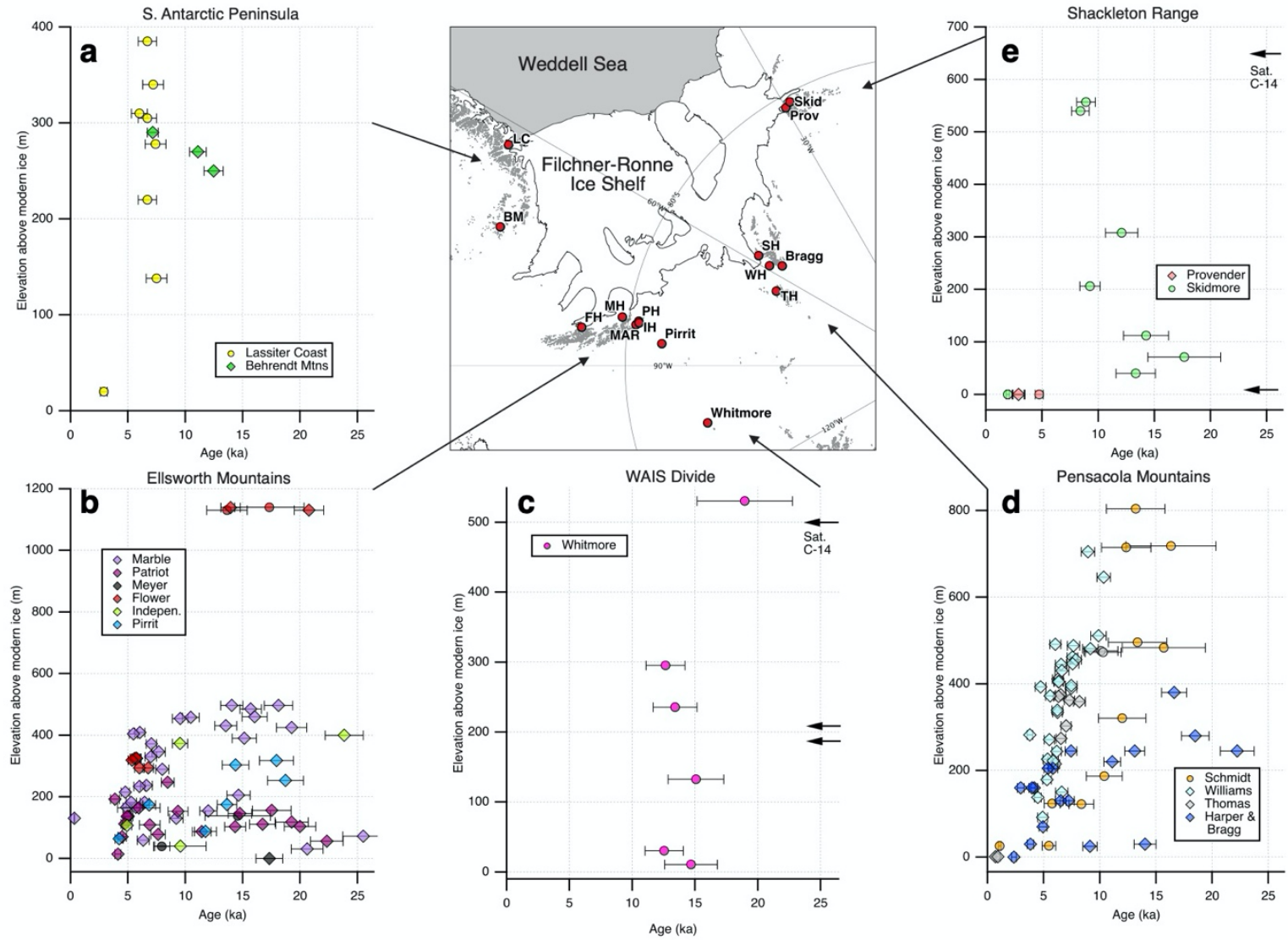


**Figure 4.1:** Post 26.5 ka  $^{10}\text{Be}$  (diamonds) and  $^{14}\text{C}$  (circles) exposure ages from the WSE. (a) Lassiter Coast (LC) and Behrendt Mountains (BM). (b) Independence (IH), Patriot (PH), Marble (MAR), Meyer (MH), and Pirrit Hills. (c) Whitmore Mountains at the Ross-Weddell divide. (d) Thomas (TH), Williams (WH), and Schmidt Hills (SH), and Mount Bragg and Mount Harper combined to form a single site (Bragg). (e) Mount Skidmore (Skid) and Mount Provender (Prov). Saturated in situ  $^{14}\text{C}$  measurements at WAIS Divide and the Shackleton Range indicated by black arrows. Grey shows exposed bedrock (SCAR Antarctic Digital Database). Base map is from the Quantarctica GIS package (Matsuoka et al., 2018).

## **2. Methods**

Our approach to evaluate ice sheet model performance using cosmogenic nuclide measurements follows that used by Spector et al. (2019). We focus on the time period of the LGM to the present. The ‘LGM’ is the maximum ice thickness during the last ca. 26.5 kyr, which may not be contemporaneous between sites, differs between models, and may differ to common global definitions of the LGM (e.g. Peltier and Fairbanks, 2006). To allow the direct comparison of different model outputs to one another, as well as to exposure ages, we present the palaeo ice sheet surface elevation relative to the final (0 ka) time slice, and present cosmogenic nuclide exposure ages using their elevation relative to the modern ice surface. Our approach thus compares the ice thickness change predicted by model outputs with that indicated by cosmogenic nuclide measurements.

Our evaluation dataset consists of the majority of post-26.5 ka  $^{10}\text{Be}$  ( $n=131$ ) and in situ  $^{14}\text{C}$  ( $n=34$ ) exposure ages from the WSE (Fig. 4.1). Four  $^{10}\text{Be}$  ages from Mount Sheffield in the Shackleton Range (Hein et al., 2011; 2014) are not included as they are sourced from the modern ice margin and thus provide little information with respect to the LGM thickness. Similarly, exposure ages from blue ice moraines in the Ellsworth Mountains are not included, as these are actively forming features and do not necessarily provide information on deglaciation or LGM thicknesses.

Exposure ages, as well as sample information including field photographs when available, are documented in the Informal Cosmogenic-Nuclide Exposure-Age Database (ICE-D) (<http://antarctica.ice-d.org/allsites>; Balco, 2020). Exposure ages are calculated using version 3 of the online calculators at [hess.ess.washington.edu](http://hess.ess.washington.edu) (Balco et al., 2008). The online calculators use the production rate scaling method for neutrons, protons, and muons following Lifton et al. (2014) and summarised in Balco (2017). The  $^{14}\text{C}$  production rate is calibrated using repeat measurements of the in situ  $^{14}\text{C}$  concentration of the CRONUS-A interlaboratory comparison standard (Jull et al., 2015; Goehring et al., 2019).

## **2.1 Ice sheet model outputs**

We use model outputs from seven studies that use three ice sheet models and one ice loading history. We study the results of Pollard et al. (2016; 2017) and Tigchelaar et al. (2018) who use the Penn State University ice-sheet model (PSU-ISM) (Deconto and Pollard, 2012), Golledge et al. (2014) and Kingslake et al. (2018) who use the Parallel Ice Sheet Model (PISM) (Winkelmann et al., 2011), and Whitehouse et al. (2012) who use the Glimmer ice sheet model (Rutt et al., 2009). The model output of Kingslake et al. (2018) is sourced from an ensemble study by Albrecht et al. (2020a, b).

We also assess the Antarctic component of the ICE-6G (VM5a) ice loading history of Argus et al. (2014) and Peltier et al. (2015). Table 4.1 summarises aspects of the model outputs, but we refer the reader to the original publications for more detailed information. The crustal ice loading history of Argus et al. (2014) differs from the aforementioned model outputs as it is not sourced from a numerical ice sheet model. The Antarctic component (ICE 6G (VM5a)) of the global ice loading history of Argus et al. (2014) and Peltier et al. (2015) does not involve the mechanical flow of ice and is instead a loading history that is adjusted to satisfy constraints on past ice sheet thickness and extent, changes in sea-level, and GPS data.

## **2.2 Interpreting cosmogenic nuclide data for ice sheet models**

In this section we outline our rationale for interpreting cosmogenic nuclide measurements with respect to their ability to record changes in past ice thickness. Cosmogenic nuclide exposure ages provide a direct measurement of past ice thickness through time. Whilst studies may yield a simple pattern of decreasing exposure age with decreasing elevation above modern ice (e.g. Fig. 4.1a, Johnson et al., 2019), samples collected at similar elevations often yield a wide range of ages (e.g. Fig. 4.1b, Bentley et al., 2010; Fogwill et al., 2014; Hein et al., 2016). It is commonplace to interpret the youngest sample at each elevation as being indicative of ice thinning (e.g. Bentley et al., 2010; Hein et al., 2016), assuming that older ages contain inherited nuclide inventories from previous periods of exposure, an assumption we use in our analysis.

Long-lived nuclides, such as  $^{10}\text{Be}$  and  $^{26}\text{Al}$ , cannot provide an upper limit on the LGM thickness of an ice mass. One may observe post-LGM ages up to an elevation above the modern ice sheet surface above which solely pre-LGM ages are found (e.g. Mount Rea in Stone et al. (2003)). Pre-LGM exposure ages at high elevations may accurately record older deglaciations, and an observed contrast between pre- and post-LGM exposure ages can be interpreted as defining the maximum LGM ice extent. However, in



Antarctica where cold-based ice dominates, high elevation surfaces may have been buried at the LGM by cold-based ice with little to no surface modification including preservation of erratic cobbles (e.g. Hein et al., 2011; Johnson et al., 2019). Therefore, long-lived nuclide measurements can only constrain the lower limit of LGM ice. When an ice sheet model predicts an LGM thickness less than the highest-elevation post-LGM exposure ages, that model output is inconsistent with the geologic constraints. Conversely, if an ice sheet model predicts an LGM thickness greater than indicated by post-LGM ages, the model output is not inconsistent with the geologic constraints (Fig. 4.2a) even though geologic data for maximum ice thickness is not the same as that in the model. When using long-lived cosmogenic nuclides, one cannot determine how much thicker than minimum constraints the ice sheet surface was in the past. Without a maximum constraint, post-LGM exposure ages do not preclude the presence of ice above the highest elevation post-LGM exposure age.

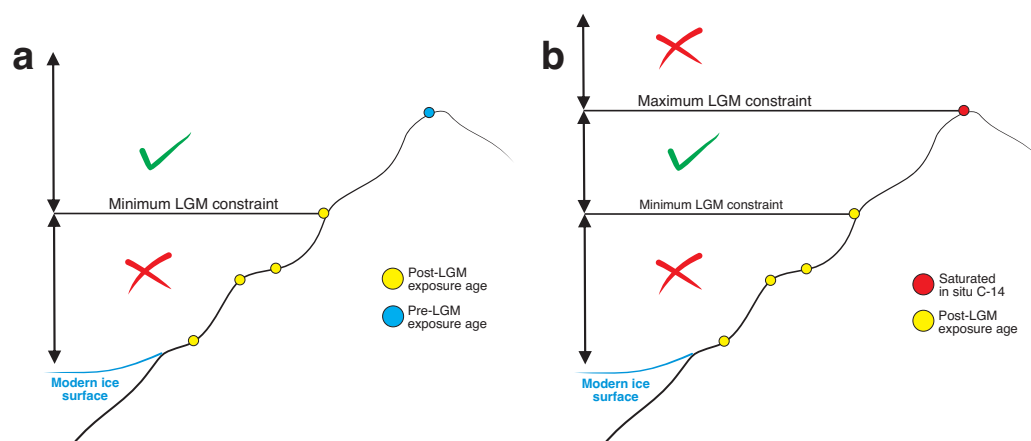


**Figure 4.2:** Two potential scenarios from measuring cosmogenic nuclide concentrations of samples collected from the surface of a nunatak and their relation to former ice extent constraints. (a) When measuring long-lived nuclides, a common outcome is a series of post-LGM exposure ages (yellow), with pre-LGM ages above them (blue). In this case, the minimum vertical extent of ice at the LGM is constrained by the highest-elevation post-LGM exposure age, with no maximum constraint. An ice sheet model must predict a total LGM thickness change greater than the minimum constraint in order to be not inconsistent with the geological observations. (b) The same upper elevation sample that yielded a pre-LGM age in (a) using a long-lived nuclide has been measured for in situ  $^{14}\text{C}$  (red). The sample is saturated with  $^{14}\text{C}$ , thus provides a maximum constraint on the thickness of LGM ice at this location. In this scenario, an ice sheet model must predict a total LGM thickness change between the highest-elevation post-LGM exposure age and the saturated measurement to be not inconsistent with the geological observations.

Unlike long-lived nuclides, measurements of in situ  $^{14}\text{C}$  can constrain the upper limit of LGM ice thickness change. The short half-life of  $^{14}\text{C}$  (5730 yr) means that a secular-equilibrium (or saturation) of the concentration is reached between production and decay after ca. 30 kyr of exposure. The saturation concentration cannot be exceeded without unusual geomorphological scenarios (e.g. Balco et al., 2019) or contamination (Nichols and Goehring, 2019). Barring this, if a sample yields a concentration

equivalent to saturation, we thus interpret that the sample was not covered by ice during the last 30 kyr. Where an ice sheet model predicts an LGM thickness that exceeds the elevation of a  $^{14}\text{C}$ -saturated sample, the modelled ice sheet behaviour is inconsistent with the in situ  $^{14}\text{C}$  constraint (Fig. 4.2b). The modelled LGM thickness is not inconsistent with exposure age constraints (in situ  $^{14}\text{C}$  or other nuclide) if it is greater than the highest elevation post-LGM exposure age and lower than the lowest elevation sample saturated with  $^{14}\text{C}$ .

An additional consideration is the fact that few cosmogenic nuclide studies report elevation measurement uncertainties. Briggs and Tarasov (2013) apply an uncertainty of  $\pm 10$  m to all elevation measurements associated with cosmogenic nuclide data lacking uncertainties. We apply the same uncertainty to all cosmogenic nuclide measurements in our evaluation. Model outputs that over- or underpredict ice thicknesses within  $\pm 10$  m of exposure age constraints are not inconsistent with the constraints.

*Figures from the intended supplement of the paper are provided here to help with the readability of this thesis chapter.*

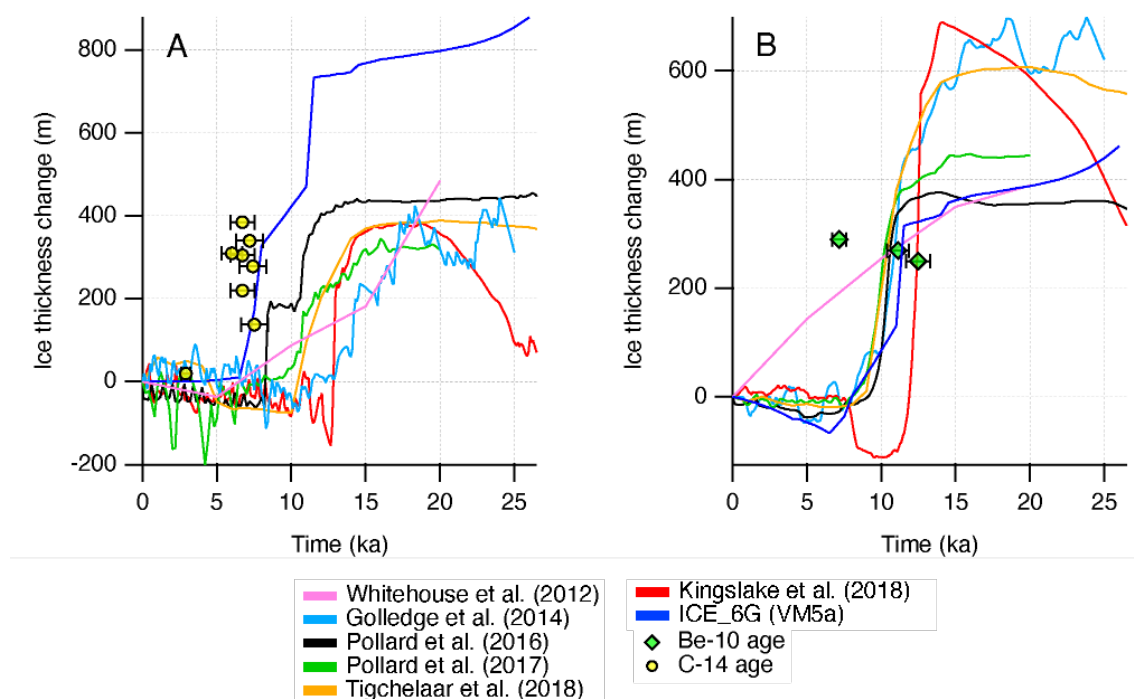


**Figure S4.1:** Modelled ice surface histories for (a) the Lassiter Coast and (b) the Behrendt Mountains on the southern Antarctic Peninsula. Exposure ages are plotted relative to the modern ice surface.

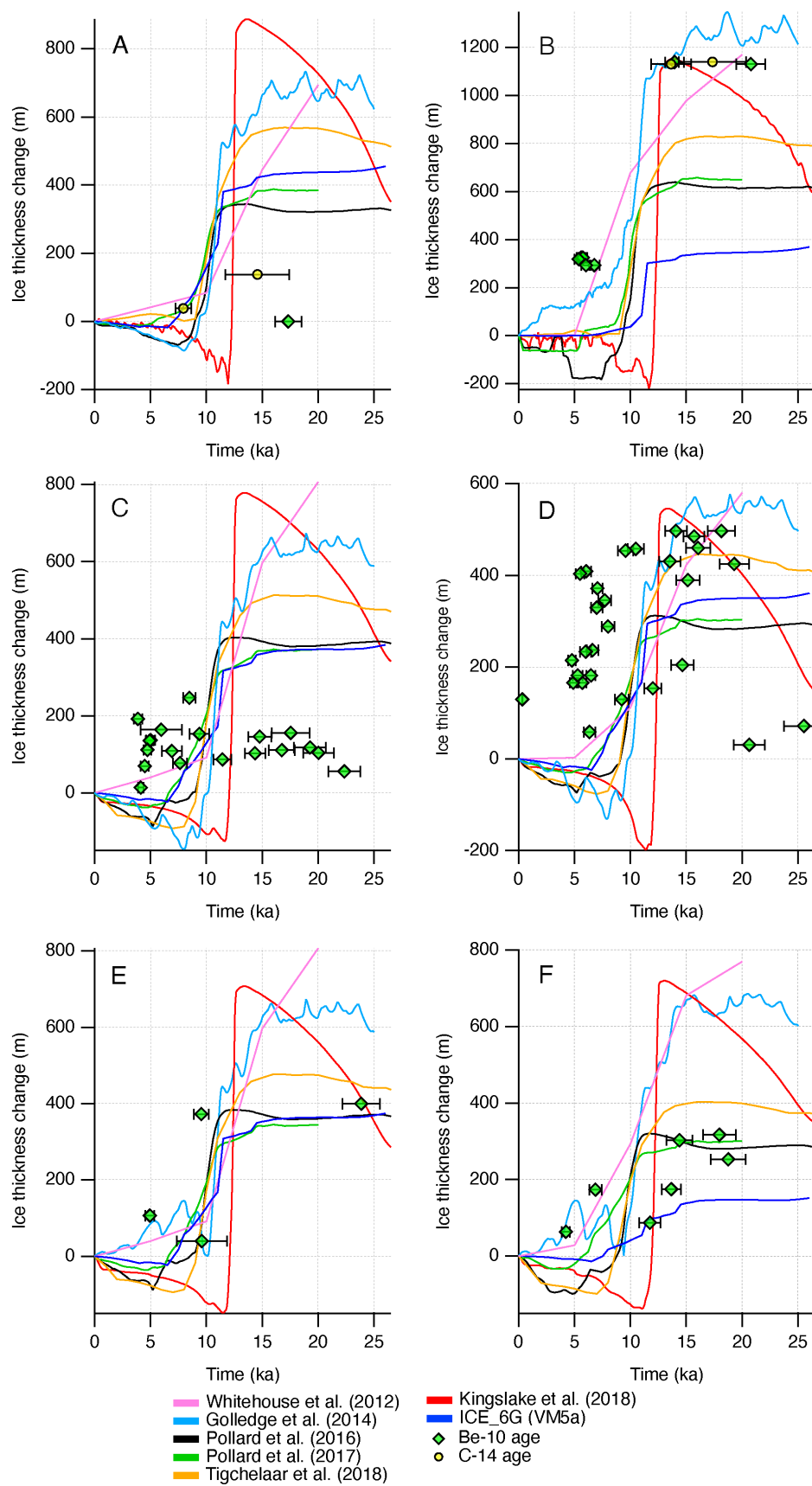


**Figure S4.2:** Modelled ice surface histories for the (a) Meyer, (b) Flower, (c) Patriot, (d) Marble, (e) Independence, and (f) Pirrit Hills in the Ellsworth Mountains.

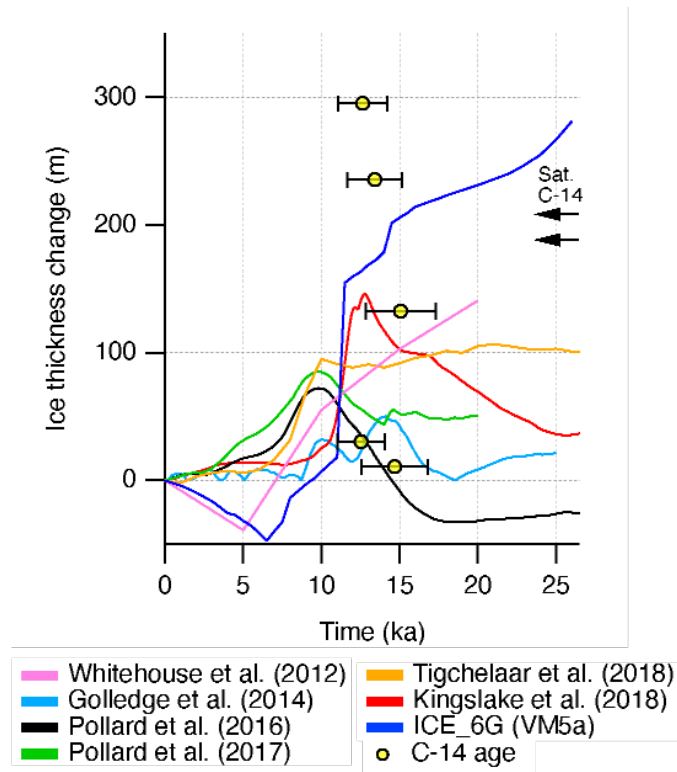


**Figure S4.3:** Modelled ice surface histories for the Whitmore Mountains at WAIS Divide.

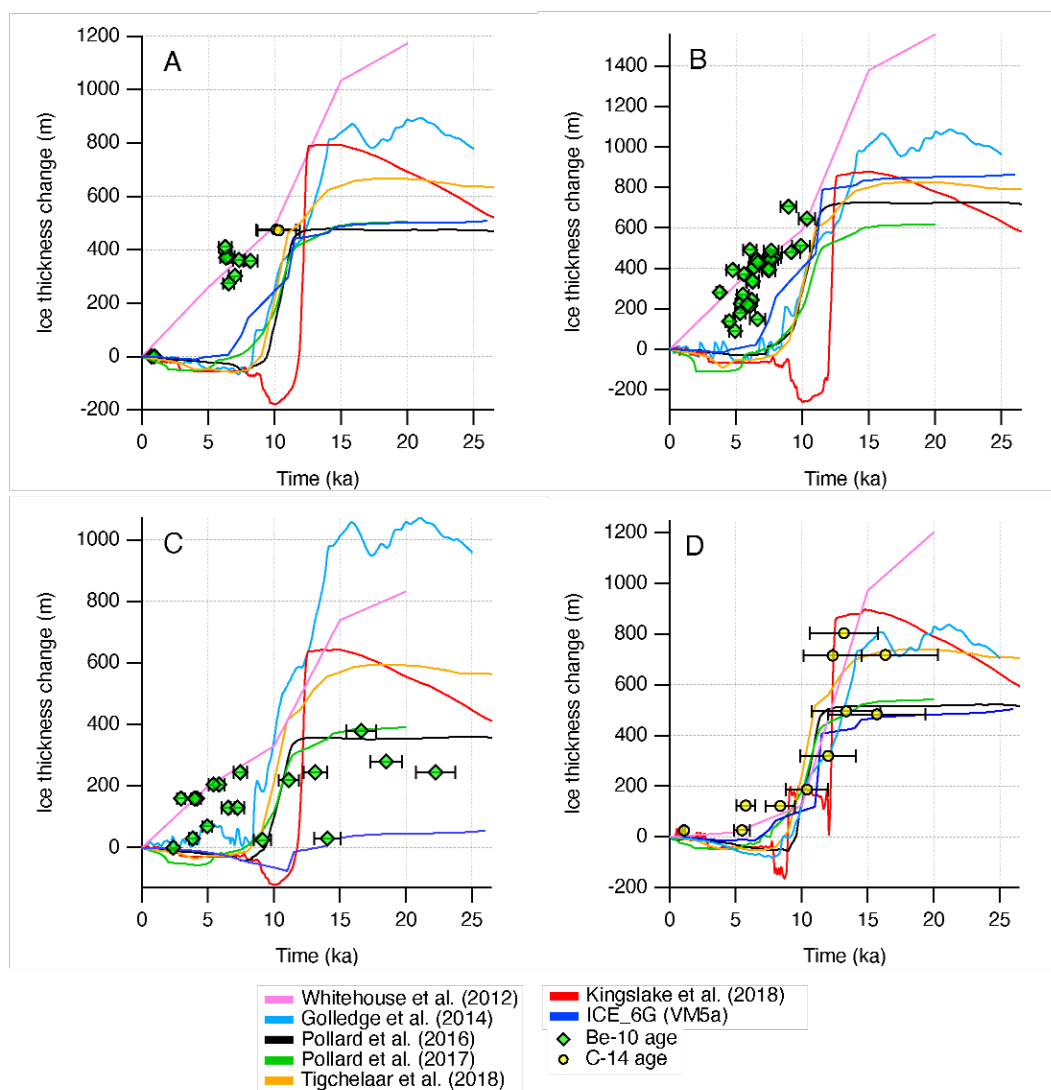


**Figure S4.4:** Modelled ice surface histories for (a) the Thomas Hills, (b) Williams Hills, (c) Mount Harper and Mount Bragg, and (d) the Schmidt Hills in the Pensacola Mountains.

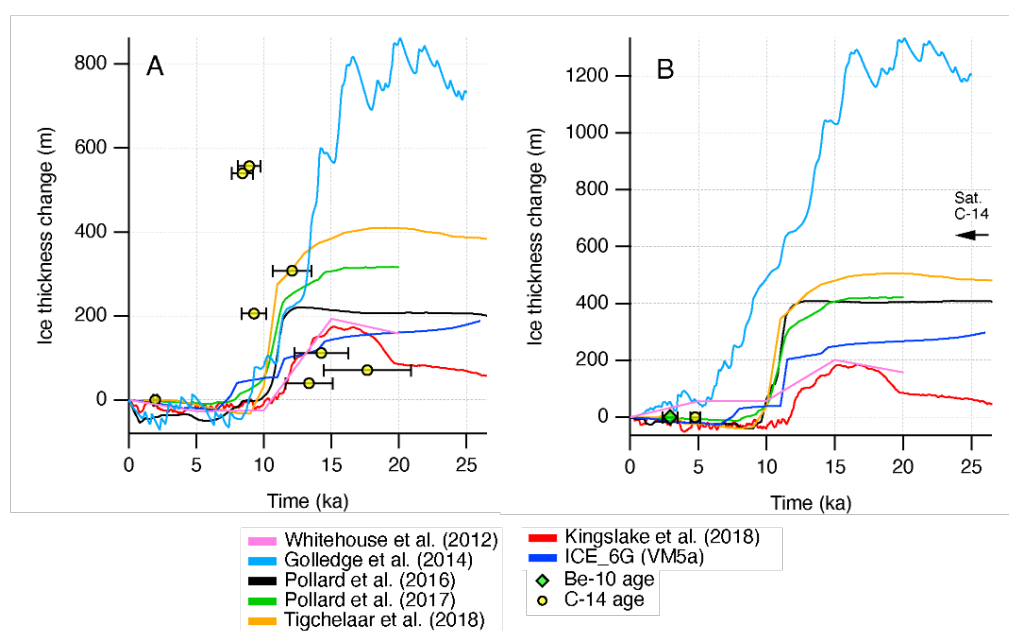


**Figure S4.5:** Modelled ice surface histories for (a) Mount Skidmore, and (b) Mount Provender in the Shackleton Range. Ice was likely at least 400 m thicker than present at Mount Provender, based on a tentative estimate by translating the modern surface profile of the Slessor Glacier to 310 m above modern ice at Mount Skidmore (20 km upstream of Mount Provender) (Nichols et al., 2019).

### **3. Discussion**

#### **3.1 LGM misfit**

We first discuss the vertical misfit between the LGM configuration from model outputs and the ice thickness change indicated by cosmogenic nuclide evidence and speculate on reasons for their distribution and magnitude (Figs. S4.1 to S4.5). The site with the most model outputs and predicted LGM thicknesses inconsistent with geologic constraints is the Whitmore Mountains ( $n = 5$ ), though the misfits are low, with a mean misfit of 61 m (Figs. 4.3 and 4.4). Four studies underpredict the LGM thickness at the Flower Hills, Schmidt Hills, and Mount Skidmore, the former two with much greater mean misfits (516 and 223 m, respectively) than the latter (105 m). At some sites, all model outputs are not inconsistent with the LGM thickness from geologic constraints, including many in the Ellsworth Mountains, and only one model is inconsistent with minimum constraints across both sites on the southern Antarctic Peninsula. The Ellsworth Mountains and the southern Antarctic Peninsula are thus, with respect to the geologically constrained LGM configuration, arguably the most well-modelled. The two earliest cosmogenic nuclide studies in the WSE (Bentley et al., 2006; 2010) are situated on the southern Antarctic Peninsula and in the Ellsworth Mountains, which may help explain why models perform well in these areas. Bentley et al. (2010) showed that ice was at least 480 m thicker than present in the Ellsworth Mountains, a constraint that was used by Whitehouse et al. (2012), Pollard et al. (2016; 2017), Kingslake et al. (2018), and Argus et al. (2014) to evaluate their own model outputs. It was later shown that ice was at least 1100 m thicker than present in the Flower Hills (Fogwill et al., 2014). The latter constraint was not used to constrain or assess any of the simulations of the studies we analysed, which may help explain why four studies underpredict LGM ice thicknesses in the Flower Hills.

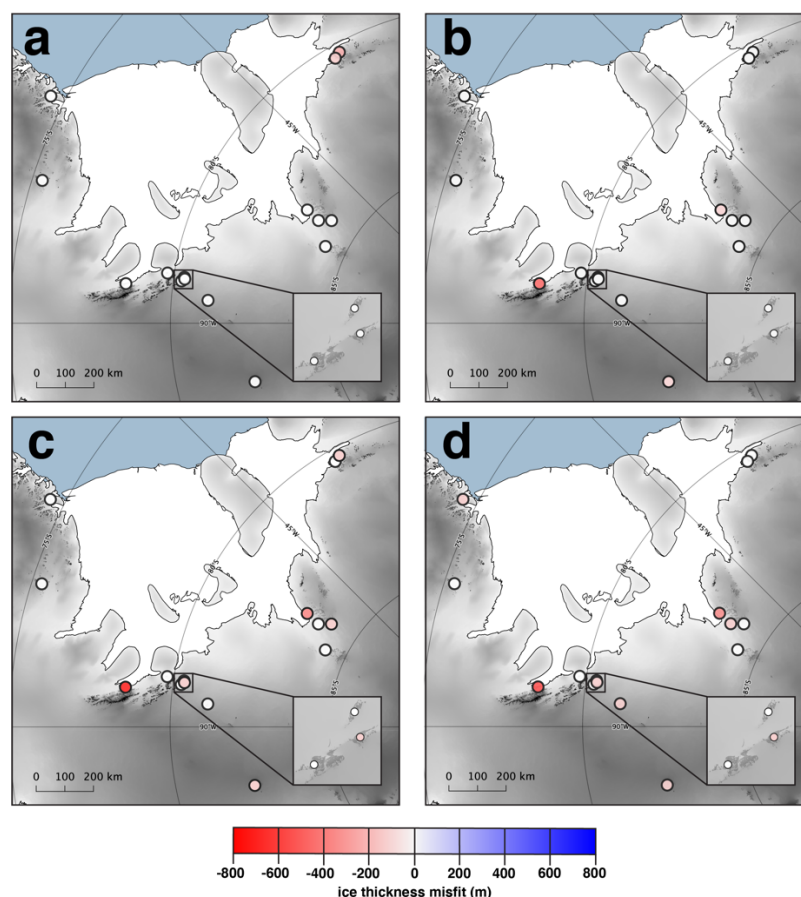


**Figure 4.3:** Misfit between total LGM ice thickness change from ice sheet model outputs and geologic constraints for (a) Whitehouse et al. (2012), (b) Tigchelaar et al. (2018), (c) Pollard et al. (2016), (d) Pollard et al. (2017). Misfits are calculated relative to the elevation of either the highest elevation post-LGM exposure age at each site or, where appropriate, relative to saturated in situ  $^{14}\text{C}$  measurements. Blue shows where the model predicted thickness change exceeds maximum constraints from saturated in situ  $^{14}\text{C}$  measurements. Red shows where the model predicted thickness change is less than that indicated by minimum constraints. Base map from the Quantarctica GIS package (Matsuoka et al., 2018). Surface topography (shading) is sourced from the Reference Elevation Model of Antarctica (REMA; Howat et al., 2019).

Two sites where we observe consistent underprediction of LGM ice thicknesses are Mount Skidmore and Mount Provender in the Shackleton Range. Multiple modelling studies use thickness estimates for the Slessor Glacier that have since been shown to underestimate the scale of LGM-to-present ice thickness change in the Shackleton Range. Models that underestimate the total ice thickness change in the Shackleton Range include Whitehouse et al. (2012), Argus et al. (2014), and Kingslake et al. (2018) (Figs. 4.3 and 4.4). Whitehouse et al. (2012) used an LGM estimate of 200 to 340 m above the modern ice surface for the Slessor Glacier in the Shackleton Range to constrain their model, based on an inferred LGM age of moraines at Mount Provender from Fogwill et al. (2004) that were, at the time, not dated. As part of their iterative process of matching the ice loading history with constraints, Argus et al. (2014) used the same cosmogenic nuclide constraints compiled by Whitehouse et al. (2012). Kingslake et al.

(2018) source palaeo constraints from the AntICEdat compilation of Briggs and Tarasov (2013). AntICEdat includes all cosmogenic nuclide constraints that were available at the time, thus the compilation contains constraints for the Shackleton Range (Hein et al., 2011). Due to cosmogenic nuclide inheritance, Hein et al. (2011) underpredict the LGM thickness of the Slessor Glacier, estimating that it was <100 m thicker than present. We now know that the Slessor Glacier was between 300 and 655 m thicker than present at the LGM (Nichols et al., 2019). It is unsurprising that, when using a range of relatively low magnitude LGM thickness change constraints in the Shackleton Range, resulting model outputs predict thickness changes smaller than the more recent geological constraints.

One model that is not inconsistent with geologic constraints at all but two study sites (Mount Provender and the Whitmore Mountains) is that of Golledge et al. (2014), which calls for an ice thickness change far in excess of minimum constraints at most study sites (Figs. S4.1 to S4.5). Rather than cosmogenic nuclide measurements, Golledge et al. (2014) use elevation changes inferred from ice cores, geodetic uplift rates, and marine evidence for the lateral expansion of ice to score their model ensemble. Uplift rate observations and marine evidence are common constraints for models (e.g. Whitehouse et al., 2012; Argus et al., 2014), but Golledge et al. (2014) appear to be the only study analysed that rely on ice core-based estimates for the WSE. Three ice cores were used to evaluate their model ensemble close to, or within, the WSE; the Berkner Island ice core, which calls for 1400 m of vertical ice thickness change since the LGM (Sasgen et al., 2005), the WAIS Divide ice core, which calls for 200 m of ice thickness change (Neumann et al., 2008), and the EPICA DML core, which calls for between -100 and + 60 m (Barbante et al., 2006). The elevation change estimate from Berkner Island is of a large magnitude, which may help explain why the model output of Golledge et al. (2014) calls for a large magnitude LGM-to-present ice thickness change at our study sites. It may also explain why the model predicts an ice thickness change that exceeds the maximum constraint (655 m) at Mount Provender. Golledge et al. (2014) acknowledge that use of exposure ages in assessing their simulations would lead them to settle on a thinner ice sheet configuration.

Overall, we find that studies using cosmogenic nuclide measurements to assess their model outputs settle on an LGM configuration that models most sites in the Ellsworth Mountains and the SE Antarctic Peninsula well in terms of ice thickness change but often underpredict thickness change in the Shackleton Range, at the Flower Hills, and at the Schmidt Hills. Models that do not use cosmogenic nuclide constraints to evaluate their simulations (Golledge et al., 2014; Tigchelaar et al., 2018) tend to call for



relatively thick LGM-to-present ice thickness change which results in few misfits due to the dearth of maximum ice thickness constraints available. Minimum ice thickness constraints from  $^{10}\text{Be}$  measurements dominate the exposure age dataset in the WSE. Maximum LGM ice thickness constraints from saturated in situ  $^{14}\text{C}$  measurements are observed in the Whitmore Mountains (Figs. 4.1 and S4.3) and at Mount Provender in the Shackleton Range (Figs. 4.1 and S4.5). At these locations we can rule out predicted LGM thicknesses that exceed the elevation of saturated measurements. At all other sites in the WSE, we have only minimum estimates for LGM ice thicknesses, thus model outputs predicting relatively thick ice thickness change are favoured as they are more likely to be not inconsistent with geologic constraints. More measurements of in situ  $^{14}\text{C}$  from high elevation nunataks in the WSE may help determine if the relatively large predicted thickness estimates are appropriate, though it is possible that most nunataks were covered by ice at the LGM and thus would not provide any additional maximum ice thickness change constraints.

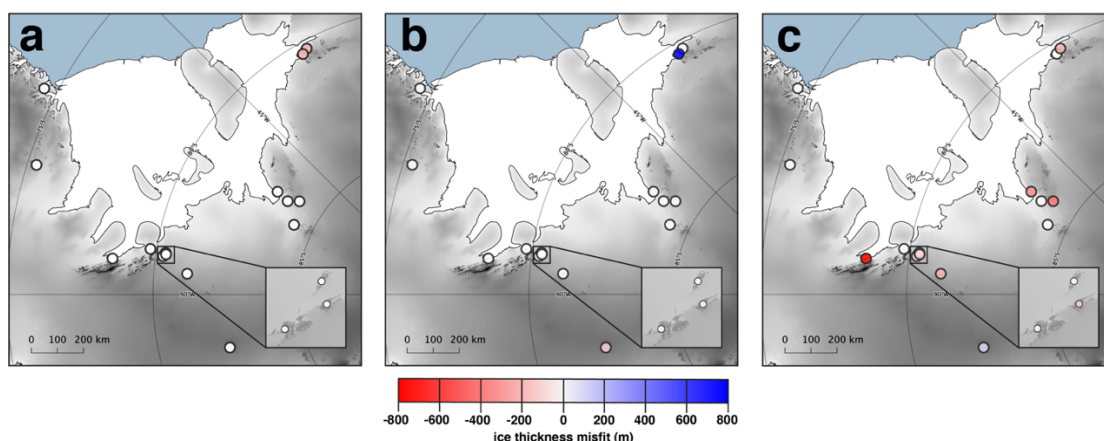


**Figure 4.4:** Misfit between total LGM ice thickness change from ice sheet model outputs and geologic constraints for (a) Kingslake et al. (2018), (b) Golledge et al. (2014), and (c) Argus et al. (2014).

### 3.2 Temporal misfit

We now know that deglaciation in the WSE was spatially complex and nonuniform, with rapid thinning in some locations, such as the Lassiter Coast and the Ellsworth Mountains, and slower thinning in others, such as at the Schmidt Hills. At the Behrendt Mountains and in the Shackleton Range, inferences we can make regarding the timing of ice surface change are hindered by sparse data for the former, and scatter in available data for the latter. It is perhaps a safe assumption that the nature of deglaciation at those study sites would be broadly consistent with other sites around the embayment. We now discuss how the model outputs reproduce the spatially variable thinning history.

Here we define the temporal misfit as the time between an exposure age, in this case the highest elevation post-LGM age at each site, and the time that a model output predicts the elevation associated with the exposure age was uncovered by ice. Negative misfits indicate thinning later than shown by exposure ages, and positive misfits indicate premature thinning. We interpolate between ice elevation data from the model outputs when they do not align with exposure ages. We observe a positive mean misfit at ten of the 14 sites, indicating that premature thinning in numerical ice sheet models is a systematic problem in the WSE (Fig. 4.5). Premature thinning is greatest at the Lassiter Coast, Independence Hills, and the Behrendt Mountains, which have with mean misfits of 8.9, 5.8, and 4 kyr, respectively. The highest negative mean misfits are observed at Mount Bragg and Mount Harper (-4.7 kyr), the Meyer Hills (-4.2 kyr), and the Pirrit Hills (-4.2 kyr). The sites with the lowest misfits, arguably the best modelled with respect to the timing of changes in ice thickness and thus using the best representation of forcings and/or ice physics, are the Marble Hills (0.7 kyr) and the Whitmore Mountains (-1 kyr), though only three model outputs at each site predict LGM-to-present ice thickness change sufficient to bury the highest elevation exposure ages.

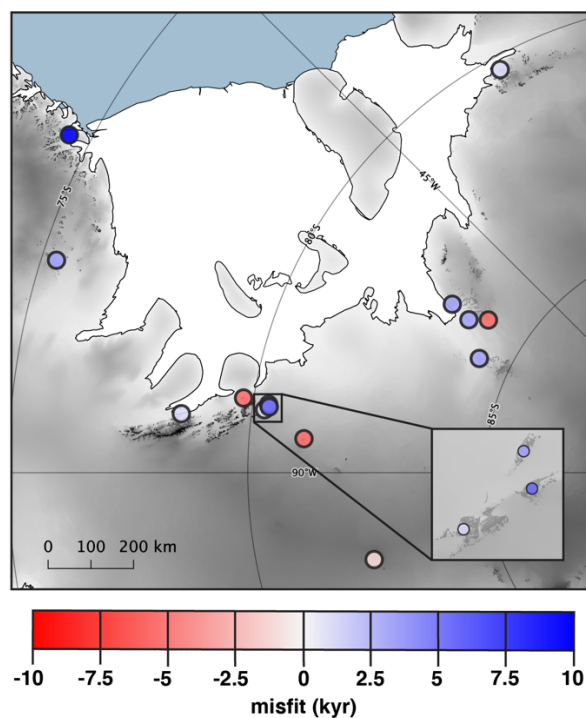


**Figure 4.5:** Mean temporal misfit between the highest elevation post-LGM exposure age at each site and the time that each model predicts that elevation was uncovered. The number of study sites varies between three and seven as not all model outputs predict a sufficient ice thickness change to cover the highest altitude exposure age at each site. Negative misfits indicate thinning later than exposure ages, positive misfits indicate premature thinning.

In addition to prevalent premature thinning around the WSE, we often observe thinning that occurs more rapidly than indicated by exposure ages. At all sites, the misfit between model outputs and exposure ages increases toward the present (Fig. 4.6), indicative of thinning in models that is more rapid than geologic constraints permit. At the Patriot (Fig. 4.6a) and Williams Hills (Fig. 4.6d), thinning is primarily premature throughout the duration of model outputs, with positive misfits increasing toward the present. At these sites, thinning in models occurs both too early and too quickly. At the Marble Hills (Fig. 4.6b), Pirrit Hills (Fig. 3.6c), Mount Harper and Mount Bragg (Fig. 4.6e), and the Schmidt Hills (Fig. 4.6f), many model outputs initially predict late thinning, but thinning again occurs too rapidly and an increasing positive misfit is observed toward the present. At these latter sites, thinning begins late but, much like at the Patriot and Williams Hills, occurs too quickly and thus overtakes the thinning history indicated by the exposure ages.

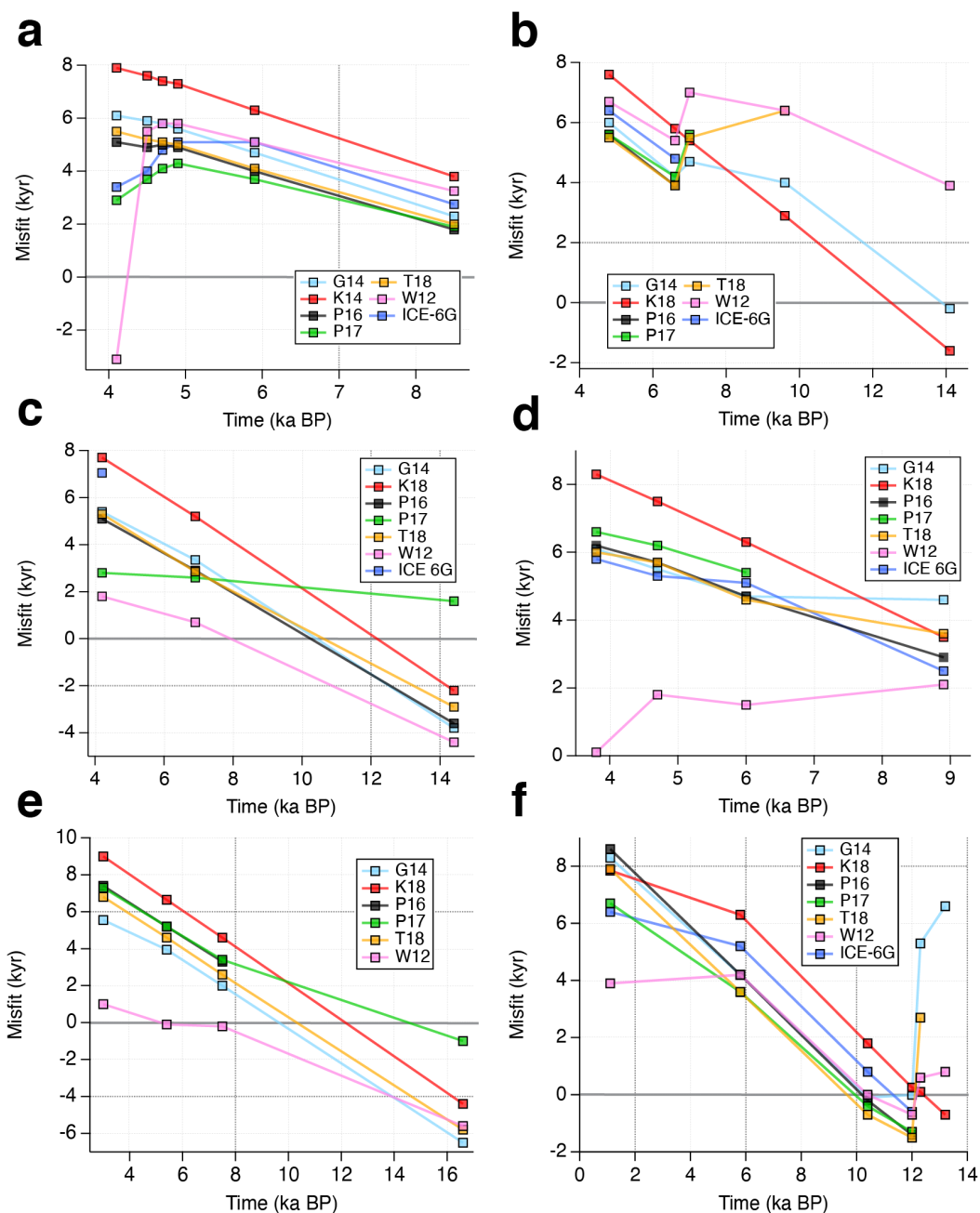


**Figure 4.6:** Temporal misfit between exposure ages and the time the elevation associated with each age is deglaciated by model outputs for the (a) Patriot, (b) Marble, (c) Pirrit, (d) and Williams Hills, (e) Mount Harper and Mount Bragg, and (f) the Schmidt Hills. Sites included are those for which a high resolution deglaciation history can be reconstructed. Each data point represents an exposure age and predicted ice surface elevations from the model outputs are interpolated when necessary.

Not included in Fig. 4.6 is the Lassiter Coast. At the Lassiter Coast, rapid thinning of ca. 300 m is observed at ca. 7 ka (Fig. S4.1a; Johnson et al., 2019). The timing and scale of ice thinning observed at the Lassiter Coast is similar to that observed for the Mackay Glacier in the western Ross Sea, where  $^{10}\text{Be}$  ages show 200 m of thinning at ca. 7 ka (Jones et al., 2015). The Lassiter Coast is located close to the modern Ronne Ice Shelf edge, similarly to how the Mackay Glacier is located close to the modern Ross Ice Shelf Edge. Jones et al. (2015) hypothesise that rapid thinning of the Mackay Glacier is caused by a

loss of ice shelf buttressing and resulting marine ice sheet instability, which may also be the case at the Lassiter Coast. Rapid thinning on the scale of that exhibited by many model outputs is shown by exposure ages at the Lassiter Coast, but thinning again occurs too early in the models. Evidently, the mechanisms to produce rapid thinning consistent with exposure ages at the Lassiter Coast are present in the numerical ice sheet models, but the timing of said thinning is too early. In their own evaluation of their model output, Whitehouse et al. (2012) suggest that premature thinning in the WSE is caused by their prescribed grounding line positions, which may be the case for other model outputs as well.

One potential explanation to account for the temporal misfit and/or the slower thinning evidenced by exposure ages than that exhibited by the ice sheet models may be our relatively poor knowledge of the bed topography beneath the modern day Filchner Ronne Ice Shelf. Many modelling studies used the BEDMAP2 bed topography dataset (Fretwell et al., 2013), or in the case of Whitehouse et al. (2012), the ALBMAP v1 bed topography of Le Brocq et al. (2010), which is based on the earlier BEDMAP dataset (Lythe et al., 2001). These datasets may be missing bed features that may have formed pinning points for retreating ice masses, causing temporary stabilisation and a lag between, for example, sea-level forcing and glacier response. Although our knowledge of bed topography is improving (e.g. Jeffrey et al. (2018) and the BedMachine dataset of Morlighem et al. (2020)), it may be some time before fine scale bed features that may form important pinning points can be incorporated into continent-wide numerical ice sheet simulations. One way to help may be to focus on simulating the WAIS or individual WSE sector, or flowline modelling of individual ice streams.

### **3.3 Evaluating models with $^{14}\text{C}$**

Spector et al. (2019) present an approach to assess the feasibility of hypothetical ice-cover scenarios and ice sheet model outputs using in situ  $^{14}\text{C}$  concentrations. Here we use Equation 1 (Spector et al., 2019) to assess model outputs at locations around the WSE where measurements of in situ  $^{14}\text{C}$  are available. The measured  $^{14}\text{C}$  concentration ( $N$ ) is described for an exposure history for a theoretical geological sample adjacent to an ice mass by:

$$N = \frac{P}{\lambda} [1 + \exp(-\lambda t_{\text{cover}}) - \exp(-\lambda t_{\text{expose}})] \quad (1),$$

Where  $P$  is the site  $^{14}\text{C}$  production rate,  $\lambda$  the  $^{14}\text{C}$  decay constant,  $t_{\text{cover}}$  the timing of ice cover, and  $t_{\text{expose}}$  the timing of deglaciation following the LGM. To apply this equation, we assume that the sample undergoes three stages in its exposure history. First, the sample is assumed to have been exposed for at least ca. 30 kyr and is thus  $^{14}\text{C}$  saturated, prior to LGM ice cover. Next, the sample undergoes burial by ice starting at time  $t_{\text{cover}}$ , at which point the production of in situ  $^{14}\text{C}$  is assumed to cease immediately. Finally, at time  $t_{\text{expose}}$ , the sample is re-exposed following thinning of the ice sheet, and production of in situ  $^{14}\text{C}$  resumes immediately. We use a range of values of  $t_{\text{cover}}$  and  $t_{\text{expose}}$  (0 to up to 35 ka, the upper limit of in situ  $^{14}\text{C}$  exposure dating) to calculate a range of possible in situ  $^{14}\text{C}$  concentrations for a given sample. We assume there has been no snow cover, so that the sample has remained unshielded since re-exposure.

The predicted ice elevation histories of Kingslake et al. (2018) and Tigchelaar et al. (2018) are the only model outputs that both cover and re-expose samples at the Lassiter Coast during the last 35 kyr. Most model outputs, at most study sites in the WSE, begin at a maximum LGM thickness and thin to the present. Consequently, sample elevations are covered from the beginning of model runs and we are unable to deduce  $t_{\text{cover}}$ . It is important to note that we can neither confirm nor refute the possibility given our exposure age dataset that not all sampled elevations were ice-free prior to the LGM, and that this is not a trivial assumption. For the models that begin at or about a maximum LGM thickness and thin to the present, the predicted cosmogenic nuclide concentrations would be equivalent to the time that surfaces were exposed following the LGM, producing a simple post-LGM age-elevation thinning history. The longer records of Kingslake et al. (2018) and Tigchelaar et al. (2018) simulate ice thickening into the LGM, followed by thinning to the present. Consequently, at some sites, sample elevations are buried during the LGM and exposed afterwards, which allows us to assess the model outputs using individual measurements of in situ  $^{14}\text{C}$ . The ice history of Tigchelaar et al. (2018) and presumably Kingslake et al. (2018) are consistent with the assumption that samples are saturated with respect to in situ  $^{14}\text{C}$  prior to the LGM.

In Fig. 4.7b, the black dashed lines show the range of combinations of  $t_{\text{cover}}$  and  $t_{\text{expose}}$  that produce in situ  $^{14}\text{C}$  concentrations consistent with the concentration (and measurement uncertainty) of sample P11.12.6 from Johnson et al. (2019), the highest elevation sample relative to modern ice measured for in situ  $^{14}\text{C}$  at the Lassiter Coast. The model output of Tigchelaar et al. (2018) predicts that this sample is buried at 22 ka and re-exposed at 20 ka (Fig. 4.7a). The combination of  $t_{\text{cover}}$  (22 ka) and  $t_{\text{expose}}$  (20 ka)

are represented in Fig. 4.7b by the orange square. The model output of Tigchelaar et al. (2018) is the only model output that predicts both cover and exposure of sample P11.12.6. We observe that the orange square is outside of the envelope of allowable exposure histories. Thus, the timing of cover and re-exposure predicted by Tigchelaar et al. (2018) is out of the range of cover and exposure ages permitted by the measured concentration. In other words, the predicted timing of burial and re-exposure of the sample is inconsistent with the geologic constraint. To plot within the allowable range from the measured concentration, thinning and thus re-exposure needs to occur later than currently predicted by the model.

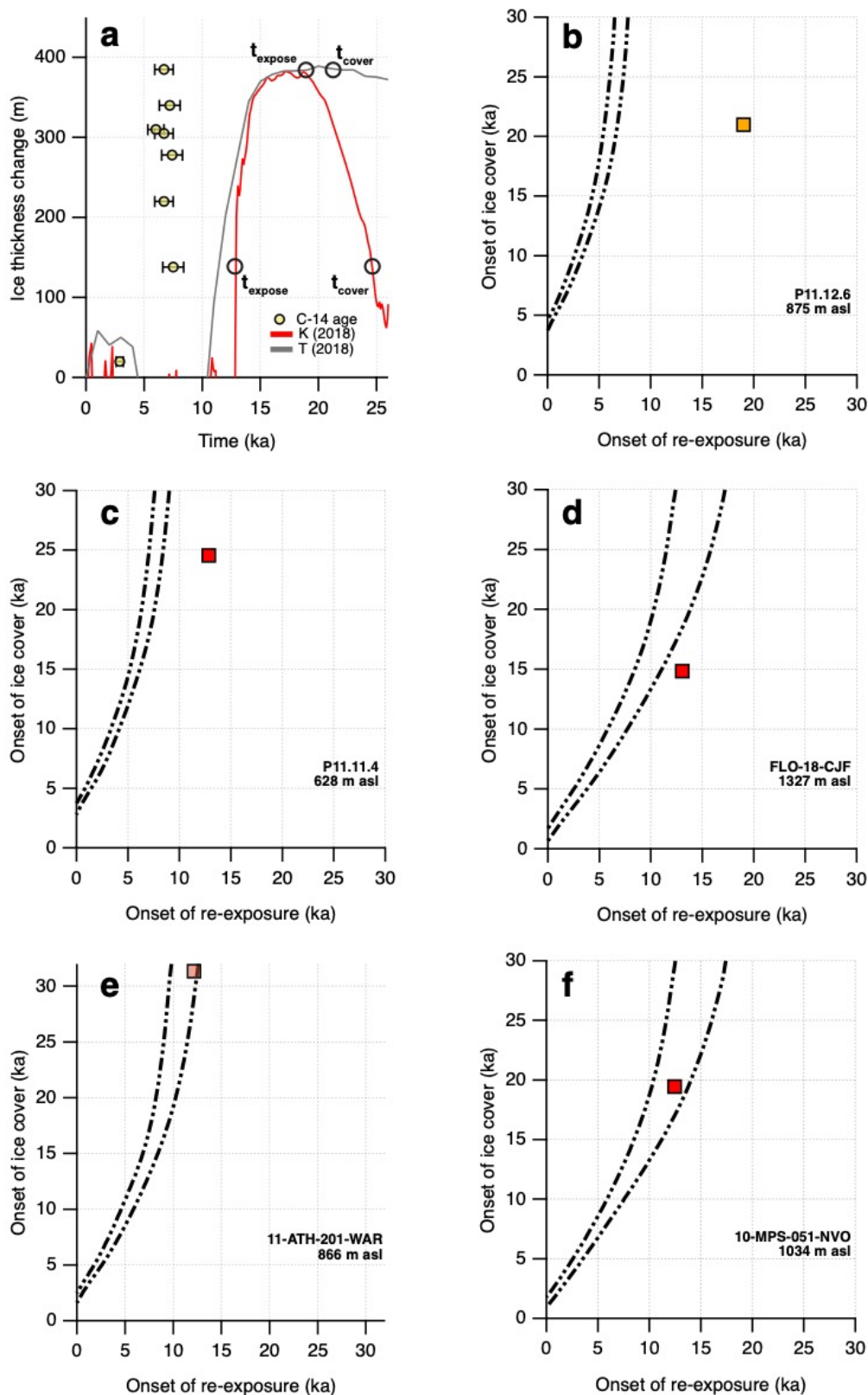


**Figure 4.7:** (a) Modelled ice surface histories of Kingslake et al. (2018) and Tigchelaar et al. (2018) for Mount Lampert on the Lassiter Coast. Exposure ages from Johnson et al. (2019) and Nichols et al. (2019). Labels  $t_{\text{cover}}$  and  $t_{\text{expose}}$  indicate when the two ice histories cover and expose two of the samples. The highest elevation sample is covered and exposed by the modelled ice history of Tigchelaar et al. (2018) and forms the basis of (b). The second-lowest elevation sample is covered and exposed by the modelled ice history of Kingslake et al. (2018) and forms the basis of (c). (b) Orange square represents  $t_{\text{cover}}$  and  $t_{\text{expose}}$  predicted by Tigchelaar et al. (2018) for a sample collected from 385 m above the modern ice



surface at the Lassiter Coast. Dashed lines show the range of  $t_{\text{cover}}$  and  $t_{\text{expose}}$  that produce a  $^{14}\text{C}$  concentration equivalent to that of sample the sample. (c) Same as (b), but the red square represents  $t_{\text{cover}}$  and  $t_{\text{expose}}$  predicted by Kingslake et al. (2018) for a different sample collected from 138 m above modern ice at the Lassiter Coast. (d) Plot for a sample collected 1130 m above modern ice at the Flower Hills. (e) Sample collected from the Thomas Hills, and (f) sample collected from the Schmidt Hills. For the (e) and (f), red represents  $t_{\text{cover}}$  and  $t_{\text{expose}}$  predicted by Kingslake et al. (2018) for each sample.

Next, we look at the model output of Kingslake et al. (2018), again at the Lassiter Coast, but evaluate the model output using an in situ  $^{14}\text{C}$  concentration from a different sample to the preceding one. The model output does not cover the highest elevation sample, however, unlike the record of Tigchelaar et al. (2018), Kingslake et al. (2018) predict that the second lowest elevation sample collected from 138 m above the modern ice surface is covered and exposed during the last 35 kyr (Fig. 4.7a). Other than the sample 20 m above the modern ice surface, all other samples yield apparent ages of ca. 6.5 to 7 ka (Johnson et al., 2019). The sample from 138 m above the modern ice surface (P11.11.4 from Johnson et al., 2019) is, logically, buried for the longest duration, which means that this sample provides the most lenient test for the model output and is a thus good starting point to assess it. If the model output is inconsistent with the sample from 138 m above the modern ice, it is not possible for it to be to be consistent with the other samples from higher elevations, given that they yield approximately the same age but are buried for a shorter time by the model output.

The predicted timing of cover and exposure for sample P11.11.4 using Kingslake et al. (2018) is outside of the permitted range from the in situ  $^{14}\text{C}$  concentration of sample P11.11.4 (Fig. 4.7c). The timing of cover and exposure predicted by Kingslake et al. (2018) is, however, closer to the permitted range than in the previous example. If the onset of ice cover is kept the same, the sample at 138 m above modern ice must be re-exposed at least ca. 5 kyr later by the model output of Kingslake et al. (2018) to be consistent with the  $^{14}\text{C}$  measurement.

Now we turn our attention to the Flower Hills, where there is an in situ  $^{14}\text{C}$  measurement (Fogwill et al., 2014; FLO-18-CJF) collected from ca. 1130 m above the Rutford Ice Stream. The only model output to predict both cover and exposure of sample FLO-18-CJF is that of Kingslake et al. (2018). Again, the predicted exposure history is outside the range of exposure histories allowed by the measured in situ  $^{14}\text{C}$  concentration (Fig. 4.7d). An additional ca. 3 kyr of burial is required to produce an in situ  $^{14}\text{C}$  concentration consistent with the geologic constraints.

Finally, we look at two examples where model outputs are consistent with in situ  $^{14}\text{C}$  constraints, both in the Pensacola Mountains. At both locations, the model output of Kingslake et al. (2018) is again

the only model output to predict both the cover and exposure of the samples in question. In the Thomas Hills, Kingslake et al. (2018) predict burial of sample 11-ATH-201-WAR (Nichols et al., 2019) at 31.4 ka, and re-exposure at 12.2 ka, consistent with the range of exposure histories permitted by the measured in situ  $^{14}\text{C}$  concentration (Fig. 4.7e). In the Schmidt Hills, Kingslake et al. (2018) predict the burial of sample 10-MPS-051-NVO (Nichols et al., 2019) at 19.5 ka and re-exposure at 12.5 ka, consistent with the range of exposure histories permitted by the in situ  $^{14}\text{C}$  measurement (Fig. 4.7f). Spector et al. (2019) also showed that the exposure history predicted by Kingslake et al. (2018) is consistent with an situ  $^{14}\text{C}$  measurement from ca. 130 m above modern ice in the Whitmore Mountains.

The section above outlines how in situ  $^{14}\text{C}$  measurements can be used to evaluate model outputs. As well as being consistent with respect to the total LGM thickness change, the reference simulation of Kingslake et al. (2018) is consistent with in situ  $^{14}\text{C}$  constraints in the Thomas Hills, Schmidt Hills, and Whitmore Mountains. It is, however, inconsistent with constraints at the Lassiter Coast and Flower Hills. In practice, it is not yet feasible to undertake this type of model evaluation on a wide scale because: (i) most ice sheet models simulate from a maximum LGM thickness to the present to study deglaciation, with no information on when samples were covered prior to the LGM, and (ii) there is a general lack of in situ  $^{14}\text{C}$  measurements available to evaluate the model outputs that do simulate thickening, and thus the burial of samples, into the LGM.

### **3.4 Future work in the WSE**

Regarding future ice sheet modelling endeavours undertaken in the WSE, studies will ideally focus on the time period of from at least 35 ka to the present, including the build-up of ice into the LGM, possibly informed by paired measurements of in situ  $^{14}\text{C}$ . By covering a longer timescale, the model outputs can be rigorously evaluated with in situ  $^{14}\text{C}$  measurements. We now know much about the nature of deglaciation in the WSE, and future modelling studies should aim to reproduce the spatially-variable pattern of ice thinning indicated by exposure ages. This would include reproducing rapid thinning in some locations, such as the Lassiter Coast and the Ellsworth Mountains, in addition to matching the timing of ice thinning to exposure ages around the embayment.

We do not want to speculate in depth about model forcings and how they should be altered to permit thicker ice at sites where the LGM thickness is often underpredicted (e.g. Flower Hills and sites in the Shackleton Range). However, one avenue might be to alter basal conditions in models. Many studies,

such as those using PSU-3D and PISM, use a constant basal sliding distribution that agrees reasonably well with the modern ice sheet configuration. A time-varying basal sliding distribution (Vogel et al., 2003; Whitehouse et al., 2012), which would impose less slippery conditions than present in the past, could potentially allow a greater build-up of ice during the LGM in the WSE (A. R. Halberstadt, personal communication). Any change in basal conditions would need to be balanced with other model inputs to provide sufficient melting from the LGM to the present to reach a configuration that agrees reasonably well with modern observations. Pollard et al. (2016) found reasonable agreement between palaeo constraints and their model ensemble when using lower basal sliding coefficient values which allowed a greater thickness of ice to build up during the LGM. However, the larger magnitude ice thickness required increased oceanic melt rates beneath floating ice shelves and a decreased  $e$ -folding time of bedrock-elevation isostatic relaxation to sufficiently thin to match the present day configuration of the ice sheet.

#### **4. Conclusions**

We present an evaluation of numerical ice sheet model outputs using cosmogenic nuclide constraints in the WSE. We find that locations with established cosmogenic nuclide constraints are the most well-modelled with respect to the total LGM-to-present ice thickness change, including sites on the southern Antarctic Peninsula and most sites in the Ellsworth Mountains. Sites with the most model outputs inconsistent with minimum ice thickness constraints are the Flower Hills in the Ellsworth Mountains, the Schmidt Hills in the Pensacola Mountains, and Mount Skidmore in the Shackleton Range.

A lack of maximum ice thickness constraints is an important limiting factor for our evaluation. Without maximum ice thickness constraints, we are unable to evaluate ice sheet model outputs that predict relatively large magnitude ice thickness changes that exceed minimum ice thickness constraints at many sites. Consequently, a lack of maximum ice thickness constraints means that our evaluation favours numerical ice sheet model outputs that call for relatively thick LGM ice in the WSE.

We observe differences between the timing of ice thickness change indicated by exposure ages and predicted by ice sheet model outputs. At most sites, deglaciation occurs both earlier and more rapidly than exposure ages show.

Finally, we show that few model outputs are consistent with individual measurements of in situ  $^{14}\text{C}$  with respect to the model-predicted timing of the onset of ice cover and post-LGM re-exposure. However, most numerical ice sheet model outputs cannot be evaluated using individual measurements of in situ  $^{14}\text{C}$  because the model outputs do not provide a predicted timing of the onset of ice cover prior to the LGM. We hope that future ice sheet modelling studies will simulate from prior to the LGM, in addition to the undertaking of more high elevation in situ  $^{14}\text{C}$  measurements which could provide valuable maximum ice constraints which are currently lacking.

## **References**

- Albrecht, T., Winkelmann, R. and Levermann, A.: Glacial-cycle simulations of the Antarctic Ice Sheet with the Parallel Ice Sheet Model (PISM)-Part 2: Parameter ensemble analysis, *Cryosph.*, 14(2), 633–656, doi:10.5194/tc-14-633-2020, 2020a.
- Albrecht, T., Winkelmann, R. and Levermann, A.: Glacial-cycle simulations of the Antarctic Ice Sheet with the Parallel Ice Sheet Model (PISM) – Part 1: Boundary conditions and climatic forcing, *Cryosph.*, 14(2), 599–632, doi:10.5194/tc-14-633-2020, 2020b.
- Argus, D. F., Peltier, W. R., Drummond, R. and Moore, A. W.: The Antarctica component of postglacial rebound model ICE-6G\_C (VM5a) based on GPS positioning, exposure age dating of ice thicknesses, and relative sea level histories, *Geophys. J. Int.*, 198(1), 537–563, doi:10.1093/gji/ggu140, 2014.
- Arndt, J. E., Hillenbrand, C.-D., Grobe, H., Kuhn, G. and Wacker, L.: Evidence for a dynamic grounding line in outer Filchner Trough, Antarctica, until the early Holocene, *Geology*, 45(11), 1035–1038, doi:10.1130/G39398.1, 2017.
- Balco, G., Todd, C., Goehring, B.M., Moening-Swanson, I., Nichols, K.: Glacial geology and cosmogenic-nuclide exposure ages from the Tucker Glacier - Whitehall Glacier confluence, northern Victoria Land, Antarctica, *Am. J. Sci.*, 319(April), 255–286, doi:10.2475/04.2019.01, 2019.
- Balco, G.: Production rate calculations for cosmic-ray-muon-produced  $^{10}\text{Be}$  and  $^{26}\text{Al}$  benchmarked against geological calibration data, *Quat. Geochronol.*, 39, 150–173, doi:10.1016/j.quageo.2017.02.001, 2017.
- Balco, G.: Technical note: A prototype transparent-middle-layer data management and analysis infrastructure for cosmogenic-nuclide exposure dating, *Geochronology*, 2, 169–175, doi:10.5194/gchron-2020-6, 2020.
- Balco, G., Stone, J. O., Lifton, N. A. and Dunai, T. J.: A complete and easily accessible means of calculating surface exposure ages or erosion rates from  $^{10}\text{Be}$  and  $^{26}\text{Al}$  measurements, *Quat. Geochronol.*, 3(3), 174–195, doi:10.1016/j.quageo.2007.12.001, 2008.

- Balco, G., Todd, C., Huybers, K., Campbell, S., Vermeulen, M., Hegland, M., Goehring, B. M. and Hillebrand, T. R.: Cosmogenic-nuclide exposure ages from the Pensacola Mountains adjacent to the Foundation Ice Stream, Antarctica, *Am. J. Sci.*, 316(6), 542–577, doi:10.2475/06.2016.02, 2016.
- Barbante, C., Barnola, J.-M., Becagli, S., Beer, J., Bigler, M., Boutron, C., Blunier, T., Castellano, E., Cattani, O., Chappellaz, J., Dahl-Jensen, D., Debret, M., Delmonte, B., Dick, D., Falourd, S., Faria, S., Federer, U., Fischer, H., Freitag, J., Frenzel, A., Fritzsche, D., Fundel, F., Gabrielli, P., Gaspari, V., Gersonde, R., Graf, W., Grigoriev, D., Hamann, I., Hansson, M., Hoffmann, G., Hutterli, M. A., Huybrechts, P., Isaksson, E., Johnsen, S., Jouzel, J., Kaczmarek, M., Karlin, T., Kaufmann, P., Kipfstuhl, S., Kohno, M., Lambert, F., Lambrecht, A., Lambrecht, A., Landais, A., Lawer, G., Leuenberger, M., Littot, G., Loulergue, L., Lüthi, D., Maggi, V., Marino, F., Masson-Delmotte, V., Meyer, H., Miller, H., Mulvaney, R., Narcisi, B., Oerlemans, J., Oerter, H., Parrenin, F., Petit, J.-R., Raisbeck, G., Raynaud, D., Röthlisberger, R., Ruth, U., Rybak, O., Severi, M., Schmitt, J., Schwander, J., Siegenthaler, U., Siggaard-Andersen, M.-L., Spahni, R., Steffensen, J. P., Stenni, B., Stocker, T. F., Tison, J.-L., Traversi, R., Udasti, R., Valero-Delgado, F., van den Broeke, M. R., van de Wal, R. S. W., Wagenbach, D., Wegner, A., Weiler, K., Wilhelms, F., Winther, J.-G., Wolff, E. and Members, E. C.: One-to-one coupling of glacial climate variability in Greenland and Antarctica, *Nature*, 444(7116), 195–198, doi:10.1038/nature05301, 2006.
- Bentley, M. J. and Anderson, J. B.: Glacial and marine geological evidence for the ice sheet configuration in the Weddell Sea–Antarctic Peninsula region during the Last Glacial Maximum, *Antarct. Sci.*, 10(3), 309–325, doi:10.1017/s0954102098000388, 1998.
- Bentley, M. J., Fogwill, C. J., Kubik, P. W. and Sugden, D. E.: Geomorphological evidence and cosmogenic  $^{10}\text{Be}/^{26}\text{Al}$  exposure ages for the Last Glacial Maximum and deglaciation of the Antarctic Peninsula Ice Sheet, *Bull. Geol. Soc. Am.*, 118(9–10), 1149–1159, doi:10.1130/B25735.1, 2006.
- Bentley, M. J., Fogwill, C. J., Brocq, A. M. Le, Hubbard, A. L., Sugden, D. E., Dunai, T. J. and Freeman, S. P. H. T.: Deglacial history of the West Antarctic Ice Sheet in the Weddell Sea embayment: Constraints on past ice volume change, *Geol. Soc. Am.*, 38(5), 411–414, doi:10.1130/G30754.1, 2010.

- Bentley, M. J., Hein, A. S., Sugden, D. E., Whitehouse, P. L., Shanks, R., Xu, S. and Freeman, S. P. H. T.: Deglacial history of the Pensacola Mountains, Antarctica from glacial geomorphology and cosmogenic nuclide surface exposure dating, *Quat. Sci. Rev.*, 158, 58–76, doi:10.1016/j.quascirev.2016.09.028, 2017.
- Briggs, R. D. and Tarasov, L.: How to evaluate model-derived deglaciation chronologies: A case study using Antarctica, *Quat. Sci. Rev.*, 63, 109–127, doi:10.1016/j.quascirev.2012.11.021, 2013.
- Le Brocq, A. M., Payne, A. J. and Vieli, A.: An improved Antarctic dataset for high resolution numerical ice sheet models (ALBMAP v1), *Earth Syst. Sci. Data*, 2(2), 247–260, doi:10.5194/essd-2-247-2010, 2010.
- Fogwill, C. J., Bentley, M. J., Sugden, D. E., Kerr, A. R. and Kubik, P. W.: Cosmogenic nuclides  $^{10}\text{Be}$  and  $^{26}\text{Al}$  imply limited Antarctic Ice Sheet thickening and low erosion in the Shackleton Range for  $>1$  m.y, *Geology*, 32(3), 265–268, doi:10.1130/G19795.1, 2004.
- Fogwill, C. J., Turney, C. S. M., Golledge, N. R., Rood, D. H., Hippe, K., Wacker, L., Wieler, R., Rainsley, E. B. and Jones, R. S.: Drivers of abrupt Holocene shifts in West Antarctic ice stream direction determined from combined ice sheet modelling and geologic signatures, *Antarct. Sci.*, 26(6), 674–686, doi:10.1017/S0954102014000613, 2014.
- Fretwell, P., Pritchard, H. D., Vaughan, D. G., Bamber, J. L., Barrand, N. E., Bell, R., Bianchi, C., Bingham, R. G., Blankenship, D. D., Casassa, G., Catania, G., Callens, D., Conway, H., Cook, A. J., Corr, H. F. J., Damaske, D., Damm, V., Ferraccioli, F., Forsberg, R., Fujita, S., Gim, Y., Gogineni, P., Griggs, J. A., Hindmarsh, R. C. A., Holmlund, P., Holt, J. W., Jacobel, R. W., Jenkins, A., Jokat, W., Jordan, T., King, E. C., Kohler, J., Krabill, W., Riger-Kusk, M., Langley, K. A., Leitchenkov, G., Leuschen, C., Luyendyk, B. P., Matsuoka, K., Mouginot, J., Nitsche, F. O., Nogi, Y., Nost, O. A., Popov, S. V., Rignot, E., Rippon, D. M., Rivera, A., Roberts, J., Ross, N., Siegert, M. J., Smith, A. M., Steinhage, D., Studinger, M., Sun, B., Tinto, B. K., Welch, B. C., Wilson, D., Young, D. A., Xiangbin, C. and Zirizzotti, A.: Bedmap2: Improved ice bed, surface and thickness datasets for Antarctica, *Cryosphere*, 7(1), 375–393, doi:10.5194/tc-7-375-2013, 2013.
- Goehring, B. M., Balco, G., Todd, C., Moening-Swanson, I. and Nichols, K.: Late-glacial grounding line retreat in the northern Ross Sea, Antarctica, *Geology*, 47(4), 1–4, doi:10.1130/G45413.1, 2019.

- Golledge, N. R., Menviel, L., Carter, L., Fogwill, C. J., England, M. H., Cortese, G. and Levy, R. H.: Antarctic contribution to meltwater pulse 1A from reduced Southern Ocean overturning, *Nat. Commun.*, 5, 1–10, doi:10.1038/ncomms6107, 2014.
- Hein, A. S., Fogwill, C. J., Sugden, D. E. and Xu, S.: Glacial/interglacial ice-stream stability in the Weddell Sea embayment, Antarctica, *Earth Planet. Sci. Lett.*, 307(1–2), 211–221, doi:10.1016/j.epsl.2011.04.037, 2011.
- Hein, A. S., Fogwill, C. J., Sugden, D. E. and Xu, S.: Geological scatter of cosmogenic-nuclide exposure ages in the Shackleton Range, Antarctica: Implications for glacial history, *Quat. Geochronol.*, 19, 52–66, doi:10.1016/j.quageo.2013.03.008, 2014.
- Hein, A. S., Marrero, S. M., Woodward, J., Dunning, S. A., Winter, K., Westoby, M. J., Freeman, S. P. H. T., Shanks, R. P. and Sugden, D. E.: Mid-Holocene pulse of thinning in the Weddell Sea sector of the West Antarctic ice sheet, *Nat. Commun.*, 7, 1–8, doi:10.1038/ncomms12511, 2016.
- Hillenbrand, C. D., Melles, M., Kuhn, G. and Larter, R. D.: Marine geological constraints for the grounding-line position of the Antarctic Ice Sheet on the southern Weddell Sea shelf at the Last Glacial Maximum, *Quat. Sci. Rev.*, 32, 25–47, doi:10.1016/j.quascirev.2011.11.017, 2012.
- Hillenbrand, C. D., Bentley, M. J., Stollendorf, T. D., Hein, A. S., Kuhn, G., Graham, A. G. C., Fogwill, C. J., Kristoffersen, Y., Smith, J. A., Anderson, J. B., Larter, R. D., Melles, M., Hodgson, D. A., Mulvaney, R. and Sugden, D. E.: Reconstruction of changes in the Weddell Sea sector of the Antarctic Ice Sheet since the Last Glacial Maximum, *Quat. Sci. Rev.*, 100, 111–136, doi:10.1016/j.quascirev.2013.07.020, 2014.
- Howat, I. M., Porter, C., Smith, B. E., Noh, M.-J. and Morin, P.: The Reference Elevation Model of Antarctica, *Cryosph.*, 13, 655–674, doi:10.5194/tc-2018-240, 2019.
- Huybrechts, P.: A 3-D model for the Antarctic ice sheet: a sensitivity study on the glacial-interglacial contrast, *Clim. Dyn.*, 5, 79–92, 1990.
- Jeofry, H., Ross, N., Corr, H. F. J., Li, J., Morlighem, M., Gogineni, P. and Siegert, M. J.: A new bed elevation model for the Weddell Sea sector of the West Antarctic Ice Sheet, *Earth Syst. Sci. Data*, 10(2), 711–725, doi:10.5194/essd-10-711-2018, 2018.
- Johnson, J. S., Nichols, K. A., Goehring, B. M., Balco, G. and Schaefer, J. M.: Abrupt mid-Holocene



- ice loss in the western Weddell Sea Embayment of Antarctica, *Earth Planet. Sci. Lett.*, 518, 127–135, doi:10.1016/j.epsl.2019.05.002, 2019.
- Jones, R. S., Mackintosh, A. N., Norton, K. P., Golledge, N. R., Fogwill, C. J., Kubik, P. W., Christl, M. and Greenwood, S. L.: Rapid Holocene thinning of an East Antarctic outlet glacier driven by marine ice sheet instability, *Nat. Commun.*, 6, doi:10.1038/ncomms9910, 2015.
- Jull, A. J. T., Scott, E. M. and Bierman, P.: The CRONUS-Earth inter-comparison for cosmogenic isotope analysis, *Quat. Geochronol.*, 26(1), 3–10, doi:10.1016/j.quageo.2013.09.003, 2015.
- Kingslake, J., Scherer, R. P., Albrecht, T., Coenen, J., Powell, R. D., Reese, R., Stansell, N. D., Tulaczyk, S., Wearing, M. G. and Whitehouse, P. L.: Extensive retreat and re-advance of the West Antarctic Ice Sheet during the Holocene, *Nature*, 558(7710), 430–434, doi:10.1038/s41586-018-0208-x, 2018.
- Larter, R. D., Graham, A. G. C., Hillenbrand, C.-D., Smith, J. A. and Gales, J. A.: Late Quaternary grounded ice extent in the Filchner Trough, Weddell Sea, Antarctica: New marine geophysical evidence, *Quat. Sci. Rev.*, 53(C), 111–122, doi:10.1016/j.quascirev.2012.08.006, 2012.
- Levermann, A., Winkelmann, R., Albrecht, T., Goelzer, H., Golledge, N. R., Greve, R., Huybrechts, P., Jordan, J., Leguy, G., Martin, D., Morlighem, M., Pattyn, F., Pollard, D., Quiquet, A., Rodehacke, C., Seroussi, H., Sutter, J., Zhang, T., Van Breedam, J., Calov, R., Deconto, R., Dumas, C., Garbe, J., Hilmar Gudmundsson, G., Hoffman, M. J., Humbert, A., Kleiner, T., Lipscomb, W. H., Meinshausen, M., Ng, E., Nowicki, S. M. J., Perego, M., Price, S. F., Saito, F., Schlegel, N. J., Sun, S. and Van De Wal, R. S. W.: Projecting Antarctica's contribution to future sea level rise from basal ice shelf melt using linear response functions of 16 ice sheet models (LARMIP-2), *Earth Syst. Dyn.*, 11(1), 35–76, doi:10.5194/esd-11-35-2020, 2020.
- Lifton, N., Sato, T. and Dunai, T. J.: Scaling in situ cosmogenic nuclide production rates using analytical approximations to atmospheric cosmic-ray fluxes, *Earth Planet. Sci. Lett.*, 386, 149–160, doi:10.1016/j.epsl.2013.10.052, 2014.
- Lythe, M. B. and Vaughan, D. G.: BEDMAP: A new ice thickness and subglacial topographic model of Antarctica, *J. Geophys. Res. Solid Earth*, 106(B6), 11335–11351, doi:10.1029/2000jb900449, 2001.
- Morlighem, M., Rignot, E., Binder, T., Blankenship, D., Drews, R., Eagles, G., Eisen, O., Ferraccioli, F., Forsberg, R., Fretwell, P., Goel, V., Greenbaum, J. S., Gudmundsson, H., Guo, J., Helm,

- V., Hofstede, C., Howat, I., Humbert, A., Jokat, W., Karlsson, N. B., Lee, W. S., Matsuoka, K., Millan, R., Mouginot, J., Paden, J., Pattyn, F., Roberts, J., Rosier, S., Ruppel, A., Seroussi, H., Smith, E. C., Steinhage, D., Sun, B., Broeke, M. R. van den, Ommen, T. D. van, Wessem, M. van and Young, D. A.: Deep glacial troughs and stabilizing ridges unveiled beneath the margins of the Antarctic ice sheet, *Nat. Geosci.*, 13(2), 132–137, doi:10.1038/s41561-019-0510-8, 2020.
- Neumann, T. A., Conways, H., Price, S. F., Waddington, E. D., Catania, G. A. and Morse, D. L.: Holocene accumulation and ice sheet dynamics in central West Antarctica, *J. Geophys. Res. Earth Surf.*, 113(2), 1–9, doi:10.1029/2007JF000764, 2008.
- Nichols, K. A., Goehring, B. M., Balco, G., Johnson, J. S., Hein, A. S. and Todd, C.: New Last Glacial Maximum ice thickness constraints for the Weddell Sea Embayment, Antarctica, *Cryosph.*, 13, 2935–2951, 2019.
- Peltier, W. R. and Fairbanks, R. G.: Global glacial ice volume and Last Glacial Maximum duration from an extended Barbados sea level record, *Quat. Sci. Rev.*, 25(23–24), 3322–3337, doi:10.1016/j.quascirev.2006.04.010, 2006.
- Peltier, W. R., Argus, D. F. and Drummond, R.: Space geodesy constrains ice age terminal deglaciation: The global ICE-6G\_C (VM5a) model, *J. Geophys. Res. Solid Earth*, 120(1), 450–487, doi:10.1002/2014JB011176, Received, 2015.
- Pollard, D. and Deconto, R. M.: A simple inverse method for the distribution of basal sliding coefficients under ice sheets, applied to Antarctica, *Cryosph.*, 6(5), 953–971, doi:10.5194/tc-6-953-2012, 2012.
- Pollard, D., Chang, W., Haran, M., Applegate, P. and DeConto, R.: Large ensemble modeling of the last deglacial retreat of the West Antarctic Ice Sheet: Comparison of simple and advanced statistical techniques, *Geosci. Model Dev.*, 9(5), 1697–1723, doi:10.5194/gmd-9-1697-2016, 2016.
- Pollard, D., Gomez, N. and Deconto, R. M.: Variations of the Antarctic Ice Sheet in a Coupled Ice Sheet-Earth-Sea Level Model: Sensitivity to Viscoelastic Earth Properties, *J. Geophys. Res. Earth Surf.*, 122(11), 2124–2138, doi:10.1002/2017JF004371, 2017.
- Rutt, I. C., Hagdorn, M., Hulton, N. R. J. and Payne, A. J.: The glimmer community ice sheet model, *J. Geophys. Res. Earth Surf.*, 114(2), 1–22, doi:10.1029/2008JF001015, 2009.

- Sasgen, I., Mulvaney, R., Klemann, V. and Wolf, D.: Glacial-isostatic adjustment and sea-level change near Berkner Island, Antarctica. Scientific Technical Report STR 07/05., 2005.
- Spector, P., Stone, J. and Goehring, B.: Thickness of the divide and flank of the West Antarctic Ice Sheet through the last deglaciation, *Cryosph.*, 13, 3061–3075, 2019.
- Stokes, C. R., Tarasov, L., Blomdin, R., Cronin, T. M., Fisher, T. G., Gyllencreutz, R., Hättstrand, C., Heyman, J., Hindmarsh, R. C. A., Hughes, A. L. C., Jakobsson, M., Kirchner, N., Livingstone, S. J., Margold, M., Murton, J. B., Noormets, R., Peltier, W. R., Peteet, D. M., Piper, D. J. W., Preusser, F., Renssen, H., Roberts, D. H., Roche, D. M., Saint-Ange, F., Stroeven, A. P. and Teller, J. T.: On the reconstruction of palaeo-ice sheets: Recent advances and future challenges, *Quat. Sci. Rev.*, 125, 15–49, doi:10.1016/j.quascirev.2015.07.016, 2015.
- Stone, J. O., Balco, G. A., Sugden, D. E., Caffee, M. W., Sass, L. C., Cowdery, S. G. and Siddoway, C.: Holocene deglaciation of Marie Byrd Land, West Antarctica, *Science* (80-. ), 299(5603), 99–102, doi:10.1126/science.1077998, 2003.
- Tigheelaar, M., Timmermann, A., Pollard, D., Friedrich, T. and Heinemann, M.: Local insolation changes enhance Antarctic interglacials: Insights from an 800,000-year ice sheet simulation with transient climate forcing, *Earth Planet. Sci. Lett.*, 495, 69–78, doi:10.1016/j.epsl.2018.05.004, 2018.
- Whitehouse, P. L., Bentley, M. J. and Le Brocq, A. M.: A deglacial model for Antarctica: Geological constraints and glaciological modelling as a basis for a new model of Antarctic glacial isostatic adjustment, *Quat. Sci. Rev.*, 32, 1–24, doi:10.1016/j.quascirev.2011.11.016, 2012.
- Whitehouse, P. L., Bentley, M. J., Vieli, A., Jamieson, S. S. R., Hein, A. S. and Sugden, D. E.: Controls on Last Glacial Maximum ice extent in the Weddell Sea embayment, Antarctica, *J. Geophys. Res. Earth Surf.*, 122(1), 371–397, doi:10.1002/2016JF004121, 2017.
- Winkelmann, R., Martin, M. A., Haseloff, M., Albrecht, T., Bueler, E., Khroulev, C. and Levermann, A.: The Potsdam Parallel Ice Sheet Model (PISM-PIK) - Part 1: Model description, *Cryosph.*, 5(3), 715–726, doi:10.5194/tc-5-715-2011, 2011.

Study	Ice sheet model or loading history	Extent	Length of run (kyr)	Temporal resolution (kyr)	Spatial resolution (km)
Pollard et al. (2016)	PSU-3D	WAIS	30	0.2 (30 - 0.2 ka), 0.02 (0.2 ka - pres.)	20
Pollard et al. (2017)	PSU-3D	AIS	20	0.5 (20 - 17 ka), 0.2 (17 ka - pres.)	20
Tigchelaar et al. (2018)	PSU-3D	AIS	784	1	20
Golledge et al. (2014)	PISM	AIS	25	0.1	15
Kingslake et al. (2018), Albrecht et al. (2020a, b)	PISM	AIS	35	0.1	15
Whitehouse et al. (2012)	Glimmer	AIS	20	5	20
Argus et al. (2014)	ICE-6G (VM5a)	AIS	26	1 (26 - 21 ka), 0.5 (21 ka - pres.)	55 - 110

Transient or steady state	Climate forcing	Notes
Transient	Modern climatological Antarctic data set with uniform cooling perturbations proportional to a deep-sea $\delta^{18}O$ record. Sea-level variations from ICE-5G dataset.	Best scoring ensemble run with respect to modern and palaeo observations .
Transient	Same as above.	Best scoring ensemble run using a “standard” Earth viscoelastic profile.
Transient	784 kyr global climate model simulation from 3D earth system model LOVECLIM.	
Transient	Air temperature changes prescribed according to EPICA Dome C oxygen isotope record. Precipitation changes implemented according to temperature-dependent function (cooler air leads to drier atmosphere).	Best scoring ensemble run based on palaeo observations (elevation change from ice cores and marine geological evidence for lateral extent).
Transient	Surface temperatures parameterised based on a multiple regression fit (as a function of latitude and elevation). Accumulation rate history higher than reconstructed from WAIS Divide ice core.	Known as the "reference simulation", agrees reasonably well with grounding-line position reconstruction.
Semi-transient	Present-day surface temperature distribution and accumulation rates linearly shifted according to East Antarctic ice core records.	
Ice loading history		

**Table 4. 1:** Forcings, simulation duration, temporal and spatial resolution, and ancillary information for the numerical ice sheet modelling and ice loading history studies. AIS is the Antarctic Ice Sheet.

## **Chapter 5: Conclusion**

Through measuring in situ  $^{14}\text{C}$  concentrations we have shown that thick, cold-based ice covered surfaces in the Schmidt Hills, the Shackleton Range, and at the Lassiter Coast, as was hypothesised after previous studies yielded primarily, or solely, old (pre-LGM)  $^{10}\text{Be}$  and  $^{26}\text{Al}$  exposure ages. Ice was at least 300 to at least 800 m thicker than present, providing constraints for future modelling studies and demonstrating that in situ  $^{14}\text{C}$  is useful for investigating glacial histories in Antarctica where cold-based ice is pervasive.

We are confident we identified laurylamine as the primary cause of elevated in situ  $^{14}\text{C}$  concentrations described in Chapter 3. One of the advantageous systematics of in situ  $^{14}\text{C}$ , that surfaces reach a saturation concentration after ca. 30 kyr, was key in identifying the presence of in situ  $^{14}\text{C}$  contamination. We hope future studies measuring in situ  $^{14}\text{C}$  from quartz either follow the procedure described in Chapter 3, or avoid the use of froth flotation entirely, to remove or avoid contamination of their results.

Finally, we showed how numerical ice sheet models in the WSE systematically predict ice thinning earlier than indicated by cosmogenic nuclide constraints. Thinning of ice is often predicted by models at a rate that exceeds that allowed by exposure ages. It is difficult to evaluate ice sheet model results that prescribe relatively thick LGM ice in the WSE using only cosmogenic nuclide constraints, as the majority of constraints provide a lower limit of LGM ice. It is also difficult or impossible to evaluate ice sheet model outputs using individual measurements of in situ  $^{14}\text{C}$  because most model simulation results are reported from the LGM to the present, thus we do not have a predicted timing for the covering of study sites by a thickening ice sheet.

Future work in the WSE, as well as the wider Antarctic continent, aiming to constrain past ice thicknesses will likely involve further use of in situ  $^{14}\text{C}$  measurements. As well as studies employing traditional elevation transects of measurements of in situ  $^{14}\text{C}$  from the surfaces of nunataks to fill spatial gaps in our knowledge, targeted high-elevation measurements of in situ  $^{14}\text{C}$  may provide an upper limit on LGM thicknesses in areas that are already considered well-studied using long-lived nuclides. Furthermore, future studies could target bedrock beneath ice to study both short and long term ice sheet behaviour. Measurements from samples collected from beneath the ice sheet may reveal if ice in the WSE and wider West Antarctic Ice Sheet (WAIS) has been thinner than present (e.g. Schaefer et al.,

2016). It is hypothesised that the grounding line of the WAIS retreated further inland of the modern grounding line and subsequently readvanced in the Holocene (Kingslake et al., 2018; Siegert et al., 2019). Measurements of in situ  $^{14}\text{C}$  from subglacial bedrock will reveal if a retreat and readvance took place, with implications for the sensitivity of the WAIS to future climate change. Measurements of long-lived nuclides will also provide insight into the longer term history of the WAIS and may shed light on hypothesised WAIS collapse (e.g. Scherer et al., 1998).

## **References**

- Kingslake, J., Scherer, R. P., Albrecht, T., Coenen, J., Powell, R. D., Reese, R., Stansell, N. D., Tulaczyk, S., Wearing, M. G. and Whitehouse, P. L.: Extensive retreat and re-advance of the West Antarctic Ice Sheet during the Holocene, *Nature*, 558(7710), 430–434, doi:10.1038/s41586-018-0208-x, 2018.
- Schaefer, J. M., Finkel, R. C., Balco, G., Alley, R. B., Caffee, M. W., Briner, J. P., Young, N. E., Gow, A. J. and Schwartz, R.: Greenland was nearly ice-free for extended periods during the Pleistocene, *Nature*, 540(7632), 252–255, doi:10.1038/nature20146, 2016.
- Scherer, R. P., Aldahan, A., Tulaczyk, S., Possnert, G., Engelhardt, H. and Kamb, B.: Pleistocene Collapse of the West Antarctic Ice Sheet, *Science*, 281(5373), 82–85, 1998.
- Siegert, M. J., Kingslake, J., Ross, N., Whitehouse, P. L., Woodward, J., Jamieson, S. S. R., Bentley, M. J., Winter, K., Wearing, M., Hein, A. S., Jeofry, H. and Sugden, D. E.: Major ice-sheet change in the Weddell Sector of West Antarctica over the last 5000 years, *Rev. Geophys.*, 0–2, doi:10.1029/2019RG000651, 2019

## **Biography**

Keir is from Staffordshire, in the northwest of England. He received a BSc from Aberystwyth University in 2012, and a MSc from Keele University in 2014. He cannot leave out the fact that, whilst studying in Wales, Keir spent a semester studying at the University Centre in Svalbard, Norway, a time he looks back on fondly and which still inspires him to study the cryosphere to this day, nine years later. From 2015 to the present, Keir has been working toward attaining a PhD in Earth and Environmental Science at Tulane University, spending much of his time in the Cosmogenic Nuclide laboratory, pretending to know what he is doing.